Study of Deformation Behaviour, Processing Maps and Springback Behaviour in Ti-6Al-4V Alloy at High Temperatures

THESIS

Submitted in partial fulfillment
of the requirements for the degree of
DOCTOR OF PHILOSOPHY

by

MOHD ABDUL WAHED
ID NO. 2015PHXF0411H

Under the Supervision of

Dr. AMIT KUMAR GUPTA

&

Under the Co-supervision of

Dr. NITIN KOTKUNDE

BITS Pilani
Pilani | Dubai | Goa | Hyderabad

BIRLA INSTITUTE OF TECHNOLOGY AND SCIENCE, PILANI

2021

BIRLA INSTITUTE OF TECHNOLOGY AND SCIENCE – PILANI

CERTIFICATE

This is to certify that the thesis entitled, "**Study of Deformation Behaviour, Processing Maps and Springback Behaviour in Ti-6Al-4V Alloy at High Temperatures**" submitted by **Mohd Abdul Wahed** ID No. **2015PHXF0411H** for award of Ph.D. of the Institute, embodies original work done by him under our supervision.

_____	_____
Supervisor	*Co-Supervisor*
Prof. Amit Kumar Gupta,	Dr. Nitin Kotkunde,
Mechanical Engineering Department	Mechanical Engineering Department
BITS Pilani, Hyderabad Campus	BITS Pilani, Hyderabad Campus
Date:	Date:

ACKNOWLEDGEMENT

I am extremely thankful to **Almighty God** for giving me this opportunity to pursue my interest in research work.

I would like to express my sincere gratitude to my supervisors **Prof. Amit Kumar Gupta** and **Dr. Nitin Kotkunde** for their robust support, guidance and constant availability for the technical discussions. I feel motivated and exhilarated after technical discussions with them. I would like to thank them for being my inspiration and well-wisher. This thesis is the outcome of the kind cooperation, technical and moral support extended by **Prof. Swadesh Kumar Singh**, Professor in the Mechanical Engineering Department, GRIET Hyderabad and for providing the opportunity to use the laboratory facilities available at GRIET.

I am grateful to my doctoral advisory committee (DAC) members, **Dr. Sujith R** and **Dr. Kurra Suresh** for their valuable suggestions during the semester reviews. I also take this opportunity to thank **Prof**. **Souvik Bhattacharya**, Vice - Chancellor, BITS-Pilani, **Prof. G. Sundar**, Director, BITS-Pilani, Hyderabad Campus, **Prof. Vamshi Krishna Venuganti**, Associate Dean, AGSRD and **Prof. Vidya Rajesh**, former Associate Dean, ARD for their constant support and for providing a good research atmosphere.

Co-authors in my published papers deserve a special thanks. The valuable inputs and discussion with them helped in publishing the papers in the reputed international journals and conferences.

I would like to express thanks to the former Head of Department (HOD) **Prof. YVD Rao** and present HOD **Prof. NSK Reddy** for being kind and cooperative and

the doctoral research committee (DRC) convener **Dr. Sabaresh G R** and **Dr. Satish Dubey** and other DRC members for organizing timely semester reviews.

I would like to express thanks to my friends **Akhil Bhardwaj** and **C. Kiran Sagar** for their helpful discussions during this research work. Also, I would like to thank **Naishadh Gohil** and **Abdul Wahab** for helping in proof reading the thesis.

I am extremely obliged to all the **faculty members** and staff of the **Mechanical Engineering Department**. I owe my thanks to the **technical staff** of **Workshop** for providing me the generous cooperation and help each and every time required.

Most of all, I would like to sincerely express my gratitude to **my parents, my brother and sister** for their relentless support, encouragement and for their trust in me and letting me pursue my desire. My special appreciation goes to **my wife and daughter** for their love, support, patience and encouragement. Also, I would like to thank my relatives, close friends and other faculties beyond BITS for their encouragement.

Finally, I would like to recognize and record grateful thanks to all the individuals who have assisted me in this research work directly or indirectly.

Mohd Abdul Wahed

ABSTRACT

Ti-6Al-4V alloy, having high strength-to-weight ratio, plays a vital role in aerospace and defense applications, however due to its poor formability at room temperature it needs to be deformed at high temperatures for producing light weight complex shaped components. Particularly, it finds applications in a wide range of components such as fan blades, engine nacelle component, tank half shell, access ducting, heat exchangers, etc. This thesis work focusses on the study of deformation behaviour, processing maps and springback behaviour in V-bending process for Ti-6Al-4V alloy at high temperatures.

Accurate determination of material properties and flow stress behaviour is an essential prerequisite for understanding the forming behaviour of a material. To this effect, tensile tests have been carried out at high temperatures from 700℃ to 900℃ and at various strain rates 10^{-1} s^{-1} to 10^{-4} s^{-1}. The obtained results indicate greater than 30% ductility in common and greater than 200% ductility in the range of 750℃ to 900℃ and at 10^{-4} s^{-1} strain rate, demonstrating the superplasticity of Ti-6Al-4V alloy. Microstructure examination of broken specimens shows coarsening of grain size and difference in the volume fraction of beta phase with the increase of temperature and Scanning Electron Microscopy reveals dominating ductile fracture failure at high temperatures.

To predict the high temperature flow stress behaviour of Ti-6Al-4V alloy, modified Arrhenius model has been developed and the correlation constant (R) has been obtained as 0.993 in comparison with the experimental flow stress. Further, processing maps have been developed for confirming the safe region of superplasticity depending on the efficiency and instability maps at various strain rates

and high temperatures. Processing maps distinctly illustrates excellent power dissipation efficiency lacking instability in the superplasticity range, viz. 770°C - 900°C and 10^{-2} s^{-1} - 10^{-4} s^{-1}, whereas instable regions have been correlated with fractography and optical microscopy. In addition, a comparative study has been carried out for different instability criteria and processing maps.

Considering the safe region for hot deformation of Ti-6Al-4V alloy, there is a need to design and optimize the process parameters for V-bending process at high temperatures for obtaining zero springback effect. Hence, experimental and finite element (FE) studies have been conducted for V-bending of Ti-6Al-4V alloy at high temperatures using Taguchi L_9 experimental design involving three process parameters - high temperature, punch speed and holding time. From the obtained experimental results, percentage contribution of individual process parameters have been determined and ANOVA revealed temperature as a dominant parameter for reducing springback behaviour considerably. FE results have been found analogous to the experimental results with percentage of error having a mean of 7.35% and standard deviation of 1.24%.

Furthermore, using the developed FE model for a full factorial design of L_{27} orthogonal array, the springback behaviour has been optimized using response surface method and genetic algorithm and thus achieved optimium process parameters setting for a minimum spring back value of 0.067º. This has also been experimentally validated achieving almost zero springback value

Keywords: Ti-6Al-4V alloy; Superplasticity; Material characterization; Constitutive modelling; Processing maps; Springback; FEA; RSM; GA

TABLE OF CONTENTS

CERTIFICATE ..... **i**
ACKNOWLEDGEMENT ..... **ii**
ABSTRACT ..... **iv**
TABLE OF CONTENTS ..... **vi**
LIST OF FIGURES ..... **viii**
LIST OF TABLES ..... **xii**
LIST OF ACRONYMS ..... **xiii**
LIST OF SYMBOLS ..... **xiv**
CHAPTER 1 : INTRODUCTION **1**
1.1. Introduction to Ti-6Al-4V Alloy 2
1.2. Forming Behaviour of Ti-6Al-4V Alloy at High Temperatures 4
1.2.1 Constitutive Modelling 5
1.2.2 Processing Maps 6
1.3. Sheet Metal Bending 8
1.4. Spring back Behaviour 11
1.5. FE Analysis of Bending Process 13
1.6. Need of the Study 14
CHAPTER 2 : LITERATURE REVIEW **15**
2.1. Deformation Behaviour and Material Characterization 15
2.2. Constitutive Modelling 18
2.3. Processing Maps 21
2.4. Spring back Studies 27
2.5. Optimization Techniques for Spring back Behaviour 31
2.6. Research Gaps 33
2.7. Objectives of the Study 34
2.8. Methodology 34
2.9. Thesis Organization 36
CHAPTER 3 : DEFORMATION BEHAVIOUR AND CHARACTERIZATION OF Ti-6Al-4V ALLOY **38**
3.1. Experimental Details 38
3.2. Mechanical Behaviour of Ti-6Al-4V Alloy at High Temperatures 42
3.2.1 Stress vs. Strain Curves in Different Orientations 46
3.2.2 Anisotropy Properties 48
3.3. Metallography Characterization of Ti-6Al-4V Alloy 52
3.3.1 Flow Softening Characterization 52
3.3.2 Superplasticity Characterization 56
3.3.3 X-ray Diffraction 62
3.4. Summary 63

CHAPTER 4 : CONSTITUTIVE MODEL AND PROCESSING MAPS FOR Ti-6Al-4V ALLOY 64
4.1. Development of Constitutive Model 65
4.2. Development of Processing Maps 72
4.2.1 Determination of Strain Rate Sensitivity 72
4.2.2 Efficiency Maps 75
4.2.3 Instability Maps 77
4.2.4 Processing Maps 79
4.3. Correlation of Instability Region with Fractography and Microstructure 82
4.4. Comparison of Instability Criteria 85
4.5. Comparison of Processing Maps 86
4.6. Summary 88
CHAPTER 5 : EXPERIMENTAL INVESTIGATION OF SPRING BACK IN V-BENDING PROCESS FOR Ti-6Al-4V ALLOY 89
5.1. Experimental Set Up 89
5.2. Design of Experiments – Taguchi L_9 Orthogonal Array 93
5.3. Experimental Results of Spring back in V-Bending Process 96
5.4. Analysis of Variance and Percentage Contribution 101
5.5. Comparison of Spring back between Room and High Temperatures 103
5.6. Spring back Factors 104
5.7. Summary 105
CHAPTER 6 : FINITE ELEMENT ANALYSIS AND OPTIMIZATION OF SPRING BACK BEHAVIOUR IN V-BENDING OF Ti-6Al-4V ALLOY 106
6.1. FE Modelling of Spring back Behaviour in V-Bending Process 106
6.2. FE Analysis of Spring back Behaviour in V-Bending Process 110
6.3. Comparison of Experimental and Simulation Results 112
6.4. Full Factorial Simulation Results 112
6.5. Optimization Methods Applied for Full Factorial Design 114
6.5.1 Response Surface Method 114
6.5.2 Genetic Algorithm 116
6.6. Confirmation Test 120
6.1. Summary 121
CHAPTER 7 : CONCLUSIONS 122
7.1. Salient Conclusions 122
7.2. Limitations of the Study 125
7.3. Specific Contribution to the Research 126
7.4. Future Scope 126
REFERENCES 127
PUBLICATIONS 143
BIOGRAPHIES 144

LIST OF FIGURES

Figure 1.1 Sheet metal applications in airframe of an aeroplane (Inagaki, et al. 2014) 1
Figure 1.2 Titanium applications in aero-engine (Inagaki, et al. 2014)..... 2
Figure 1.3 Sheet metal applications of Ti-6Al-4V alloy..... 3
Figure 1.4 Ti-6Al-4V alloy engine nacelle part (a) conventionally formed and (b) superplastically formed (S. Semiatin 2006) 4
Figure 1.5 Classification of constitutive models..... 6
Figure 1.6 (a) Processing map generated using ELI Ti-6Al-4V alloy and (b) its interpretation (Prasad, Rao and Sasidhara 2015) 7
Figure 1.7 Demonstration of a bending process 8
Figure 1.8 Bending processes (a) air bending, (b) U-bending and (c) V-bending... 9
Figure 1.9 Four stages of V-bending (a) Three point contact, (b) Partial contact, (c) Full contact and (d) Punch unloading (Zong, et al. 2015)..... 9
Figure 1.10 Stress state in V-bending (Ao, et al. 2018)..... 10
Figure 1.11. Stress – strain distribution in the bending portion (Zong, et al. 2015). 10
Figure 1.12 Illustration of spring back in V-bending 11
Figure 1.13 Parameters influencing spring back behaviour..... 12
Figure 1.14 Hysteresis loop due to Bauschinger effect (S. Semiatin 2006) 13
Figure 2.1 Phase diagram of titanium alloys (Porntadawit, Uthaisangsuk and Choungthong 2014)..... 20
Figure 2.2 Constitutive relationship for (a) non-linear and (b) linear power dissipation (Liu, Hui, et al. 2019)..... 22
Figure 2.3 Corroboration of physical models with processing maps (Prasad, Rao and Sasidhara 2015) 22
Figure 2.4 Instability maps established by different criteria at 0.5 strain (Cai, et al. 2016)..... 25
Figure 2.5 Three dimensional deformation map of Ti-6Al-4V (Quan, et al. 2020) 26
Figure 2.6 A three dimensional instability map of Ti-2.7Cu alloy (Zhou, et al. 2020) 27

Figure 2.7 V-bending in (a) loading of punch, (b) spring back and (c) negative spring back (Teimouri, et al. 2012) 29
Figure 2.8 Methodology adopted in this study 35
Figure 2.9 Thesis organisation 37
Figure 3.1 An overview of the chapter 38
Figure 3.2 (a) Optical image and (b) SEM image of initial Ti-6Al-4V alloy 39
Figure 3.3 Tensile test specimen (all dimensions are in millimetre) 40
Figure 3.4 (a) Computer control UTM of 50 KN capacity and (b) diverse temperature split furnace 41
Figure 3.5 Heating and cooling of Ti-6Al-4V alloy tensile specimens 41
Figure 3.6 Tensile tested specimens exhibiting overall elongation till fracture 43
Figure 3.7 Stress vs. strain curves in Ti-6Al-4V alloy along 0° orientation conducted at high temperatures and various strain rates (a) 10^{-1} s^{-1}, (b) 10^{-2} s^{-1}, (c) 10^{-3} s^{-1} and (d) 10^{-4} s^{-1} 44
Figure 3.8 Strain rate sensitivity of Ti-6Al-4V alloy at (a) 700℃ & (b) 900℃ 45
Figure 3.9 Graphs representing difference of (a) YS, (b) UTS and (c) El % pertaining to high temperatures at various strain rates 46
Figure 3.10 Stress vs. strain curves at (a) 10^{-2} s^{-1}, (b) 10^{-3} s^{-1} & (d) 10^{-4} s^{-1} 47
Figure 3.11 Stress vs. strain plots at (a) 10^{-2} s^{-1}, (b) 10^{-3} s^{-1} & (d) 10^{-4} s^{-1} 48
Figure 3.12 Tensile specimen for anisotropy study 48
Figure 3.13 Difference of mechanical properties (a) YS & (b) UTS at 10^{-4} s^{-1} and high temperatures in different orientations 52
Figure 3.14 (a) Scanning Electron micrographs of ruptured specimens at 800℃ (a) 10^{-3} & (b) 10^{-4} s^{-1} and at 750℃ (c) 10^{-2}, (d) 10^{-3} & (e) 10^{-4} s^{-1} respectively 53
Figure 3.15 Optical micrographs of ruptured specimens at 800℃ (a) 10^{-3} s^{-1} & (b) 10^{-4} s^{-1} and at 750℃ (b) 10^{-2} s^{-1}, (c) 10^{-3} s^{-1} & (d) 10^{-4} s^{-1} respectively 55
Figure 3.16 Optical images of ruptured specimens at 10^{-4} s^{-1} and different temperatures (a) RT, (b) 750℃ and (c) 800℃ 57
Figure 3.17 Volume fractions and Avg. grain size of beta phase for ruptured specimens at 10^{-4} s^{-1} and different temperatures at (a) RT, (b) 750℃ & (c) 800℃ 58

Figure 3.18 Quantitative study of beta phase for ruptured specimens (a) percentage area fraction & (b) Average size (μm) pertaining RT, 750℃ & 800℃ at 10^{-4} s^{-1} 59
Figure 3.19 Quantitative study of alpha phase for ruptured specimens - Average size (μm) pertaining to RT, 750℃ & 800℃ at 10^{-4} s^{-1} 59
Figure 3.20 SEM images of ruptured specimens at 10^{-4} s^{-1} and different temperatures (a) RT, (b and c) 750℃ & (d and e) 800℃..... 61
Figure 3.21 XRD of Ti-6Al-4V alloy deformed at 10^{-4} s^{-1} and different temperatures 62
Figure 4.1 True stress - true strain curves along 0º orientation at high temperatures & various strain rates (a) 10^{-2} s^{-1}, (b) 10^{-3} s^{-1} & (c) 10^{-4} s^{-1} 64
Figure 4.2 Comparison between experimental and predicted flow stress at high temperatures and various strain rates (a) 10^{-2} s^{-1}, (b) 10^{-3} s^{-1} & (c) 10^{-4} s^{-1} 71
Figure 4.3 Comparison between experimental and predicted stress behaviour..... 71
Figure 4.4 Log - log curves of true stress - strain rate at various strains (a) 0.1, (b) 0.2, (c) 0.3 & (d) 0.4..... 73
Figure 4.5 Contour maps representing m at various values of strains (a) 0.1, (b) 0.2, (c) 0.3 & (d) 0.4..... 75
Figure 4.6 Efficiency maps generated at various strain values (a) 0.1, (b) 0.2, (c) 0.3 & (d) 0.4 respectively (Contour numbers in maps denote the efficiency.) 77
Figure 4.7 Instability maps generated at various strain values (a) 0.1, (b) 0.2, (c) 0.3 & (d) 0.4 (shaded region in maps denote the instability.) 79
Figure 4.8 Processing maps generated at various strain values (a) 0.1, (b) 0.2, (c) 0.3 & (d) 0.4 (The contour numbers in maps signify the efficiency and shaded area in maps signify the instability) 81
Figure 4.9 SEM images of ruptured specimens at 700℃ and 10^{-2} s^{-1} strain rate at (a) 46X, (b) 300X, (c) 800X & (d) 1.5kX magnifications respectively 82
Figure 4.10 SEM images of ruptured specimens at 750℃ and 10^{-2} s^{-1} at (a) 61X and (b) 1.5kX magnifications..... 83

Figure 4.11 SEM images of ruptured specimens at 700℃ and 10^{-3} s^{-1} at (a) 70X and (b) 1.5kX magnifications 83
Figure 4.12 Optical micrographs of ruptured specimens at (a) 700℃_10^{-2} s^{-1}, (b) 700℃_10^{-3} s^{-1} & (c) 750℃_10^{-2} s^{-1} at 100X magnification 84
Figure 4.13 Instability criteria (a & b) Prasad's and (c & d) Murthy's at 0.1 and 0.4 strains respectively 86
Figure 4.14 Processing map of Ti-6Al-4V alloy developed at 0.5 strain (Numbers denote efficiency & instability as shaded region) (Prasad, Rao and Sasidhara 2015) 87
Figure 5.1 (a) Compression testing machine and (b) Heating split furnace 90
Figure 5.2 Schematic view of (a) 2D punch dimensions, (b) 2D die dimensions and (c) combined punch and die in a 3D CAD model 90
Figure 5.3 Loading of punch and die on CTM 91
Figure 5.4 V-bending of Ti-6Al-4V alloy (a) process and (b) geometry..... 92
Figure 5.5 (a) Coordinate measuring machine with V-bend specimen and (b) schematic of V-bend specimen showing measured points 93
Figure 5.6 A flow chart of Taguchi method 94
Figure 5.7 V bent samples as per Taguchi L_9 orthogonal array..... 97
Figure 5.8 Box plot displaying spring back values (SB_1, SB_2 & SB_3) 99
Figure 5.9 Main effect plots of process parameters for smaller is better SN ratios100
Figure 5.10 Interaction plots for spring back in (a) temp vs. punch speed, (b) temp vs. holding time, (c) punch speed vs. temp and (d) holding time vs. temp 102
Figure 5.11 Experiementally measured spring back values at (a) RT, (b) 700℃ and (c) 900℃ 103
Figure 6.1 Steps implemented in FEA 106
Figure 6.2 2D FE model of V-bending process 107
Figure 6.3 FE modelling of V-bending process (a) initial step, (b) loading step, (c) holding step and (d) unloading step 108
Figure 6.4 Boundary conditions and blank meshing 110
Figure 6.5 FE simulation outcome of unloading step (a) 700-0.05-1, (b) 800-0.1-0 & (c) 900-0.01-10 111
Figure 6.6 Contour plots at different settings (a) 700_0.1_0, (b) 800_0.05_0, (c) 900_0.05_0 and (d) 900_0.1_10..... 116

LIST OF TABLES

Table 3.1 Chemical composition of as-received Ti-6Al-4V alloy sheet (% wt.) ... 38
Table 3.2 Anisotropic parameters ... 49
Table 3.3 Material properties at high temperatures and different strain rates in different orientations ... 50
Table 3.4 Flow softening index at 10^{-4} s^{-1} and high temperatures in different orientations ... 51
Table 3.5 Grain size at 750℃ and different strain rates ... 54
Table 4.1 Material coefficients obtained for m-Arr model ... 69
Table 5.1 Three level design of process parameters ... 95
Table 5.2 Design of parameters according to Taguchi L_9 orthogonal array ... 95
Table 5.3 Experimental spring back values for Taguchi L_9 orthogonal array ... 98
Table 5.4 ANOVA outcome for experimentation spring back ... 101
Table 6.1 Mesh sensitivity analysis ... 109
Table 6.2 Comparison between simulation & experimentation outcomes ... 112
Table 6.3 Full factorial FE simulation outcome of spring back ... 113
Table 6.4 Calculated regression constants for FE simulated spring back based on the coded units ... 118
Table 6.5 ANOVA for FE simulated spring back ... 119
Table 6.6 Calculated regression constants for spring back using uncoded units ... 119
Table 6.7 Simulation and experimental spring back value for the optimum process parameters ... 120

LIST OF ACRONYMS

ANOVA	Analysis of Variance
ASTM	American Society for Testing of Materials
CMM	Coordinate Measuring Machine
CPE4R	Four-Node Bilinear Plane Strain Quadrilateral Reduced Integration, Hourglass Control Shell Element
CTM	Compression Testing Machine
DMM	Dynamic Material Model
DRV	Dynamic Recovery
DRX	Dynamic Recrystallization
EBSD	Electron Backscatter Diffraction
EDM	Electrical Discharge Machining
EDS	Energy Dispersive Spectroscopy
FEA	Finite Element Analysis
GA	Genetic Algorithm
GBS	Grain Boundary Sliding
HSS	High Speed Steel
m-Arr	Modified Arrhenius
OM	Optical Microscope
RSM	Response Surface Method
RT	Room Temperature
SB	Spring back
SEM	Scanning Electron Microscope
S/N	Signal to Noise ratio
UTM	Universal Testing Machine
UTS	Ultimate Tensile Strength
XRD	X-Ray Diffraction
YS	Yield Strength

LIST OF SYMBOLS

$El\ \%$	Percentage Elongation
$\%\ wt.$	Percentage Weight
R	Lankford Parameter
R_N	Normal Anisotropy
ΔR	Planar Anisotropy
γ	Flow Softening Index
m	Strain Rate Sensitivity
T_β	Beta Transus Temperature
T_m	Melting Temeperature
Z	Hollomon Parameter
Q	Activation Energy
R	Universal Gas Constant
T	Temperature
$\dot{\varepsilon}$	Strain Rate
R	Correlation Constant in m-ARR Model
$A, \alpha, n, \beta_0, \beta_1, \beta_2$	Material Coefficients for m-ARR Model
σ	Stress
ε	Strain
η	Efficiency of Power Dissipation
$\xi\ (\dot{\varepsilon})$	Dimensionless Process Parameter in Instability Map
σ_r	Radial Stress
ε_r	Radial Strain
σ_θ	Tangential Stress
ε_θ	Tangential Strain
σ_z	Transverse Stress
$\overline{S/N}$	Mean for Overall Signal-to-Noise Ratio
SS_i	Mean of Parameters belongs to Variations of Overall mean
SS	Sum of Squares belong to Variations of Overall Mean

CHAPTER 1 : INTRODUCTION

Among all the manufacturing processes, sheet metal forming is a prominent manufacturing process to produce various parts and components required especially in the aerospace and automobile industry, as it reduces the component's cost and simultaneously enhances the performance (Banabic 2010). It involves a metal blank to be plastically deformed for getting a desired shape. As a result, it eliminates the use of other conventional processes that gives an edge for its use in industries with mass production. Some of the sheet metal applications in an aeroplane with respect to the airframe are shown in Figure 1.1 (Inagaki, et al. 2014). Apart from this, titanium alloys also find their application in an aero-engine as presented in Figure 1.2. In the aerospace applications about 70% of titanium shipments as well as jet engines use more than half of the overall aerospace consumptions (Froes 2015).

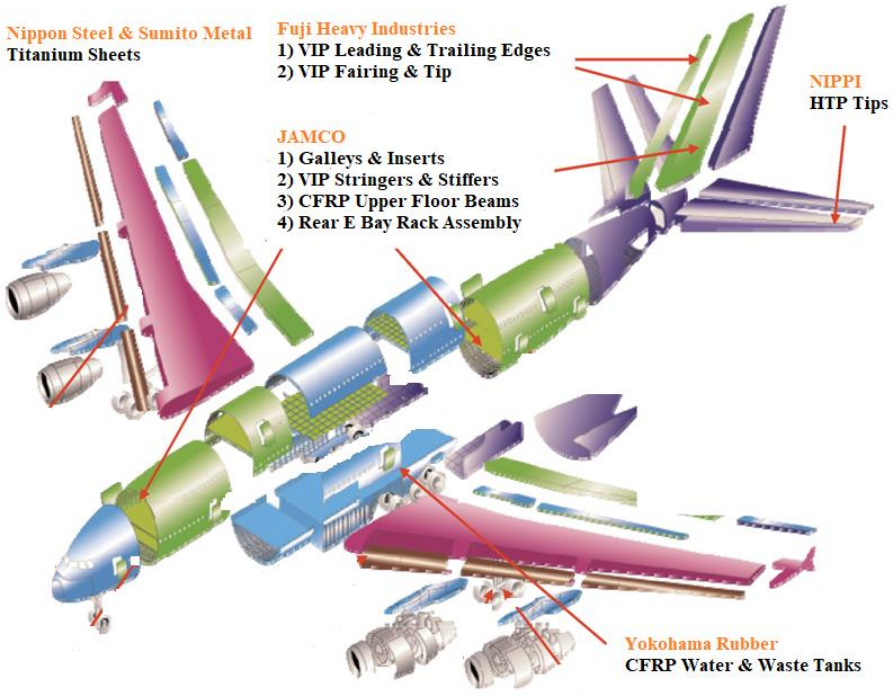

Figure 1.1 Sheet metal applications in airframe of an aeroplane (Inagaki, et al. 2014)

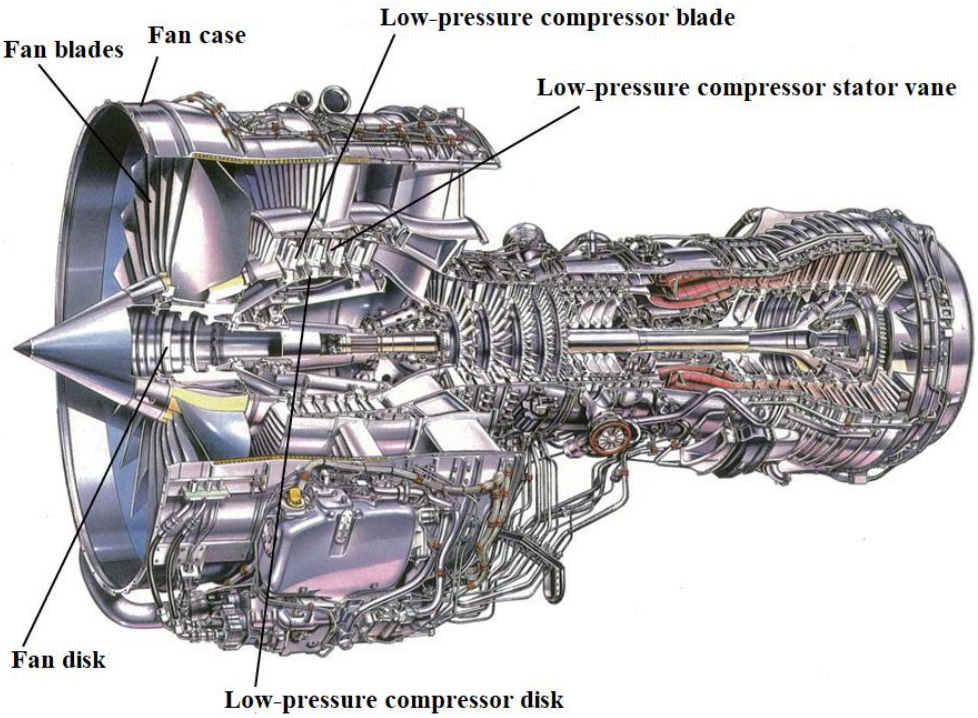

Figure 1.2 Titanium applications in aero-engine (Inagaki, et al. 2014)

1.1. Introduction to Ti-6Al-4V Alloy

Among all the titanium alloys, Ti-6Al-4V is one of the prominent alloys, as it contributes 50% of total fabrication and it is treated as the driving force in manufacturing of titanium products (Leyens and Peters 2003). Ti-6Al-4V alloy has different aerospace applications like cockpit window frame, wing box etc., in the airframe and like fan blade etc., in the aero-engine. Ti-6Al-4V alloy shows remarkable properties namely, high melting point ($T_m \approx 1600$ °C), high strength (≈ 1050 MPa), low density (≈ 4.5 gm/cc), low thermal conductivity, high corrosion resistance and high ductility (Froes 2015).

The scope of sheet metal applications of Ti-6Al-4V alloy for some diverse industries has been presented in Figure 1.3 (Leyens and Peters 2003). However, low formability and high spring back behavior in Ti-6Al-4V alloy, especially at ambient temperature, confines its application (Badr, et al. 2015). One of the solutions to avoid

this behavior is by working at high temperatures, i.e., by using warm forming or hot forming or superplastic forming (Li, et al. 2014).

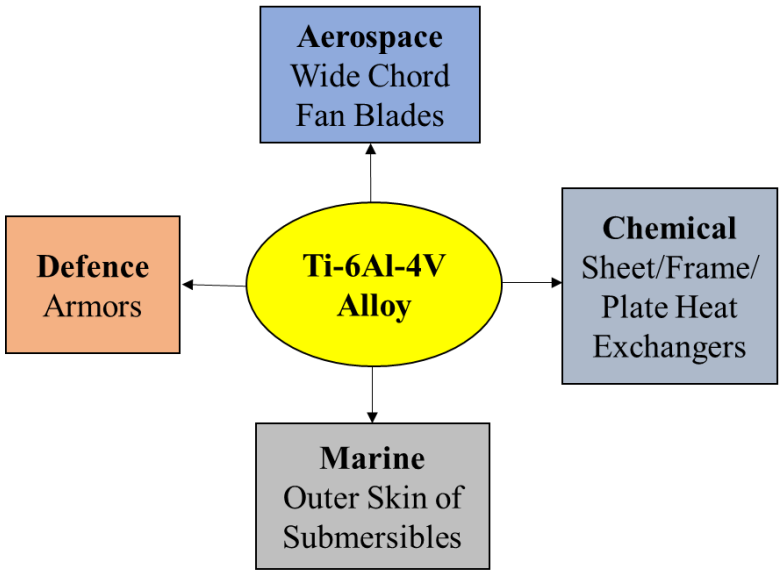

Figure 1.3 Sheet metal applications of Ti-6Al-4V alloy

Warm forming is defined when the working temperatures are within 0.3 T_m to 0.5 T_m (≈ 480 °C – 800 °C) and hot forming is defined when the working temperatures are within 0.44 T_m to 0.55 T_m (≈ 704 °C – 880 °C). Whereas, superplastic forming is defined above 0.55 T_m (≈ 880 °C) with a stable fine grained microstructure having grain size between 5 – 15 µm and at low strain rates from 10^{-4} s^{-1} – 10^{-2} s^{-1} (Giuliano 2011). In superplasticity, the material experiences large tensile elongations (≥ 200%) with low flow stresses before rupture. In addition, here an important parameter is strain rate sensitivity (m) which varies between 0.3 – 0.8 (Tuoyang, et al. 2014).

Ti-6Al-4V alloy is a multicrystalline metal viz., it endures high ductility with more than 200% elongation before rupture indicating superplasticity. Figure 1.4 presents an example of an aero-engine nacelle component (S. Semiatin 2006), where its fabrication in a conventional way required 41 detailed parts and more than 200

fasteners as shown in Figure 1.4 (a), whereas when manufactured using superplastic forming, the same component has been manufactured using a single sheet as shown in Figure 1.4 (b). Superplasticity condition (especially high temperature range) is most preferable for bending, i.e., with increase in temperature, strength decreases which reduces spring back effect considerably (Boyer, Welsch and Collings 1994).

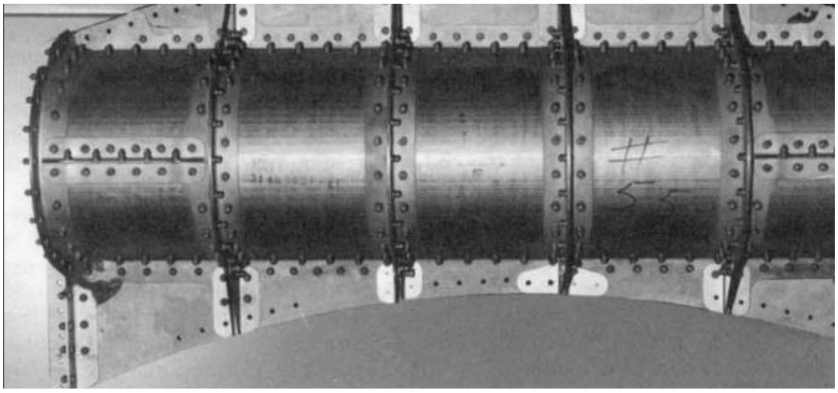

(a)

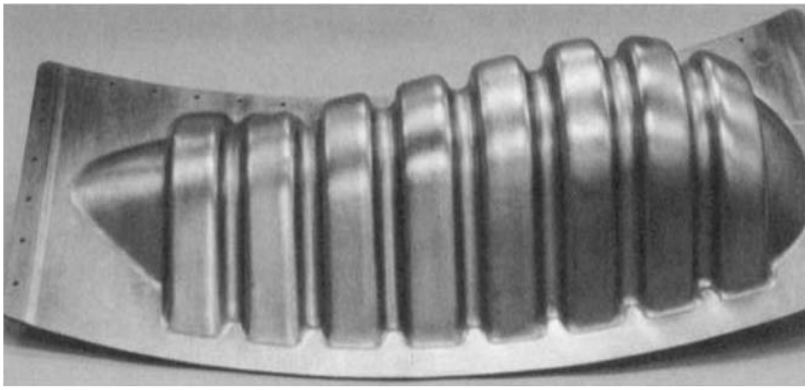

(b)

Figure 1.4 Ti-6Al-4V alloy engine nacelle part (a) conventionally formed and (b) superplastically formed (S. Semiatin 2006)

1.2. Forming Behaviour of Ti-6Al-4V Alloy at High Temperatures

Studying the forming behaviour of Ti-6Al-4V alloy at elevated/high temperatures involves the following considerations:

- A sophisticated set up to perform necessary experiments, having a high temperature capacity furnace
- Proper selection of die material, to resist high temperatures and dimensional stability
- High temperature lubrication to prevent oxidation effect on the dies and the working material
- Appropriate heating time and use of thermocouples to indicate temperature
- Suitable holding time after heating, to achieve thermal equilibrium then conducting experiments

For better understanding of the forming behaviour of any material, it is necessary to first study the mechanical properties, the flow stress behaviour and deformation regimes. In this view, the researchers have developed modelling techniques, such as constitutive modelling, processing maps, etc., which are discussed in the next section.

1.2.1 Constitutive Modelling

In the earlier days, trial and error methods were performed to understand the hot deformation process, which is a non-economical and time consuming process. Therefore, researchers use the finite element (FE) methods for such studies which utilize constitutive/mechanical models and thus, optimize the hot deformation processes (Bodunrin 2020). An understanding of hot tensile behavior at diverse temperatures as well as strain rates is important for effective process design in any metal forming process (Chandra 2002). A constitutive model/equation defines flow stress in terms of varying strain, strain rate and range of working temperature (Khan

and Yu 2012). The flow stress in materials during hot deformation is greatly affected by strain hardening and strain softening mechanisms (Lin and Chen 2011).

A constitutive model must consist of a reasonable amount of numerical constants that can be obtained by conducting a limited amount of experiments (Gupta, Krishnan and Singh 2013). Therefore, different constitutive models/equations have been developed for predicting flow stress, depending on the obtained experimental data (Liang and Khan 1999). These are divided as phenomenological based model, physical based model as well as (ANN) artificial neural network (Lin and Chen 2011). Some of them are presented in Figure 1.5.

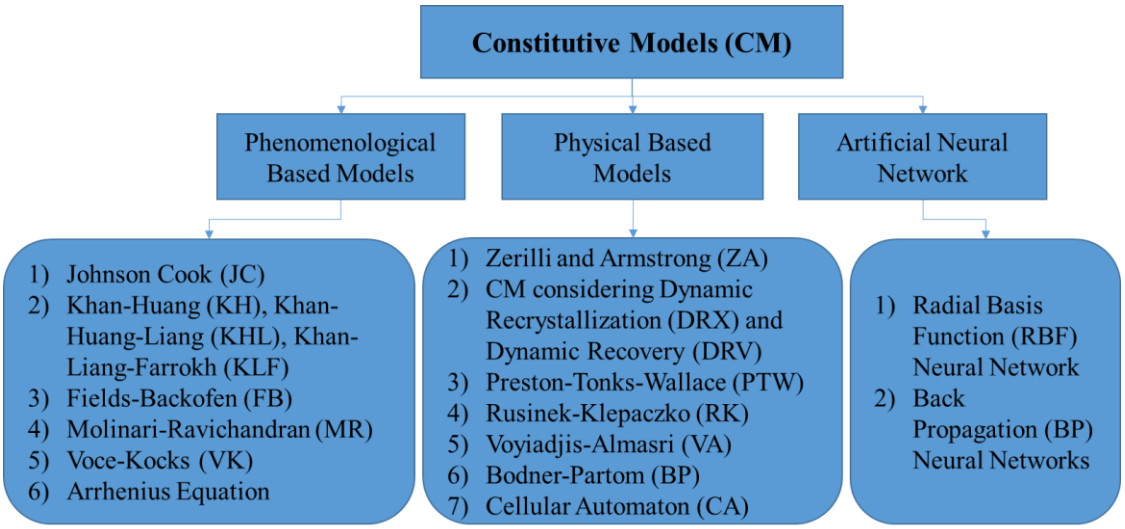

Figure 1.5 Classification of constitutive models

1.2.2 Processing Maps

Processing maps play an essential role in obtaining the optimal process parameters during the event of hot deformation conditions. It is described as a relationship between working temperature range as well as strain rate obtained at a particular strain (Prasad and Seshacharyulu 1998). Processing maps are helpful in identifying different microstructural mechanisms during hot deformation of materials

namely superplasticity, flow localization, kinking, prior particle boundary cracking, etc., as shown in Figure 1.6 (Prasad, Rao and Sasidhara 2015).

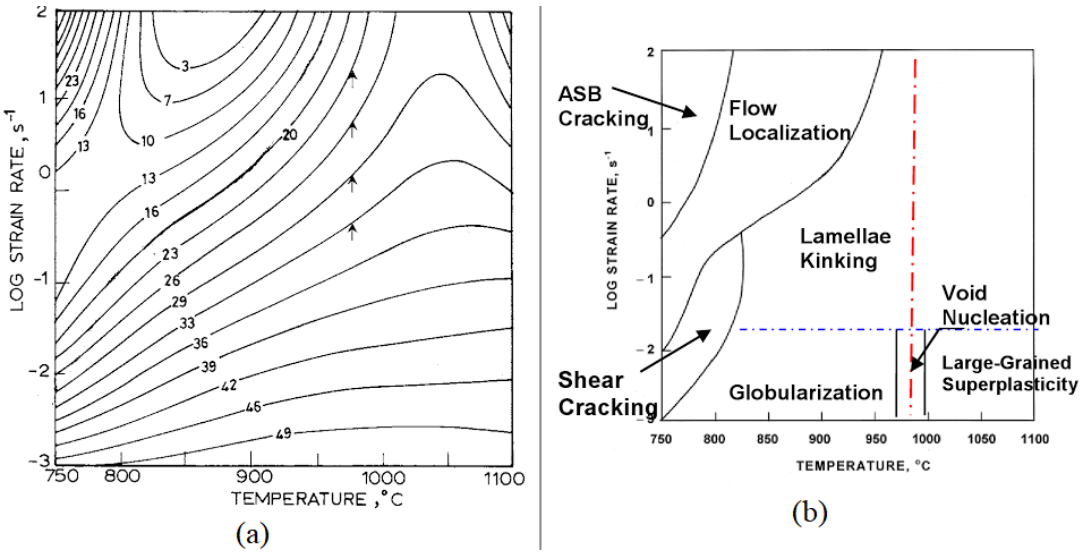

Figure 1.6 (a) Processing map generated using ELI Ti-6Al-4V alloy and (b) its interpretation (Prasad, Rao and Sasidhara 2015)

Superplasticity is regarded as one of the safe hot deformation mechanisms and can be predicted by using a processing map (T. Seshacharyulu, S. C. Medeiros, et al. 2000). Ideally, for a superplastic deformation range, the efficiency will be high, wherein efficiency describes dissipation of energy via growth of the microstructure (Prasad and Seshacharyulu 1998). Further, the efficiency can be improved by reducing the strain rate in the absence of instability within the region.

Processing maps can be utilized in two ways: primarily, for a new metal or alloy, the process can be considered to ensemble the constitutive necessities for optimal workability and microstructural control. Secondly, the existing processes can be improved and appropriate methods can be recognized such that the quality and yield of manufactured components increase (Prasad, Rao and Sasidhara 2015).

Therefore, processing maps can be used in the final control of microstructure, to enhance the process performance ultimately. Also, microscopic or macroscopic defects or flow instabilities can be avoided in order to achieve accurate hot deformation processes (Liu, Hui, et al. 2019). Processing maps identify optimal parameters that can be applied in the sheet metal forming processes to obtain the required results.

1.3. Sheet Metal Bending

In order to study the spring back behaviour in Ti-6Al-4V alloy, sheet metal bending is the most effective sheet metal forming processes. Bending is regarded as the metal forming process that consist of a sheet, which is subjected to the bending stresses. In this process, a flat portion is plastically bended/deformed into a curved portion as presented in Figure 1.7.

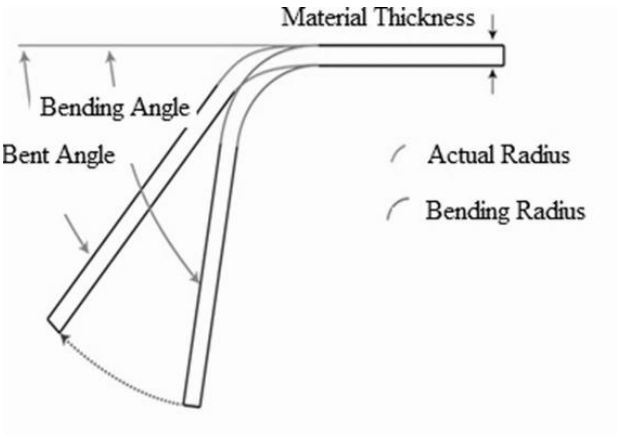

Figure 1.7 Demonstration of a bending process

Bending process is classified into air bending, U-bending and V-bending (Kalpakjian and Schmid 2009). In an air bending, initially blank touches outside edges of both the parts (punch and die). Then, punch forces the blank such that the blank deforms without contacting the bottom of the blank with the die as shown in Figure 1.8 (a).

Bending is classified based on the geometry i.e., if bending is performed using a U-shape die, then it is known as U-bending process as presented in Figure 1.8 (b). If bending is performed using a V-shape die, then it is known as the V-bending process as shown in Figure 1.8 (c). Among these bending processes, V-bending is the most functional process.

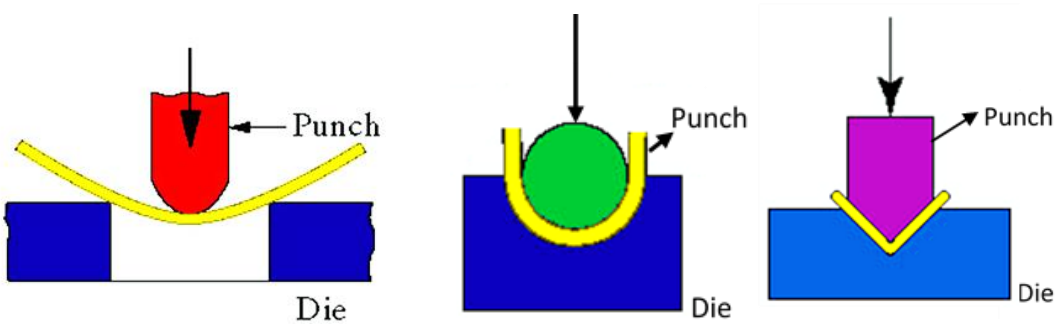

(a) (b) (c)

Figure 1.8 Bending processes (a) air bending, (b) U-bending and (c) V-bending

V-bending operation involves the following sequence of stages: (a) three point contact, (b) partial contact, (c) full contact and (d) punch unloading, as presented in Figure 1.9 (a) - (d) (Zong, et al. 2015).

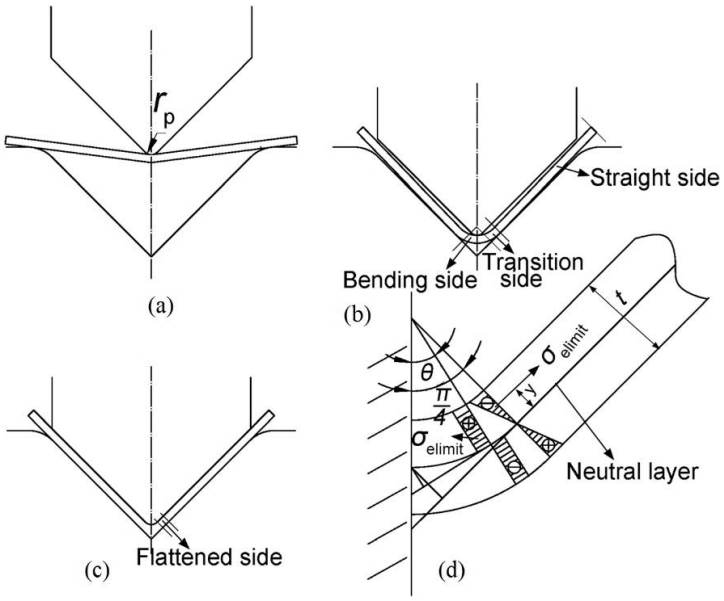

Figure 1.9 Four stages of V-bending (a) Three point contact, (b) Partial contact, (c) Full contact and (d) Punch unloading (Zong, et al. 2015).

In V-bending method, the inside bend radius of the sheet experiences compressive stresses, while the outside bend radius experiences tensile stresses as shown in Figure 1.10 (Ao, et al. 2018). Also, the outside layer elongates, whereas the inside layer undergoes compression.

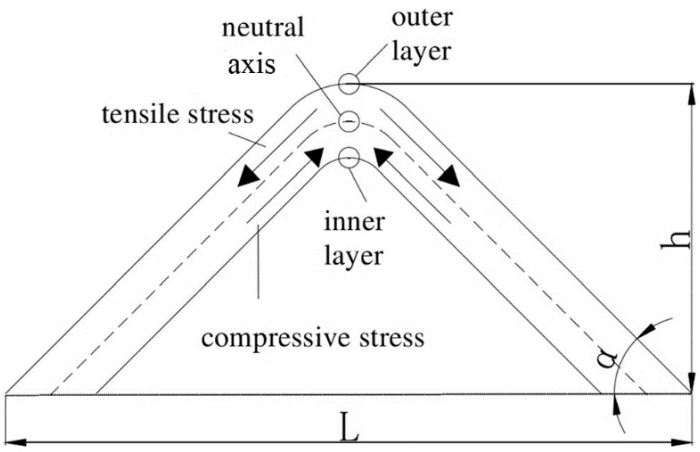

Figure 1.10 Stress state in V-bending (Ao, et al. 2018)

In the inside and outside bend radius, tangential strain (ε_θ) is greater than radial strain (ε_r). Whereas, tangential stress (σ_θ) is larger than radial (σ_r) and transverse (σ_z) stresses (Zong, et al. 2015) . As the material deforms in the tangential direction, transverse strain is ignored, as the transverse bending is prevented for large width to thickness ratio. Stress - strain distribution is presented in Figure 1.11.

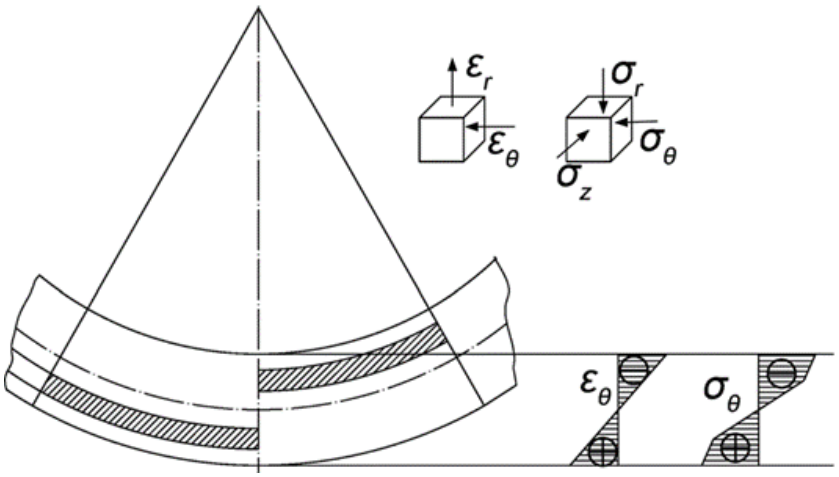

Figure 1.11. Stress – strain distribution in the bending portion (Zong, et al. 2015).

When the metal is deformed outside the elastic limit, then it undergoes into a permanent set (Ozturk, et al. 2010). However, some elasticity remains within the material, due to which spring back occurs during unloading of the punch as presented in Figure 1.12.

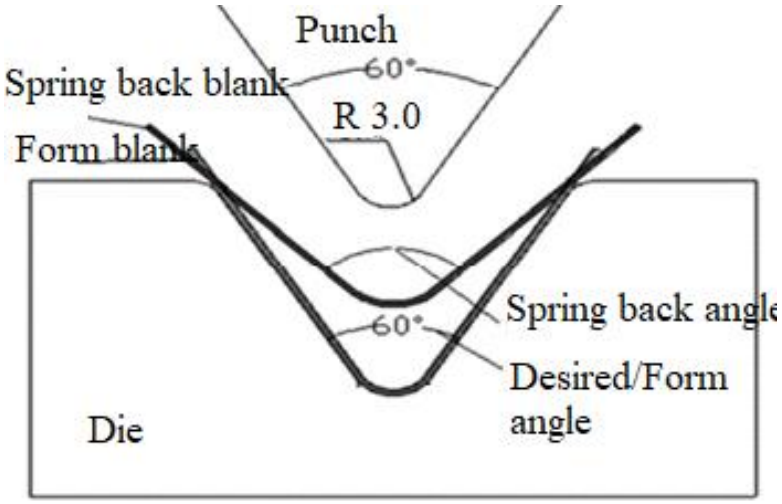

Figure 1.12 Illustration of spring back in V-bending

1.4. Spring back Behaviour

In manufacturing of components, the phenomenon of spring back leads to the geometrical inaccuracies and so it is an important prerequisite to consider spring back while designing the tooling and the assembly process. This is particularly very relevant for titanium alloys as the spring back value can go up to even 30º (Adamus and Lacki 2011). If the given tolerance limit is exceeded, then spring back creates major problems during assembly as well (Banabic 2010).

In V-bending, spring back behaviour is obtained by subtracting the final angle from the initial angle and it can be measured by using a Coordinate measuring machine, bevel protractor, profile projector, etc. Commonly used methods for overcoming spring back are over bending and stretch bending other than the application of high temperature (Dieter 2013).

Spring back is affected by various parameters namely, design of punch and die geometry, type of sheet material and properties, processing conditions and type of bending as presented in Figure 1.13.

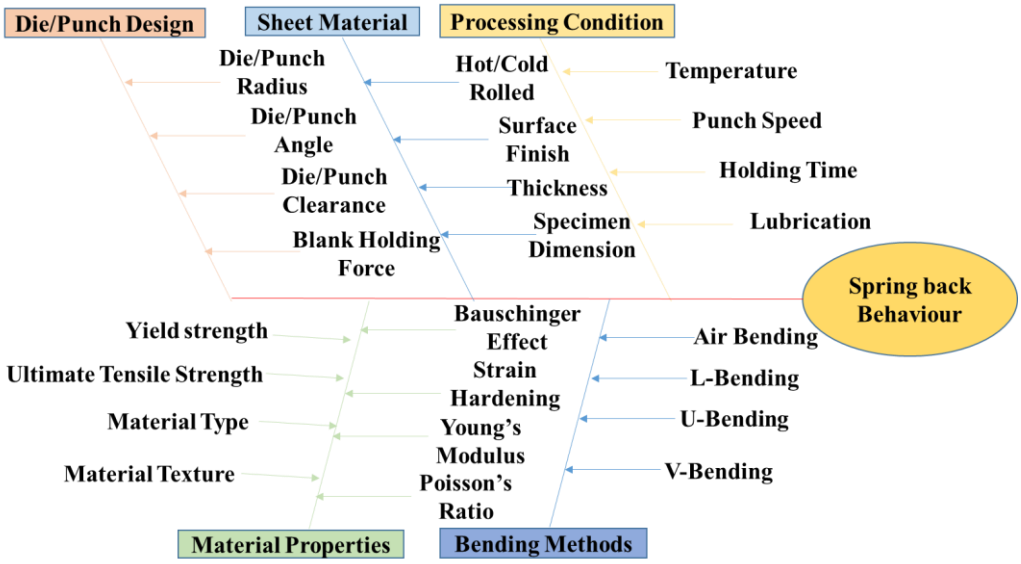

Figure 1.13 Parameters influencing spring back behaviour

Among these parameters, Ti-6Al-4V alloy is susceptible to the Bauschinger effect, where the compressive strength decreases subsequent to tensile straining (Badr, et al. 2015). The Bauschinger effect involves stress strain asymmetry resulting in a hysteresis loop as presented schematically in Figure 1.14. The Bauschinger effect is most pronounced at room temperature and so needs to be considered for spring back evaluation for the forming processes at room temperature. However, increasing the temperature reduces the Bauschinger effect (S. Semiatin 2006) and for the sheet metal bending in hot/superplastic region, it becomes almost negligible.

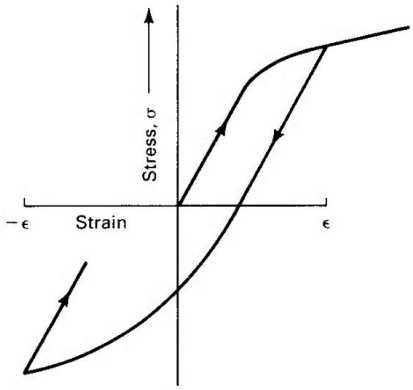

Figure 1.14 Hysteresis loop due to Bauschinger effect (S. Semiatin 2006)

1.5. FE Analysis of Bending Process

In the sheet metal research and industry, FE analysis plays an essential role especially in order to avoid the tedious and time consuming trial and error experimentation on a large scale basis (Papeleux and Ponthot 2002), (Kotkunde, Gupta and Singh 2015). Particularly, accurate prediction of spring back has been substantially improved with FE analysis (Wagoner, Lim and Lee 2013).

To achieve accurate simulation results of spring back using Ti-6Al-4V alloy, proper selection of numerical factors is important such as material model, elastic-plastic data, integration scheme and points, element type, element size and time step (Ablat and Qattawi 2017). Simultaneously, type of method i.e., static or dynamic is also essential in predicting the spring back (Tekkaya 2000).

FE analysis can be performed by using any of the available software package such as ABAQUS, AUTO FORM, INDEED, LS-DYNA, MTLFROM, OPTRIS, PAM STAMP and STAMPACK (Tisza 2004), (Banabic 2010).

1.6. Need of the Study

There is a need to study the spring back behaviour in V-bending of Ti-6Al-4V alloy at high temperatures. For this, first it is important to understand the deformation of Ti-6Al-4V alloy at various high temperatures and strain rates, and develop the deformation processing map and the constitutive model. In order to minimize the spring back, experimental and simulation studies on V-bending of Ti-6Al-4V alloy at high temperatures are required, using which the optimum process parameters can be determined.

Considering all these, the next chapter presents a thorough literature review on deformation behavior, constitutive modeling, processing maps, spring back behavior and its optimization, leading to the gaps in the literature, followed by the research objectives, the methodology and the thesis organization.

CHAPTER 2 : LITERATURE REVIEW

This chapter reviews the major literature including the deformation behaviour, material characterization, constitutive modelling, processing maps and spring back in the bending process followed by research gaps, objectives, methodology and thesis organization.

2.1. Deformation Behaviour and Material Characterization

Deformation behaviour using Ti-6Al-4V alloy acts as a preliminary stage, from where data pertaining to flow stress is obtained for studying different material properties. In this view, Alabort et al. (2015) carried out tensile experiments using Ti-6Al-4V alloy at a constant strain rate and in the temperature range of 700℃ - 950℃. To understand the superplasticity with respect to its characterization, modelling as well as applications, elongations up to 300% were considered and the superplasticity region has been determined to be within the temperature range of 850℃ - 900℃ and at strain rate range of 10^{-3} s^{-1} to 10^{-4} s^{-1}.

Similarly, Salishchev et al. (2001) carried out tensile tests using Ti-6Al-4V alloy from 650℃ - 750℃ and at 10^{-1} s^{-1} - 10^{-4} s^{-1} strain rates, by producing sub microcrystalline grains of 0.3 μm. They stated superplastic properties in this temperature range to be lower than those in other temperature ranges. Some researchers (Patankar, et al. 2002) - (Jalumedi and Dutta 2015) even developed 300 nm and 1-2 μm grained Ti-6Al-4V alloy sheets & performed tensile tests, in order to examine the superplasticity and found better superplastic properties at the considered grain sizes when compared with grain sizes > 3 μm. Although researchers have explored using ultrafine grain materials, but there processing for achieving grain

refinement involved high initial cost as well as greater sensitivity to grain size increment and thus restricting their uses. Thus, superplasticity of Ti-6Al-4V alloy is greatly affected by the initial grain size that reduces the working temperature and also it is governed by the respective microstructural mechanisms.

To investigate microstructural mechanisms, material characterization is performed on the deformed specimens by using different techniques such as Optical Microscope (OM), Scanning Electron Microscope (SEM), Transmission Electron Microscope (TEM), Electron backscatter diffraction (EBSD), X-Ray Diffraction (XRD), etc. In this context, Kim et al. (1999) carried out tensile study on Ti-6Al-4V ($\alpha+\beta$) alloy at 10^{-3} s^{-1} and 600℃ & 900℃, examined the microstructural aspects using TEM and concluded from grain size analysis that the grain boundary sliding in both the phases are meticulously associated with the dislocation motion.

Vanderhasten et al. (2007) examined different microstructural features of Ti-6Al-4V alloy on tensile test specimens conducted at constant strain rate $5x10^{-4}$ s^{-1} and till 1050℃. Based on OM and EBSD studies, it was reported that during the deformation from RT to 950℃, different mechanisms occur at different temperature intervals for instance strain hardening, dynamic recrystallization (DRX), grain growth and grain boundary sliding (GBS).

Liu et al. (2013) used a hybrid metal forming technique in studying the superplastic deformation behaviour of Ti-6Al-4V alloy. Metallurgical investigations were carried out using EBSD and XRD analysis and simultaneously oxidation phenomena has been studied. Based on this, it was reported that DRX was the major mechanism as it takes place in the complete process, whereas cracks and oxidation

were responsible for thickness reduction at a particular location. Also, the effect of oxidation at 800℃ was minimum, when compared with 900℃.

Roy et al. (2013), (2014) investigated the influence of temperature as well as diverse strain rates during deformation of Ti-6Al-4V-0.1B alloy. SEM and EBSD has been utilized pertaining to flow stress, microstructural growth, etc. and compared with Ti-6Al-4V alloy. Results reveal that nonexistence of macroscopic instabilities and early beginning of softening was due to the addition of Boron. Alternatively, Gao et al. (2020) studied the microstructure development and flow response during the sub-transus processing of Titanium alloy with lamellar microstructure. Based on SEM and EBSD studies, it was reported that breaking of lamellar microstructure subsequently to hot deformation plays a main role in modifying the end microstructure.

Bao et al. (2020) carried out a study on electro-pulsing supported by micro scale shear deformation on Ti-6Al-4V alloy using varying current density. For this, two microstructures have been considered, lamellar and equiaxed. Results indicated variation in flow stress and temperature that has contributed in the initiation of shear bands in lamellar microstructure. Whereas, in the equiaxed microstructure, the development of stretched dislocation cells, sub-grains and their break up were the evolutionary procedure of shear bands.

Singh et al. (2020) studied the development of microstructure, spherodization response of alpha laths and different textures in the rolling of Ti407 using SEM and EBSD techniques. Results suggested that initiation of deformation twinning plays an important role in the breaking of alpha laths and substantial texture variation including formation of texture components. Debta et al. (2020) performed rolling

operation till 85% of thickness reduction on Ti-6Al-4V alloy at elevated temperature subjected to annealing. With the help of XRD and EBSD studies, the presence of DRX mechanism was recognized via sub grain formation.

Therefore, based on the above literature, the superplasticity has been recognized when the elongations were greater than 200%, whereas superplastic forming was attained at a specific grain size at high temperatures as well as low strain rates.

2.2. Constitutive Modelling

Generally, the flow stress is modelled as a function of varying strain, strain rate as well as working temperature, which is called as a constitutive model. Researchers have developed various constitutive models, which can be categorized as phenomenological based model, physical based model as well as ANN based model (Lin and Chen 2011). A physical based model was suggested by Picu et al. (2002) by adding thermal and athermal components for investigating the flow stress response, using the experimental data for Ti-6Al-4V alloy at various temperatures as well as constant strain rate i.e., 10^{-3} s^{-1}. In this, the first component includes dislocation interaction using interstitial impurities, whereas the second component includes dislocation interaction using substitutional atoms and precipitates. Both these components fit accurately. Chandra (2002) studied the development of constitutive models at different levels such as macroscopic, mesoscopic and atomistic, to accommodate GBS and suggested that the GBS can be accommodated and modeled accurately at the atomistic level. Huang et al. (2018) developed a constitutive model that consists of temperature aspect as well as its effect on different

factors for studying different mechanism of Ti-6Al-4V alloy and observed that the temperature aspect representing strain hardening and softening mathematically connects classical and modified models appropriately.

Sorgente et al. (2017) examined the superplastic behaviour of Ti-6Al-4V alloy (ELI) at 850℃ by conducting experimentations and simulations managed by genetic algorithm and found that the used approach depending on the power law was proved to be suitable for the modelling of superplastic behaviour. Khan et al. (2012) studied anisotropic behaviour of Ti-6Al-4V alloy from subzero to high temperatures and at diverse strain rates, developing the KHL model with close agreement between the predicted and experimental results.

Kotkunde et al. conducted tensile tests for Ti-6Al-4V alloy varying from room temperature to 400℃ and at different strain rates 10^{-5} s^{-1} - 10^{-2} s^{-1} and applied various constitutive models such as JC, FB, KHL and MTS (2014) (a) and modified-JC model, modified-ZA model as well as RK model (2014) (b). The performance of these constitutive models have been quantified using statistical measures, reporting the better performance of MTS and m-ZA models. Similarly, Tuninetti et al. (2014) developed different set of models such as Norton-Hoff (NH) and CPB06 on the tensile data of Ti-6Al-4V alloy at strain rates 10^{-3} s^{-1} - 10^{-1} s^{-1} and temperature till 400℃ and found that CPB06 model was in close agreement with the obtained experimental results.

To predict the hot deformation response, Zener and Hollomon (1944) initially proposed hyperbolic sine function which is also called as Arrhenius equation. Xiao et al. (2012) applied Arrhenius equation for better modelling of the flow stress response of Ti-6Al-4V alloy at high temperatures as well as low strain rates with

strain till 25% and reported that the results have been in close agreement with the experimental results. Similarly, Zhang et al. (2012) carried out a study to recognize the workability of Ti-6Al-4V alloy during the hot tensile tests from 650℃ - 750℃ and $5x10^{-4}$ s^{-1} - $5x10^{-2}$ s^{-1} strain rates and developed Arrhenius and NH models to evaluate the deformation behaviour and it was reported that both the models accurately predicted the flow stress behaviour under these processing conditions. Porntadawit et al. (2014) investigated the flow stress response of Ti-6Al-4V alloy using hyperbolic sine and the Cingara, the Shafiei and Ebrahimi equations. The material has been deformed from 900℃ - 1050℃ and 10^{-1} s^{-1} - 10 s^{-1} strain rates as per the phase diagram illustrated in Figure 2.1 and found that a combination of these equations predicts the flow stress behaviour accurately.

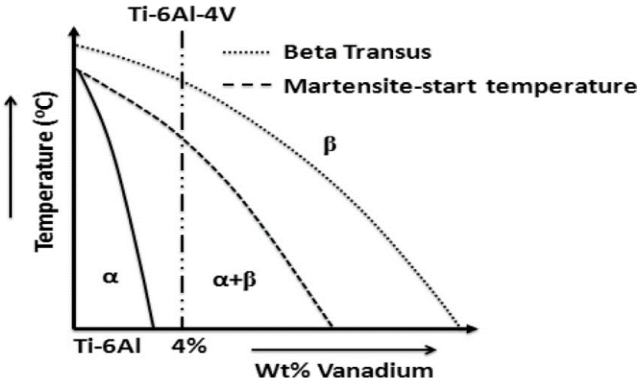

Figure 2.1 Phase diagram of titanium alloys (Porntadawit, Uthaisangsuk and Choungthong 2014)

Jha et al., (2019) studied the deformation response of Ti-6Al-4V alloy using lamellar and equiaxed microstructures from 750℃ - 950℃ and 10^{-3} s^{-1} - 10 s^{-1} strain rates and applied Arrhenius model to compute the flow stress response for both the microstructures and found its predictions to be very accurate. Bodunrin (2020) used Arrhenius model with a reduced gradient for optimizing the material constants and predicted the flow behaviour of Titanium alloy within temperature range of 750℃ -

900°C and strain rate varying from 10^{-3} s^{-1} to 10 s^{-1} and reported that accuracy of the model can be improved by incorporating a reduced gradient. Xia et al. (2020) examined the deformation response of Ti-6Al-4V-0.1Ru from 750°C - 1150°C and 10^{-2} s^{-1} - 10 s^{-1} strain rates and reported that the developed Arrhenius model with material constants (n, α and A) was helpful in accurately predicting the deformation response.

However, to predict the hot deformation response more accurately, Xiao and Guo (2011) introduced the term strain in the Arrhenius equation and developed a modified Arrhenius model. Bao et al. (2020) investigated the hot deformation response of Pb-Mg-Al-B-0.4Y alloy at different processing conditions by applying Arrhenius and modified Arrhenius models and reported that the modified Arrhenius model predicted the hot deformation response more accurately.

Based on the literature, it has been observed that JC, FB, KHL, MTS, etc., were used to accurately predict the flow stress behaviour at elevated temperatures, whereas at high temperatures Arr, m-Arr and the Cingara equations gave better predictions.

2.3. Processing Maps

Processing maps are a graphical representation of hot deformation process in terms of varying strain, strain rate and working temperature, depicting the safe and unsafe region in the given process (Prasad, Rao and Sasidhara 2015). These maps are used for designing a manufacturing process involving hot deformation conditions. In these maps at specified parameters, the power dissipation efficiency is given by a

combination of two integrals i.e., *G* and *J* as presented in Figure 2.2, similarly reported by Liu et al. (2019).

where *G* (dissipator content) indicates power dissipated as the temperature increases and *J* (dissipator co-content) is associated with the microstructural mechanisms. The power setting between the two integrals correspond to strain rate sensitivity (*m*).

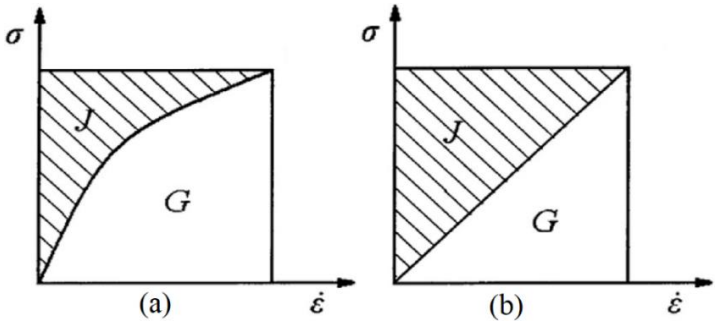

Figure 2.2 Constitutive relationship for (a) non-linear and (b) linear power dissipation (Liu, Hui, et al. 2019)

For non-linear dissipator, *m* varies from 0 to 1 and *m* is equal to 1 for linear dissipator. Prasad et al. (2015) presented a corroboration of the physical model with the processing map as shown in Figure 2.3.

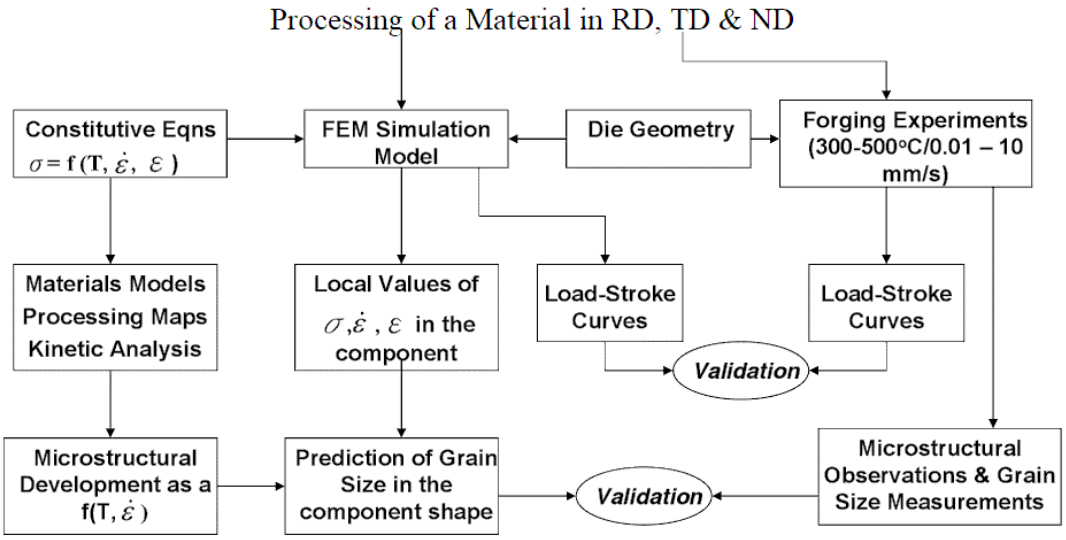

Figure 2.3 Corroboration of physical models with processing maps (Prasad, Rao and Sasidhara 2015)

Researchers have developed processing maps to obtain processing ranges and to achieve microstructure control. Seshacharyulu et al. (2002) performed compression tests on Ti-6Al-4V alloy having equiaxed and lamellar microstructures from 750℃ - 1100℃ and $3x10^{-4}$ s^{-1} - 10 s^{-1} strain rates and constructed processing maps. They reported that for the equiaxed microstructure, alpha grain size enhances in alpha-beta phase and instability occurs at strain rates higher than 1 s^{-1}, whereas for lamellar microstructure, globularization of lamellae takes place from 800℃ - 975℃ and $3x10^{-4}$ s^{-1} - 10^{-2} s^{-1} and instability occurs for strain rates greater than 10 s^{-1}.

Park et al. (2002) investigated the hot deformation response of Ti-6Al-4V alloy by carrying out compression tests from 850℃ - 1000℃ and 10^{-3} s^{-1} - 10 s^{-1} strain rates for developing processing maps and also considered microstructural developments for pancake forgings. Results showed that the stable and unstable regions of processing maps developed for the work-piece agrees well with the experimental results. Similarly, Lypchanskyi et al. (2020) studied the hot flow response of Ti-6246 alloy by conducting hot compression tests at 10^{-2} s^{-1} - 100 s^{-1} strain rates and from 800℃ - 1100℃ and generated processing maps. They reported that the optimum conditions obtained from the processing maps were used in the numerical modelling of forging of Titanium alloy and a confirmation test was also conducted for related forging experiments.

Li et al. (2009) observed the effect of hydrogen on the development of processing maps by conducting compression tests on Ti-6Al-4V alloy from 760℃ - 920℃ and 10^{-2} s^{-1} - 10 s^{-1} strain rates and found that the instable regions differ in the processing maps as the hydrogen content varied. Similarly, Sen et al. (2010) carried out compression tests on Boron modified Ti-6Al-4V alloy varying from 750℃ -

1000°C and 10^{-3} s^{-1} - 10 s^{-1} strain rates and constructed processing maps and reported that size of beta grain reduces on adding Boron and results in unwanted microstructural developments.

Luo et al. (2009) investigated the influence of strain on the construction of processing maps for Titanium alloys by conducting isothermal compression tests from 820°C - 1030°C & 10^{-3} s^{-1} - 10 s^{-1}. They observed that the influence of strain was more significant on beta Titanium than (α+β) & less on alpha Titanium alloy. Zhe et al. (2017) carried out compression tests on TB17 Titanium alloy from 775°C - 905°C and 10^{-3} s^{-1} - 10 s^{-1} strain rates. OM, TEM and EBSD techniques were used for characterization and correlation of unstable regions in processing maps and found that the *m* remains constant in both the phases (α+β) and varied in the beta phase.

Sun et al. (2011) examined the hot deformation response of Ti40 alloy by conducting compression tests from 900°C - 1100°C and strain rates 10^{-2} s^{-1} - 10 s^{-1} and constructed processing maps for studying the hot working behaviour. Results showed that the optimal processing domain was found to be in the range of 1050°C - 1100°C and 10^{-2} s^{-1} - 10^{-1} s^{-1} with occurrence of DRX as the microstructural mechanism. Similarly, Sun et al. (2015) carried out the hot deformation response of TiAl-based alloy by developing activation energy map and processing maps based on the compression test data and reported optimal processing window and correlated regions with the evolution of microstructure involving DRX and cracking. Ghasemi et al. (2017) performed compression tests on Titanium alloy BT9 from 1000°C - 1100°C and 10^{-3} s^{-1} - 10^{-1} s^{-1} strain rates and developed processing maps for correlating DRX and DRV. The maximum power dissipation in these two conditions has been found to be 52% and 46% respectively.

Researchers integrated a standard method of assessing hot deformation performance and compression tests using a material model. Additionally, assessed microstructure by generating processing maps and found that the obtained processing maps were free from the defects in the stable region (Lukaszek-Solek and Krawczyk 2015). Wang et al. (2016) carried out compression tests for Tungsten from 1250℃ - 1550℃ and 10^{-3} s^{-1} - 1 s^{-1} strain rates and to investigate the hot flow response, microstructural characterization, flow stability and instability areas processing maps were constructed and reported that the stable region in the processing maps can be categorized into multiple regions and unstable regions were correlated with respective microstructures. Cai et al. (2016) performed compression tests on Ti-6Al-4V alloy varying from 800℃ - 1050℃ and $5x10^{-4}$ s^{-1} - 1 s^{-1} strain rates and generated processing maps based on different instability conditions as shown in Figure *2.4* and corroborated it using microstructural development (whereas A, B, C, D and E are different microstructure locations with respective instability criteria). Results showed that the efficiency maps were similar for Prasad and Murthy criteria, however the instability maps varied from each other.

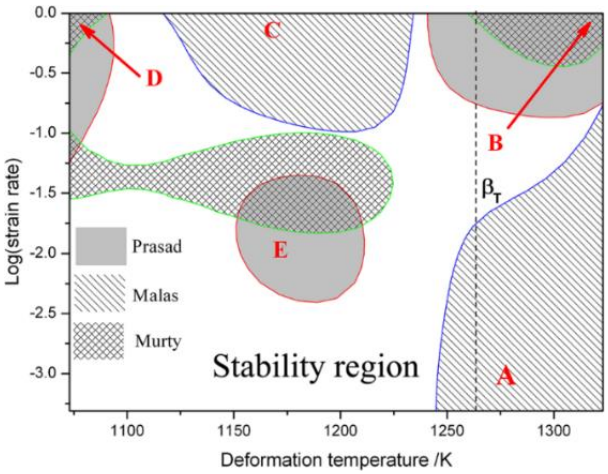

Figure 2.4 Instability maps established by different criteria at 0.5 strain (Cai, et al. 2016)

Saxena et al. (2017) conducted compression tests on Zr-1Nb alloy from 650℃ - 1050℃ and various strain rates 10^{-2} s^{-1} - 10^{-1} s^{-1} and used a new approach to construct the processing maps and noticed that by using this approach, it predicted regions of high power dissipation and simultaneously, correlated with microstructural development. Su et al., (2020) examined the hot compression behaviour of near alpha Titanium alloy from 975℃ - 1100℃ and at 10^{-2} s^{-1} - 1 s^{-1} and obtained the optimum processing range by developing processing maps.

Quan et al. (2020) performed compression tests at various temperatures as well as strain rates to generate processing maps. They have mapped the process parameters with microstructural mechanisms in 3D space as shown in Figure 2.5 and separated DRX from grain refined parameter. Simultaneously, they have developed FE model for better understanding and obtained the optimum parameters for loading paths. Similarly, Zhou et al. (2020) constructed 3D processing maps based on compression test data for Ti-2.7Cu alloy at high temperatures and different strain rates. They reported that unstable regions occur due to flow localization and mechanical instability, whereas the stable region occurs due to DRX as presented in Figure 2.6.

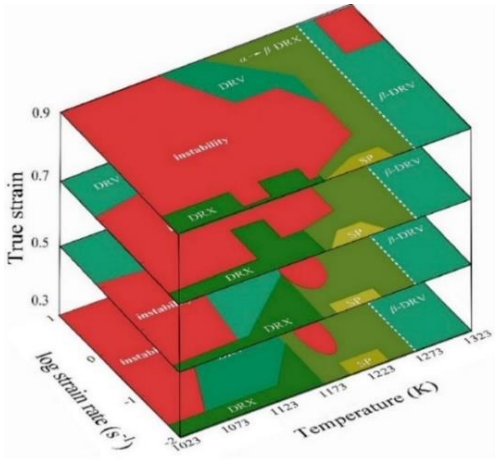

Figure 2.5 Three dimensional deformation map of Ti-6Al-4V (Quan, et al. 2020)

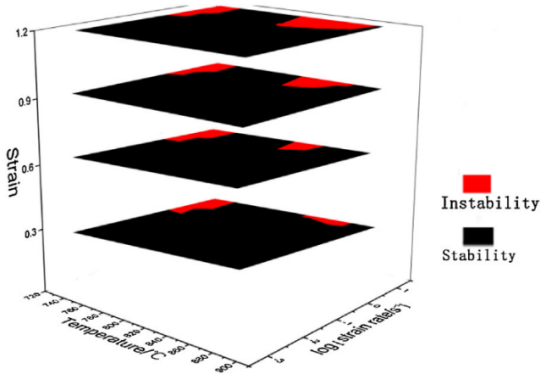

Figure 2.6 A three dimensional instability map of Ti-2.7Cu alloy (Zhou, et al. 2020)

Thus, based on this literature review, it has been recognized that most of the work has been conducted with respect to compression testing of different materials at high temperatures and different strain rates in the development of processing maps.

Next section deals with literature review emphasizing on the spring back based on different parameters.

2.4. Spring back Studies

A number of research works were reported on the spring back effect for different bending process such as air bending, U-bending and V-bending at ambient temperature. Santos et al. (2004) presented experimental results carried out on stamping operation using aluminium alloy and steel performed by various institutions and validated it with the benchmark simulation results. Panthi et al. (2007) applied a TEIP algorithm in the modelling of sheet bending process of structural steel and used it in FEA for investigating the influence of load on the spring back behaviour with changing thickness along with die bend radius and found that the simulation results were reasonably accurate with the obtained experimental results. Leu et al. (2016) investigated the spring back effect of HSS by considering strength, varying punch radius and varying sheet thickness and the experimental effects of these process

parameters were validated with numerical simulations. Li et al. (2016) suggested a method for calculating the bending moments of 2024Al alloy with varying curvature and also, predicted spring back behaviour. Results showed that the suggested method agrees well with the experiments and simultaneously validated with the numerical results.

Karaagac (2016) investigated bending of copper as well as brass in flexforming operation and conventional operation for diverse holding times, varying angles along with the pressure and reported that surface flaws did not exist in the flexforming operation when a comparison has been made with the conventional operation. Furthermore, they implemented fuzzy logic for evaluating the spring back and noticed that it agrees closely with the experimental results. Cui et al. (2020) carried out a comparative study between electromagnetic supported stamping (EMAS) involving magnetic force and conventional EMAS for reducing spring back. Results showed that equivalent plastic strain and plastic energy improves, whereas tangential stress, elastic strain energy and spring back reduces considerably as discharge voltage increases.

Tekiner (2004) performed an experimental investigation to understand the spring back effect on sheet metal components for aluminium, brass, copper, galvanizing iron and stainless steel by varying bending angles in V-bending dies and found that the applied methods predicted spring back results accurately. Chan et al. (2004) implemented FEA using AL2024-T3 for calculating the spring back effect during V-bending process and considered punch and die lip radii along with punch angle and noticed that spring back eases with the growth of punch radius along with punch angle.

Thipprakmas and Phanitwong (2011) studied spring-back as well as spring-go/negative spring-back effect in the V-bending simulations using A1100 as shown in Figure 2.7. They considered process parameters like thickness, varying punch radius as well as bending angle depending on Taguchi method and observed that the thickness along with bending angle were found to be the major contributors in decreasing spring-back as well as spring-go. Chen et al. (2014) studied the influence of grain size on pure iron during the micro V-bending operation using parameters such as punch radius and varying punch speed and reported that spring-back minimizes with increase in punch speed in case of smaller grains, whereas spring-go reduces with decrease in punch speed in case of larger grains.

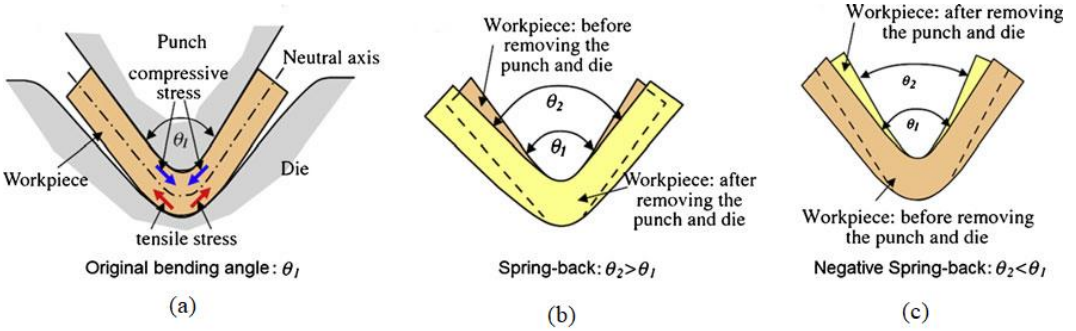

Figure 2.7 V-bending in (a) loading of punch, (b) spring back and (c) negative spring back (Teimouri, et al. 2012)

Badr et al. (2015) studied the influence of spring back on Ti-6Al-4V alloy during roll forming as well as V-bending operations and observed that less spring back occurs during roll forming operation when compared with the bending operation. Ramadass et al. (2019) examined spring back behaviour of Ti grade 2 alloy in V-bending process and considered parameters as thickness variation, punch radius besides die opening and designed them using Taguchi method and found that the thickness has the main effect in minimizing the spring back.

All the above spring back studies were conducted at room temperature. However, due to low formability and high spring back in Titanium alloys, these are formed at high temperatures to reduce spring back effect. Researchers described that spring back behaviour reduces as the temperature increases, typically because of the reduction in the yield strength, Boyer et al. (1994), Dieter (2013) and Kalpakjian & Schmid (2009). Ozturk et al. (2010) examined the influence of warm temperature taking place on spring back for Ti-2 alloy and found that with the rise of temperature spring back reduces substantially.

Shong et al. (1983) observed the significance of hot sizing using different Titanium alloys and reported that hot sizing works as an amalgamation of softness and stress relaxation for decreasing spring back behaviour. Odenberger et al. (2011) explored the prospects of designing different hot forming tools using FE analysis for Ti-6Al-4V alloy and reported a range of temperature and springback could be further decreased by using hot sizing.

Zong et al. (2015) studied springback behaviour of Ti-6Al-4V alloy in the V-bending process varying from RT - 850℃ at a fixed punch speed and diverse punch radius and reported that spring-go occurs for small punch radius, whereas spring-back with larger punch radius. Liu et al. (2019) investigated the deformation route and spring back behaviour of Ti-6Al-4V alloy varying from 700℃ - 750℃. Results showed that the deformation undergoes uneven strain distribution and there has been a slight rise in the spring back from centre to the middle section.

Based on this literature, different parameters have been identified i.e. punch design and die design, temperature domain, punch speed, holding time, varying sheet thickness, die opening, bending angle, etc., for understanding the influence of spring

back behaviour. In order to minimize the spring back behaviour, researchers have applied various optimization techniques, which are reviewed in the next section.

2.5. Optimization Techniques for Spring back Behaviour

For minimizing spring back effect, researchers have used various optimization techniques such as RSM, GA, ANN. Han and Lee (2009) suggested a new RSM method that makes sure of constraint possibilities regarding the best result. Alvarez et al. (2009) discussed the significance of applying GA plus RSM and found that this combination works as a useful tool in getting the optimized process parameters.

Sousa et al. (2006) carried out a study on the optimization of V and U-bending operations by generating an algorithm and adding it to genetic algorithm (GA). They have considered process parameters as punch along with die radii, blank holding force as well as punch shift and reported that the developed algorithm added to GA has been effective in optimizing both the bending processes. Liu et al. (2007) used a neural network as well as GA based technique to resolve the spring back problem and reported that by using this technique, the spring back has been estimated accurately.

Teimouri et al. (2012) carried out a study on the modelling as well as optimization of positive and negative spring back in the V-bending operation. They have considered process parameters as punch radius, varying thickness as well as sheet orientation and reported that the prediction of spring back by radial basis network was better when compared with other models. Gupta (2010) considered different optimization methods such as response surface method (RSM) along with support vector regression as well as ANN to optimize parameters and reported that

the considered methods were very much suitable with acceptable goodness of fit in the optimization of process parameters.

Liu et al. (2007) developed a multi optimization platform from where CAD and CAE tools can be interrelated and found that this platform improves the design and analysis of automation and reduces human error. Wiebenga et al. (2012) presented a robust method for optimizing the time consumption during V-bending simulations and found that considerable development and stability has been accomplished for the deteriorating effects involving noise variables. A broad classification of various statistical methods has been presented, to optimize the parameters and their uses depending on the requirements by Montgomery (2017).

Few investigations have been reported pertaining to experimental and numerical studies on deformation behaviour using Ti-6Al-4V alloy at lower elevated temperatures. The earlier investigations were primarily focused on experimental and numerical characteristics of different deformation processes. The major concerns that were noticed in the earlier works pertaining to Ti-6Al-4V alloy comprises of low deformation and high spring back at ambient temperature and oxidation effect beyond 400°C.

Some reports on material properties and processing maps generation using Ti-6Al-4V alloy specified the safe working range could be at the high temperatures (preferably in the hot working temperature domain for a particular material). Furthermore, less concentration has been made on the thorough experimental and numerical investigation of spring back in the hot working conditions.

Based on the broad literature on deformation behaviour, material characterization, constitutive modelling, processing maps, experimental or numerical

investigation of spring back and optimization of spring back, research gaps have been identified and presented in the next section.

2.6. Research Gaps

Based on the comprehensive literature survey, the following research gaps have been identified:

- Ti-6Al-4V alloy exhibits poor formability and high springback effect at cold working conditions due to limited ductility, low strain hardening exponent and high elastic recovery.
- Formability of Ti-6Al-4V alloy can be enhanced to some extent at warm forming ($0.3T_m$ to $0.5T_m$) conditions, however the springback effect is still significant. Thus, forming of complex shape components with minimal elastic recovery is considered as a challenge for Ti-6Al-4V alloy.
- Recently, few studies have reported that Ti-6Al-4V alloy displayed superplasticity at hot deformation conditions. The significant enhancement in ductility has been noticed in superplastic range, which helps to form complex shape components.
- Also, it is important to develop constitutive model and processing maps at high temperature conditions and optimization of spring back to near-zero values.

Thus, it is essential to thoroughly understand the deformation and springback behaviour of Ti-6Al-4V alloy at high temperatures. Based on these research gaps, objectives of this study have been finalised and presented in the next section.

2.7. Objectives of the Study

The main research objectives of the study are identified as follows:

1. Study of deformation behaviour and microstructural analysis at high temperatures (700℃ - 900℃).
2. Constitutive modelling and development of processing maps for Ti-6Al-4V alloy at high temperatures for different strain rates.
3. Experimental study of spring back behaviour in the V-bending process at high temperatures (700℃ - 900℃).
4. FE modelling of springback behaviour in the V-bending process at high temperatures for Ti-6Al-4V alloy.
5. Optimization of process parameters for minimizing springback effect and its experimental validation.

2.8. Methodology

The main objective of this research work has been to study the deformation behaviour, processing maps and spring back behaviour using Ti-6Al-4V alloy at high temperatures varying from 700℃ - 900℃. The thorough investigation of material properties along with flow stress response is necessary to understand the deformation behaviour. In this context, material properties and flow stress response has been evaluated from 700℃ - 900℃ at a gap of 50℃ (700℃, 750℃, 800℃, 850℃, 900℃) and within a strain rate range varying from (10^{-2} s^{-1} to 10^{-4} s^{-1}) by means of tensile tests. Microstructural and XRD studies were carried out on the fractured samples.

The flow stress data of Ti-6Al-4V alloy acquired from the tensile tests have been used for developing the constitutive model for accurately predicting the hot

tensile response. Furthermore, processing maps were generated for understanding the superplastic deformation response of Ti-6Al-4V alloy and from this, stable regions have been identified for confirming superplasticity, whereas unstable regions were correlated with microstructure studies. Lastly, superplasticity of Ti-6Al-4V alloy was confirmed from material properties, material characterization and processing maps.

The material properties acquired using the tensile tests data were used in the FE Analysis, to perform V-bending simulations using different process parameters based on full factorial design. From V-bending simulations, the spring back results of Ti-6Al-4V alloy were obtained and validated with the experimental results as per the Taguchi method L_9 orthogonal array design. Finally, the process parameters from the full factorial simulations were optimized to get an optimum setting and confirmed through simulation and experimentation. The complete methodology is presented in Figure 2.8.

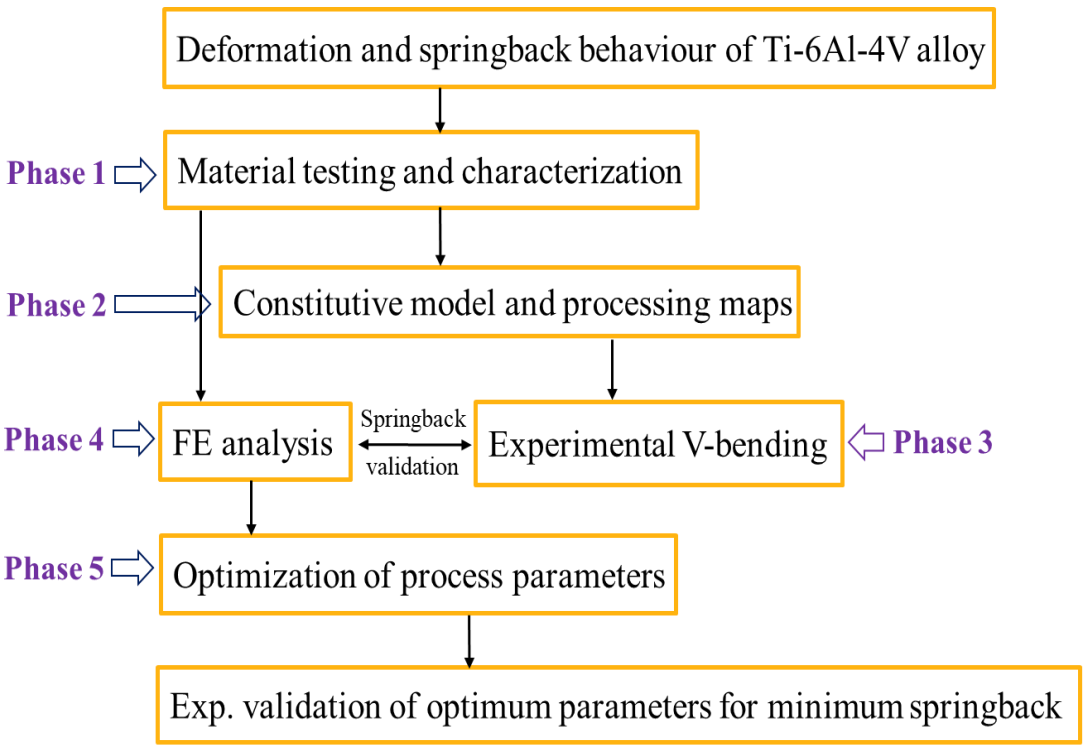

Figure 2.8 Methodology adopted in this study

2.9. Thesis Organization

The thesis has been organized in seven chapters as presented below.

Chapter 1 consists of a broad introduction of Ti-6Al-4V alloy, constitutive modelling and processing maps followed by a discussion on sheet metal bending, FE modelling and analysis and need of the study.

Chapter 2 presents an extensive literature review of deformation behaviour, material properties and characterization, constitutive modelling, processing maps, spring back studies and optimization of spring back. In addition, research gaps, thesis objectives and the adopted methodology have been presented.

Chapter 3 covers determination of different material properties at high temperatures and various strain rates. For material characterization, OM, SEM and XRD studies have been presented.

Chapter 4 involves development of constitutive model as well as processing maps depending on the flow stress data acquired from high temperature tensile tests. The developed processing maps have also been analyzed for different instability criteria.

Chapter 5 consists of experimental study of V-bending process considering different process parameters to evaluate spring back. It also presents analysis of variance for finding out the most prominent process parameters.

Chapter 6 comprises of FE modelling of V-bending process based on full factorial design and optimization of spring back effect using RSM and GA. The optimum results have been validated with the experimental findings.

Finally, Chapter 7 presents salient conclusions, limitations and future work. The complete thesis organization is presented in Figure 2.9.

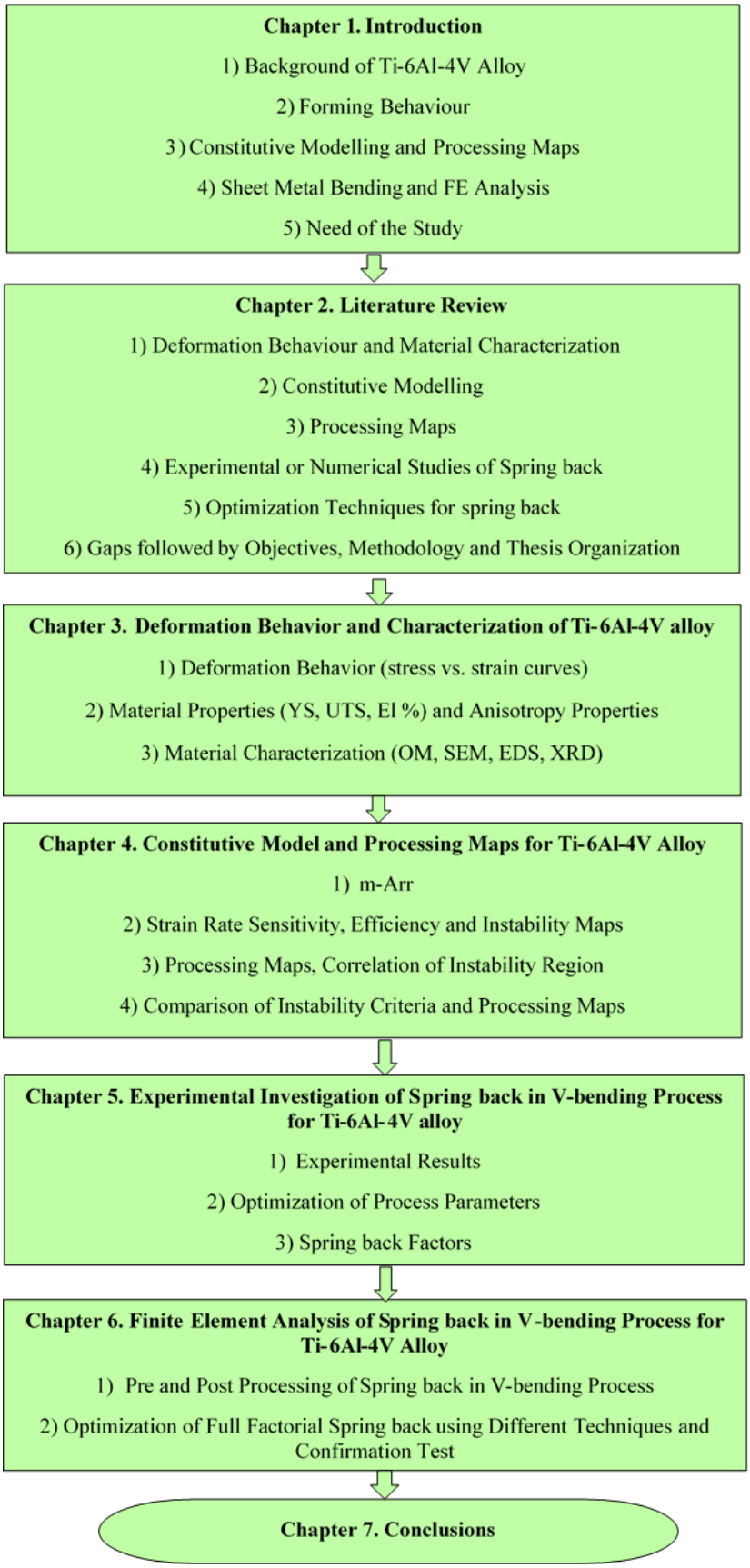

Figure 2.9 Thesis organisation

CHAPTER 3 : DEFORMATION BEHAVIOUR AND CHARACTERIZATION OF TI-6AL-4V ALLOY

This chapter presents deformation behaviour followed by determination of different material and anisotropic properties and characterization of Ti-6Al-4V alloy at high temperatures and various strain rates as presented in Figure 3.1.

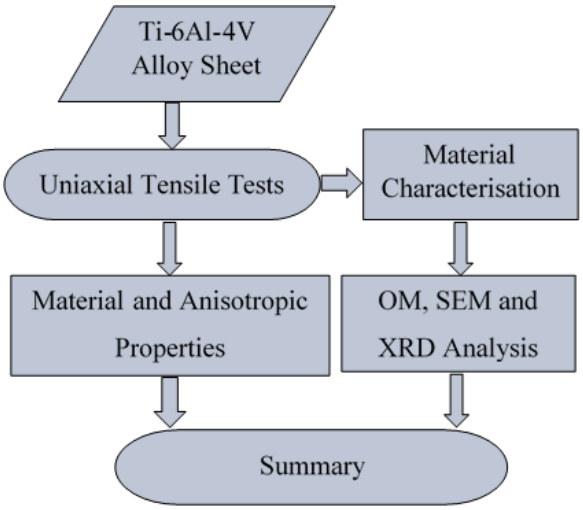

Figure 3.1 An overview of the chapter

3.1. Experimental Details

For tensile tests, 1.3 mm thick Ti-6Al-4V alloy sheets were received with a chemical composition as presented in Table 3.1. Figure 3.2 illustrates the optical and SEM images of initial equiaxed microstructure of Ti-6Al-4V alloy showing dual phase alpha (α-Ti) and beta (β-Ti) fine grains.

Table 3.1 Chemical composition of as-received Ti-6Al-4V alloy sheet (% wt.)

Al	V	Fe	C	O	N_2	H_2	Ti
5.980	4.070	0.220	0.020	0.120	0.030	0.010	Balance

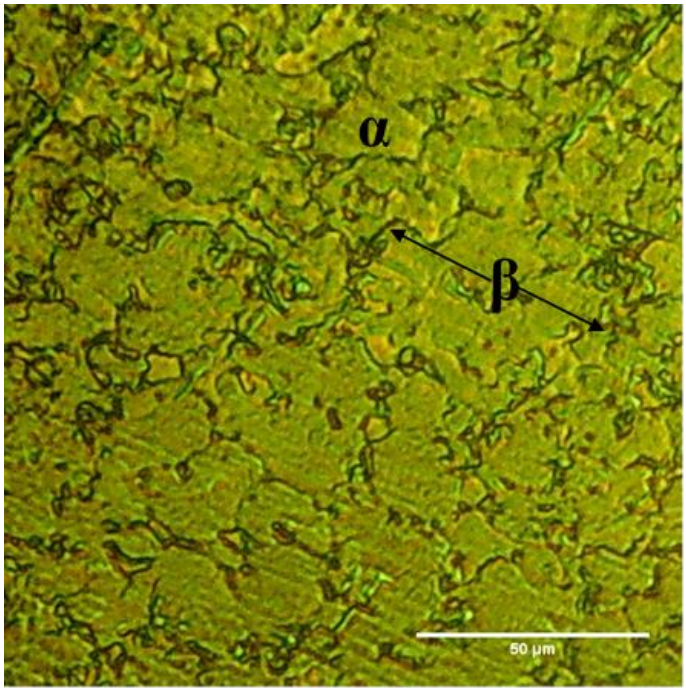

(a)

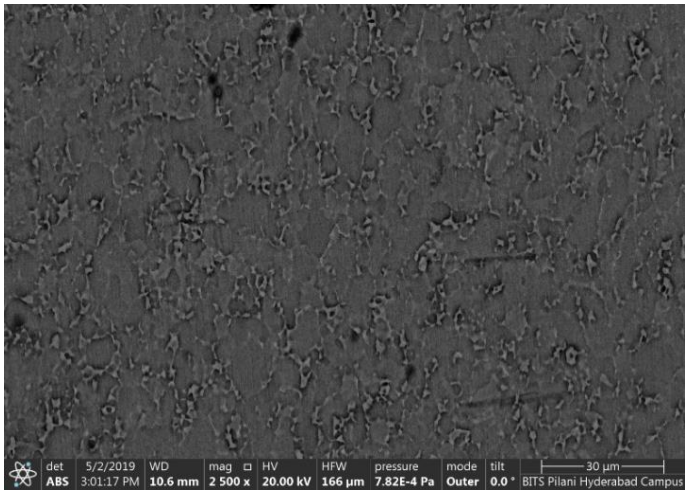

(b)

Figure 3.2 (a) Optical image and (b) SEM image of initial Ti-6Al-4V alloy

The tensile specimens were prepared from as-received Ti-6Al-4V alloy sheet using a wire-cut Electro Discharge machining for obtaining burr free specimens, following the sub-sized ASTM standard dimensions (E8/E8M-11), which are presented in Figure 3.3.

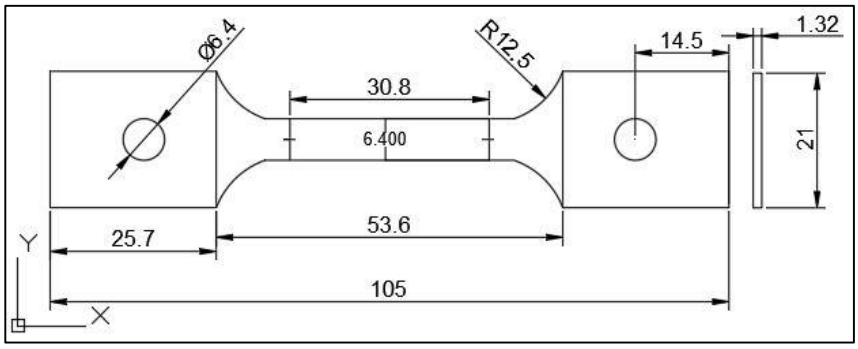

Figure 3.3 Tensile test specimen (all dimensions are in millimetre)

Tensile tests were performed at high temperatures ranging from 700°C to 900°C within a gap of 50°C and at various strain rates 10^{-1} s^{-1} - 10^{-4} s^{-1}. A computer controlled 50 kN Universal Testing Machine (UTM) as illustrated in Figure 3.4 (a) has been used for carrying out tensile tests at constant strain rates. UTM is equipped with a split furnace as shown in Figure 3.4 (b) with a temperature capacity up to 1000°C and temperature measurement precision up to ±5°C using K-type thermocouples.

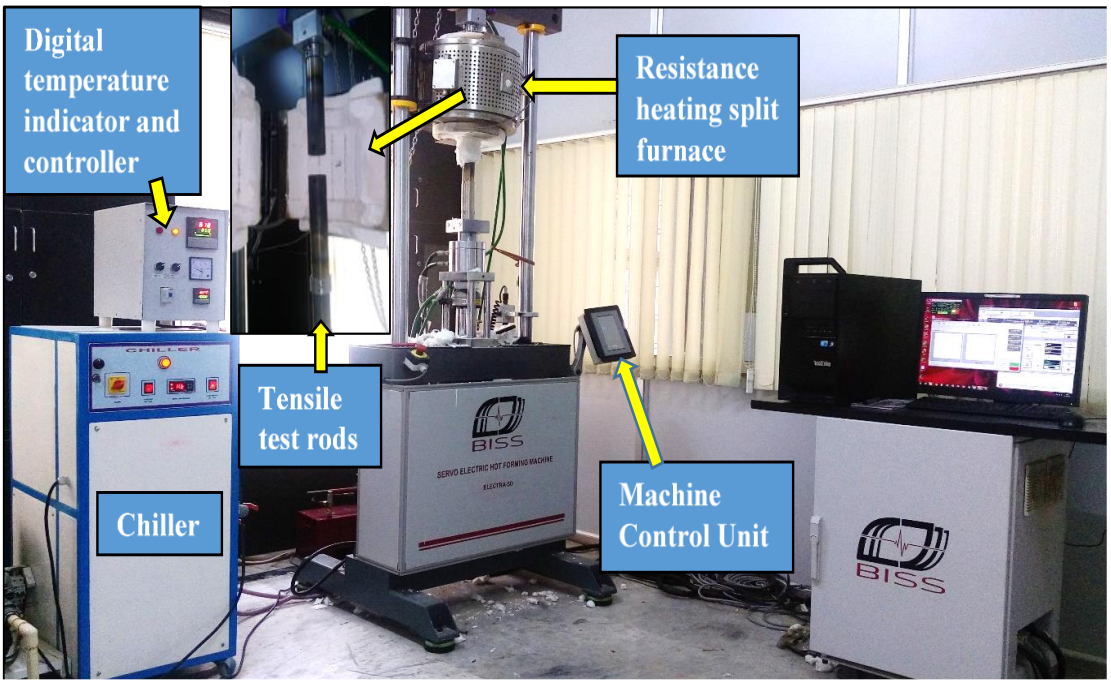

(a)

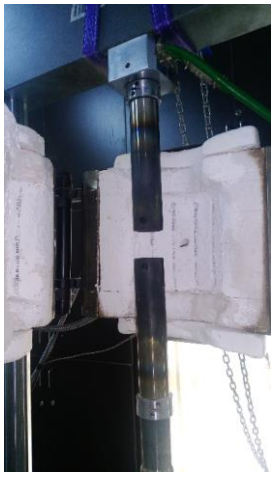

(b)

Figure 3.4 (a) Computer control UTM of 50 KN capacity and (b) diverse temperature split furnace

In order to avoid oxidation effect during high temperature tensile testing, a thin layer of delta glaze liquid coating has been applied on the specimens. It forms a glass-like layer on the sheet metal, when comes in contact with high temperatures, and thus prevents surface oxidation. The specimens have been heated at a rate of 10℃/min and then held at the desired temperature for minimum three minutes in order to stabilize the temperature. This has been followed by tensile test till rupture and subsequent annealing as shown in Figure 3.5. Each experiment has been conducted thrice to ensure repeatability of results.

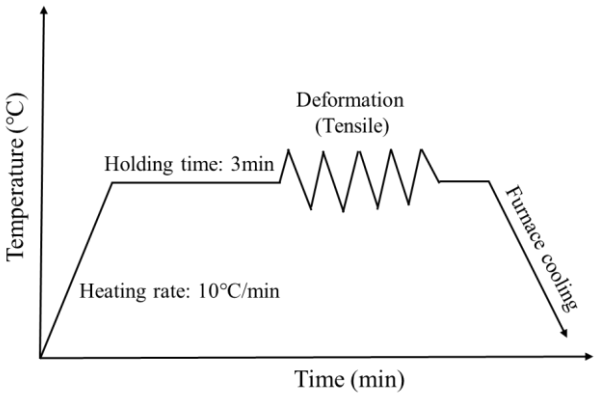

Figure 3.5 Heating and cooling of Ti-6Al-4V alloy tensile specimens

For microstructural study, the metallographic samples have been cut within the gauge length from the fractured tensile test specimens and hot mounted for surface polishing using various grades of emery papers. For attaining mirror surface finish on the samples, lapping has been performed on a velvet cloth mounted on a polishing machine using plenty of H_2O (water) as well as diamond paste and etched using Kroll's reagent as an etchant (4 ml HF + 12 ml HNO_3 + 84 ml H_2O).

Etched samples consisting of microstructure has been visually observed at various magnifications using an Optical Microscope (OM). Image J digital processing software was used to calculate the average void size and grain size, and also, to quantify the area and volume fraction of the phases present.

For fractography and microstructure, investigations have been carried out along the surface and on the broken area of the sheared samples by using a high resolution SEM - made by Carl Zeiss Company - Model was EVO - 18.

XRD analysis have been carried out on the fractured tensile samples by means of copper source having λ (lambda) = 1.54 Å with the help of scintillation counter sensor of Rigaku company and Model was ULTIMA IV.

3.2. Mechanical Behaviour of Ti-6Al-4V Alloy at High Temperatures

For understanding the mechanical behaviour of Ti-6Al-4V alloy at high temperatures, tensile tests were conducted at different strain rates (10^{-1} s^{-1} - 10^{-4} s^{-1}) and temperatures (700℃ - 900℃). These deformed tensile test specimens have been presented in Figure 3.6, displaying the percentage of elongation (ductility) up till fracture. Superplasticity range of Ti-6Al-4V alloy occurs from 750℃ - 900℃ at 10^{-4} s^{-1} and it can be seen from Figure 3.6 that the complete elongation till rupture is

greater than 200%. Also, *m* values for these parameters lie in the range of (0.3 - 0.8), signifying superplastic deformation behaviour of Ti-6Al-4V alloy, as reported by Giuliano (2011) and Tuoyang et al. (2014).

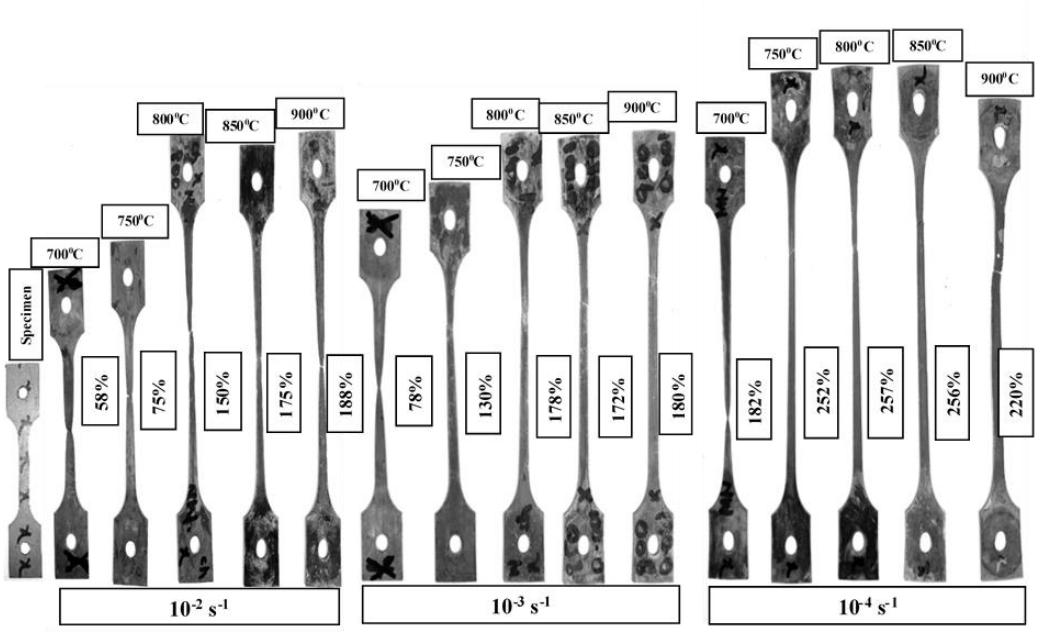

Figure 3.6 Tensile tested specimens exhibiting overall elongation till fracture

Stress vs. strain curves at high temperatures and various strain rates are presented in Figure 3.7. It can be observed that flow stress values are greater at lower elevated temperatures along with high strain rates as compared to those at higher temperatures along with low strain rates.

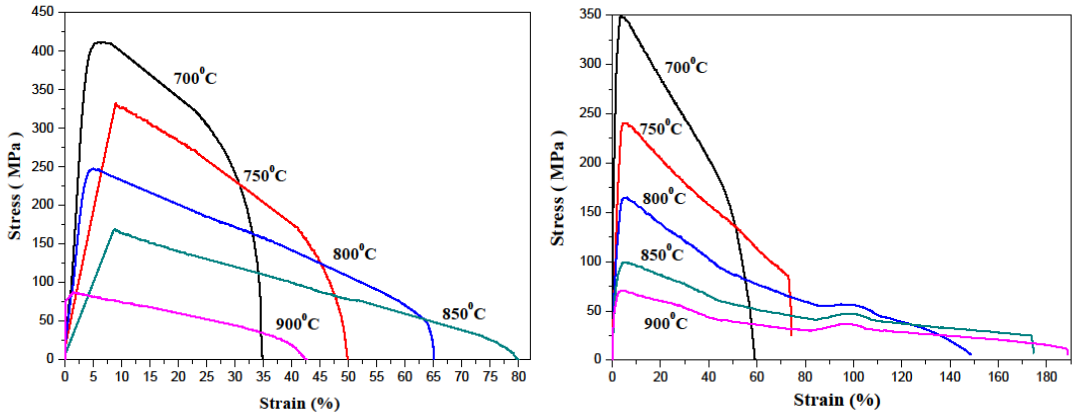

(a) (b)

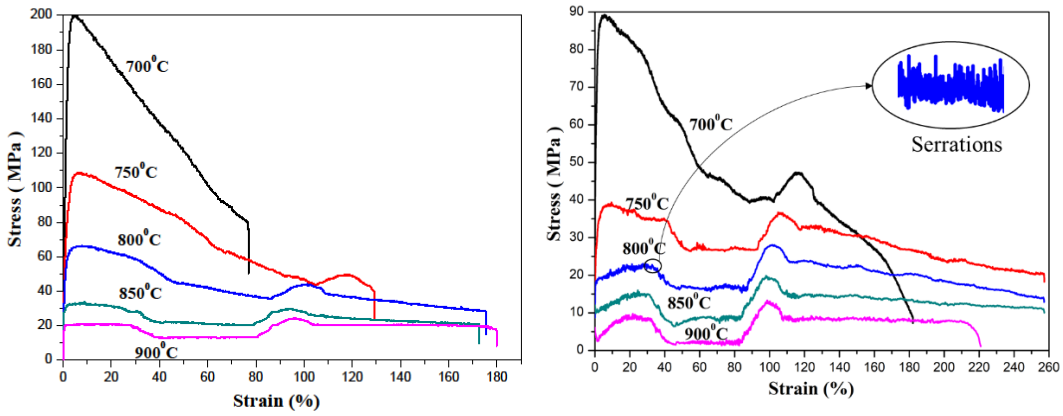

(c) (d)

Figure 3.7 Stress vs. strain curves in Ti-6Al-4V alloy along 0° orientation conducted at high temperatures and various strain rates (a) 10^{-1} s^{-1}, (b) 10^{-2} s^{-1}, (c) 10^{-3} s^{-1} and (d) 10^{-4} s^{-1}

At 10^{-2} s^{-1} and 700°C, the elongation is 60%, which improves with the rise of temperature and reduction in the strain rates till 260% even though superplasticity (greater than 200% of elongation) is attained only at 10^{-4} s^{-1}. From these figures, it may be inferred that stress vs. strain curves show large elongations till fracture due to flow softening.

In Figure 3.7 (d), stress vs. strain curves starting from 750°C exhibit very high elongations. It is because of lowest strain rate as well as higher temperatures due to which it achieves superplasticity. Also, it might be due to sliding of grain boundaries (GBS) by means of parallel reduction of stresses generated on grain boundaries of triple junctions. It includes diffusion of atoms in order to improve flow ability, as reported by Seshacharyulu et al. (2000).

Serrations can be observed in these figures, as highlighted in Figure 3.7 (d), it might be due to the competing nature of strain hardening along with strain softening, similarly observed by Tuoyang et al. (2014). Small humps have been observed at higher strain rates, it could be due to reorientation of primary unfavorable

direction of alpha to other favorable directions, as reorientation of alpha probably affects the flow response due to initial texture, as stated by Roy et al. (2014). The size of hump increases at a lower strain rate, it might be due to increased GBS, as reported by Roy and Suwas (2013).

Ti-6Al-4V alloy is subtle to strain rate i.e., stress vs. strain curve varies with the strain rate as presented in Figure 3.8. From Figure 3.8 (a), it has been perceived that as the strain rate reduces flow stress also reduces and a similar trend has been observed from Figure 3.8 (b).

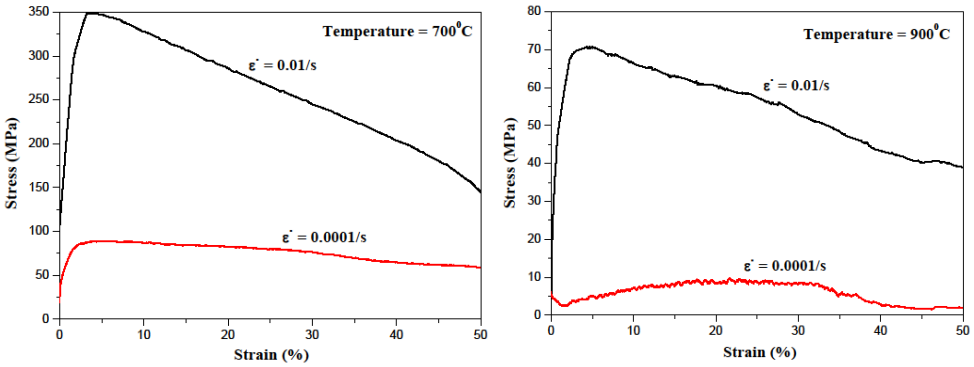

(a) (b)

Figure 3.8 Strain rate sensitivity of Ti-6Al-4V alloy at (a) 700°C & (b) 900°C

Stress vs. strain data has been utilized for calculating (a) 0.2% offset i.e., Yield strength (YS), (b) tensile strength (Ultimate) (UTS) and (c) Ductility/Elongation (El %). Figure 3.9 show graphs with difference in properties related to high temperatures and strain rates. From Figure 3.9 (a) and (b), it has been noticed that YS reduces from 80% - 97% and UTS reduces from 80% - 91% as temperature rises and at different strain rates, it could be because of thermal softening, dislocation mobility as well as activation of atoms. Figure 3.9 (c) indicates that El % rises from 21% - 224% with temperature and various strain rates owing to thermal softening. From 700°C - 900°C and 10^{-2} s^{-1} - 10^{-3} s^{-1}, El % is < 200%, while at 10^{-4} s^{-}

[1] and from 750℃, El % rises > 200%, demonstrating superplastic behaviour of Ti-6Al-4V alloy, similarly reported by Leyens and Peters (2003), Giuliano (2011).

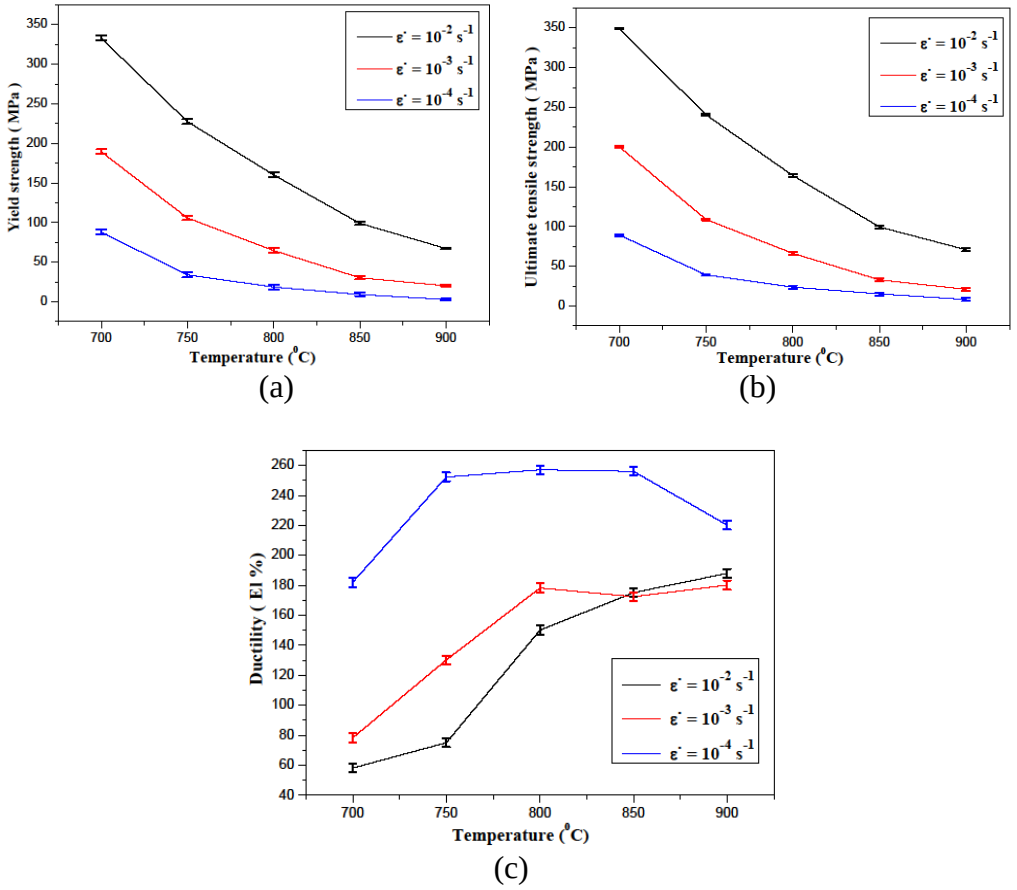

Figure 3.9 Graphs representing difference of (a) YS, (b) UTS and (c) El % pertaining to high temperatures at various strain rates

3.2.1 Stress vs. Strain Curves in Different Orientations

Stress - strain curves have been plotted in different orientations i.e., in 45° and 90° from 700℃ - 900℃ temperature range in a gap of 50℃ and at different strain rates as presented in Figure 3.10 and Figure 3.11. It can be observed that as the temperature rises, flow stress reduces significantly from 700℃ - 850℃ and then it slows down. However, there is no significant variation in stress vs. strain curves for the different orientations.

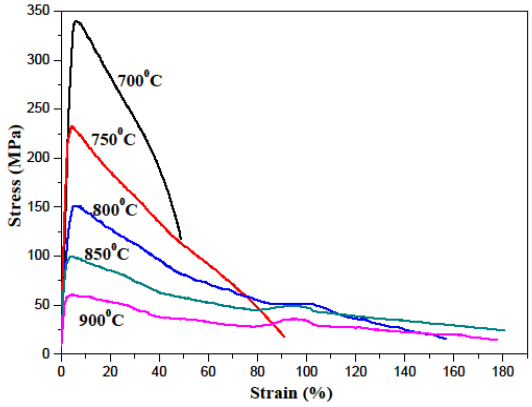

(a)

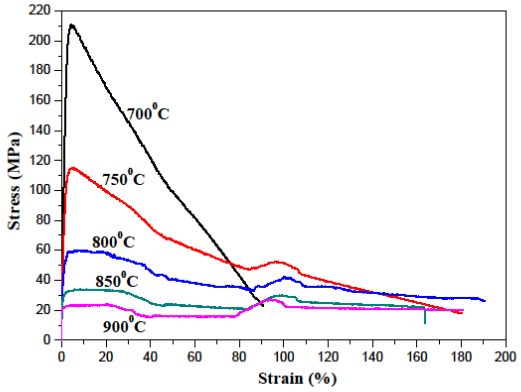

(b)

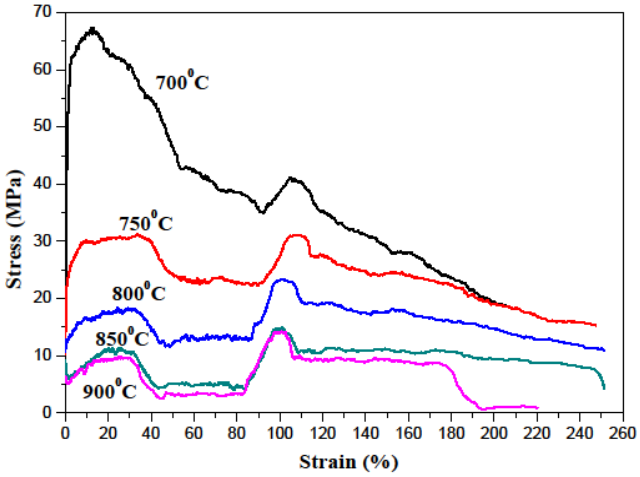

(c)

Figure 3.10 Stress vs. strain curves at (a) 10^{-2} s^{-1}, (b) 10^{-3} s^{-1} & (d) 10^{-4} s^{-1} and high temperatures along 45° orientation

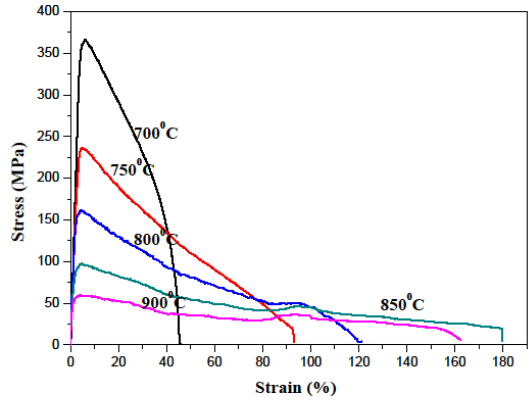

(a)

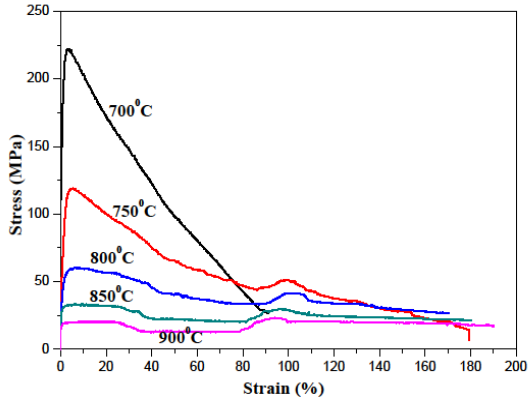

(b)

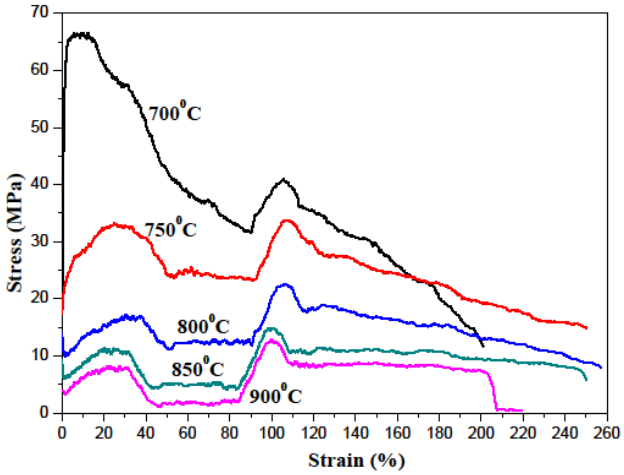

(c)

Figure 3.11 Stress vs. strain plots at (a) 10^{-2} s^{-1}, (b) 10^{-3} s^{-1} & (d) 10^{-4} s^{-1} and high temperatures along 90º orientation

3.2.2 Anisotropy Properties

Different anisotropy properties such as Lankford parameter (R), normal anisotropy (R_N) and planar anisotropy (ΔR) have been calculated for Ti-6Al-4V alloy as presented in Eqs (3.1) to (3.3) (Banabic 2010). Initially, the tensile specimen has been divided into equal number of divisions within the gauge length as presented in Figure 3.12. For the determination of R-value, the specimen has been deformed at a constant strain rate prior to its necking (≈ 10% strain). Finally, changes in dimensions of the deformed specimens have been measured using a stereo microscope and the average of five readings for each specimen has been considered.

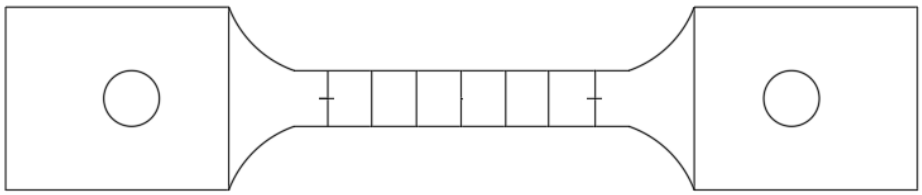

Figure 3.12 Tensile specimen for anisotropy study

Lankford parameter (R)

$$(R) = \frac{\varepsilon_{\text{width}}}{\varepsilon_{\text{length}}} \tag{3.1}$$

Normal anisotropy (R_N)

$$(R_N) = \frac{R_0 + 2R_{45} + R_{90}}{4} \tag{3.2}$$

Planar anisotropy (ΔR)

$$(\Delta R) = \frac{R_0 - 2R_{45} + R_{90}}{2} \tag{3.3}$$

where $\varepsilon_{\text{width}}$ denotes width strain, $\varepsilon_{\text{thickness}}$ denotes thickness strain and $\varepsilon_{\text{length}}$ denotes length strain, R_0, R_{45} & R_{90} represents anisotropy parameters along 0°, 45° & 90° orientations to rolling direction respectively. All these anisotropic parameters are presented in Table 3.2.

Table 3.2 Anisotropic parameters

Temp.	R_0	R_{45}	R_{90}	R_N	ΔR
RT	0.470	1.433	0.294	0.907	-1.051
700°C	0.310±0.3	0.322±0.2	0.315±0.2	0.317	-0.009
750°C	0.598±0.3	0.302±0.2	0.296±0.1	0.374	0.145
800°C	0.508±0.2	0.868±0.6	0.624±0.6	0.717	-0.302
850°C	0.239±0.09	0.419±0.3	0.405±0.3	0.370	-0.097
900°C	0.334±0.3	0.264±0.1	0.245±0.2	0.276	0.025

Table 3.3 presents the complete dataset of material properties (YS, UTS, El%) at different temperatures and strain rates.

Table 3.3 Material properties at high temperatures and different strain rates in different orientations

Orientations ➡		**(0º)**			**(45º)**			**(90º)**		
Temp.	**Matl. Prop.**	**10^{-2} s^{-1}**	**10^{-3} s^{-1}**	**10^{-4} s^{-1}**	**10^{-2} s^{-1}**	**10^{-3} s^{-1}**	**10^{-4} s^{-1}**	**10^{-2} s^{-1}**	**10^{-3} s^{-1}**	**10^{-4} s^{-1}**
700°C	**YS (MPa)**	332.84	189.46	87.68	328.08	201.24	56.56	334.98	201.93	63.88
	UTS (MPa)	349.19	200.31	89.28	339.96	210.70	68.17	366.67	221.06	67.77
	El (%)	58.12	78.34	182.03	48.43	90.66	205.25	46.24	90.22	200.85
750°C	**YS**	227.57	105.89	33.96	224.61	110.05	18.69	224.25	114.66	17.74
	UTS	240.75	108.79	39.23	232.35	113.27	31.19	235.97	119.05	32.44
	El	75.05	130.22	252.26	90.20	180.41	247.25	93.09	179.61	250.23
800°C	**YS**	160.25	64.74	18.53	147.93	48.90	12.00	151.66	48.55	12.26
	UTS	164.20	66.35	23.62	151.61	60.18	18.47	161.59	60.38	15.75
	El	150.17	178.30	257.19	158.15	190.23	251.25	121.20	170.47	257.26
850°C	**YS**	98.97	30.23	9.16	89.40	25.19	8.57	89.93	25.79	8.39
	UTS	99.37	32.92	15.17	100.00	34.05	10.02	97.30	33.57	10.56
	El	175.15	172.39	256.07	180.07	163.53	252.31	180.10	180.43	250.25
900°C	**YS**	67.27	20.25	2.85	57.73	23.29	6.33	54.83	19.85	4.48
	UTS	70.85	20.98	8.20	60.74	24.10	8.30	59.65	20.48	7.71
	El	188.05	180.22	220.25	178.75	180.85	220.09	160.23	190.28	219.24

Also, flow softening index (γ) has been calculated in all the three orientations from 750°C - 900°C and at 10^{-4} s^{-1}, as it is an essential parameter to quantify at high temperatures and is given by Eq. 3.4 (Semiatin and Bieler 2001),

$$\gamma = \frac{\sigma_{UTS} - \sigma_{\varepsilon}}{\sigma_{UTS}} \tag{3.4}$$

where σ_{UTS} indicate ultimate tensile stress (MPa) and σ_{ε} indicate stress (MPa) at a particular strain ($\varepsilon = 0.4$) in all the three orientations.

The obtained values of flow softening index are shown in Table 3.4. These values show an increasing trend of flow softening index from 750℃ - 900℃. The highest value obtained is along 0º orientation followed by 90º and 45º orientations. The percentage increase in flow softening index along 0º, 45º and 90º orientations from 750℃ - 900℃ were 504.31%, 1065.85% and 936.66% respectively.

Table 3.4 Flow softening index at 10^{-4} s^{-1} and high temperatures in different orientations

	(0º)			**(45º)**			**(90º)**		
	10^{-4} s^{-1}			**10^{-4} s^{-1}**			**10^{-4} s^{-1}**		
Temp.	σ_{UTS}	σ_{ε}	γ	σ_{UTS}	σ_{ε}	γ	σ_{UTS}	σ_{ε}	γ
750℃	39.23	34.65	0.116	31.19	29.89	0.041	32.44	30.48	0.060
800℃	23.62	16.18	0.314	18.47	14.24	0.229	15.75	14.62	0.071
850℃	15.17	9.26	0.389	10.02	6.01	0.400	10.56	4.88	0.537
900℃	8.2	2.45	0.701	8.30	4.33	0.478	7.71	2.91	0.622

Finally, the material properties obtained in different orientations from the stress vs. strain curves at 10^{-4} s^{-1} are drawn such as YS vs. temperature and UTS vs. temperature and are presented in Figure 3.13. It can be observed that variation in strength is highest along 0° orientation and almost similar in 45° and 90º orientations. Percentage decrease in YS along 0°, 45° and 90º orientations is 96.74%, 88.80% and 92.98% respectively, whereas the percentage decrease in UTS along 0°, 45° and 90º orientations is 90.81%, 87.82% and 88.62%.

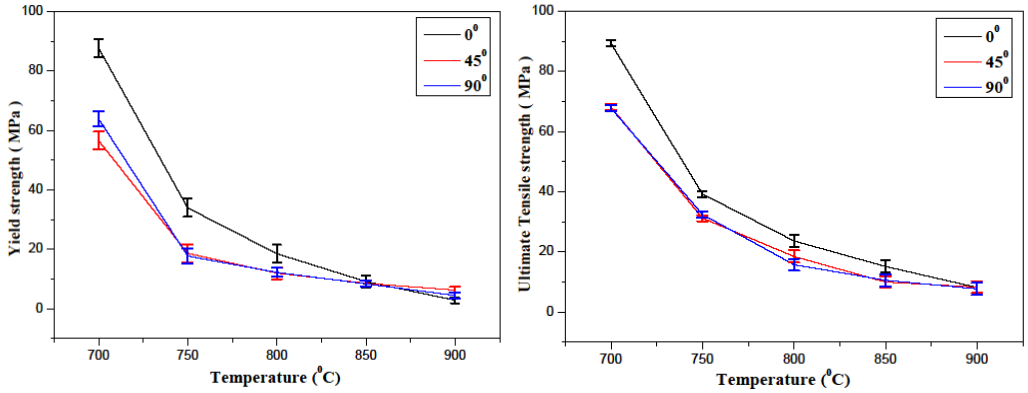

Figure 3.13 Difference of mechanical properties (a) YS & (b) UTS at 10^{-4} s^{-1} and high temperatures in different orientations

Furthermore, the deformed specimens were characterized using OM, SEM as well as XRD techniques, to understand the metallurgical aspects responsible for the flow softening and superplasticity.

3.3. Metallography Characterization of Ti-6Al-4V Alloy

3.3.1 Flow Softening Characterization

To understand the deformation behaviour, tensile test samples have been characterized using OM and SEM at high temperatures as well as various strain rates. Based on this, the grain and void sizes have been quantified from optical and SEM micrographs at 800°C as illustrated in Figure 3.14, it indicates void sizes of 0.58 µm at 10^{-3} s^{-1} and 0.83 µm at 10^{-4} s^{-1}.

Whereas, at 750°C micrographs as shown in Figure 3.14 (c) - (e) indicates 0.41 µm at 10^{-2} s^{-1}, 0.36 µm at 10^{-3} s^{-1} and 0.48 µm at 10^{-4} s^{-1} respectively. This represents there is a reduction in the void sizes as there is a rise in strain rate apart from 10^{-2} s^{-1} at 750°C. Thus, at a constant temperature and with rise in strain rate, it has been observed that the quantity of voids increases, whereas its size reduces.

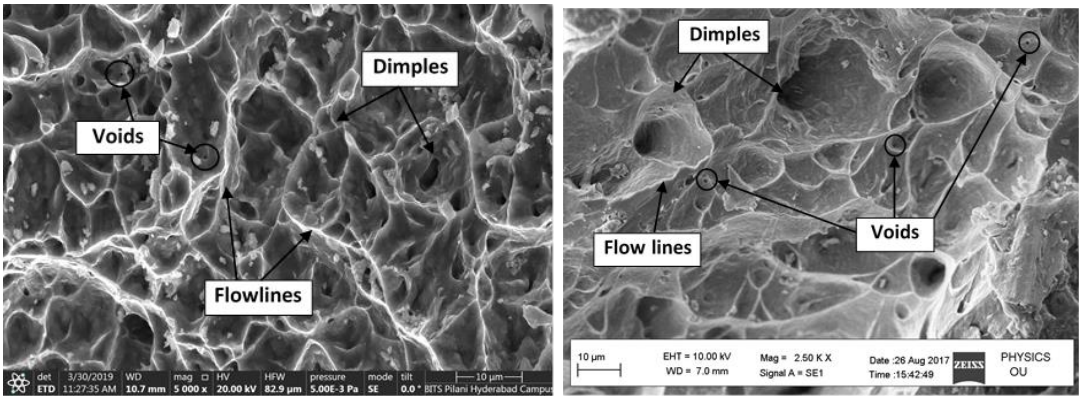

(a) (b)

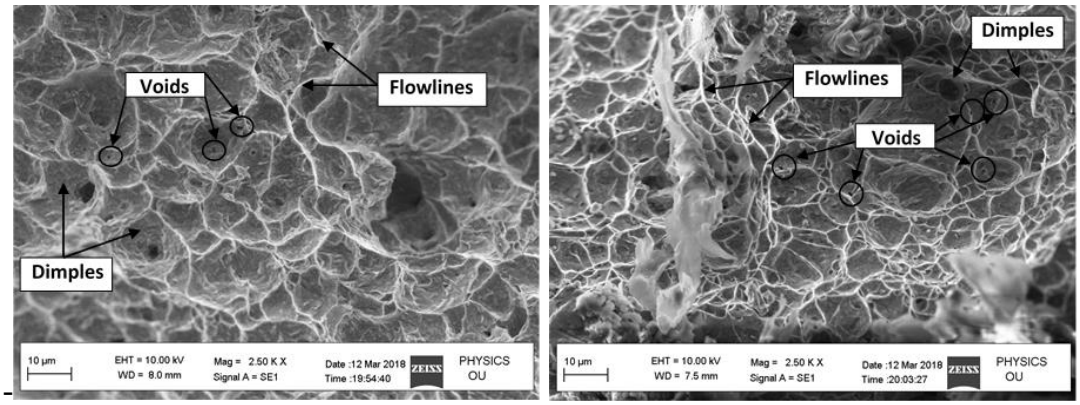

(c) (d)

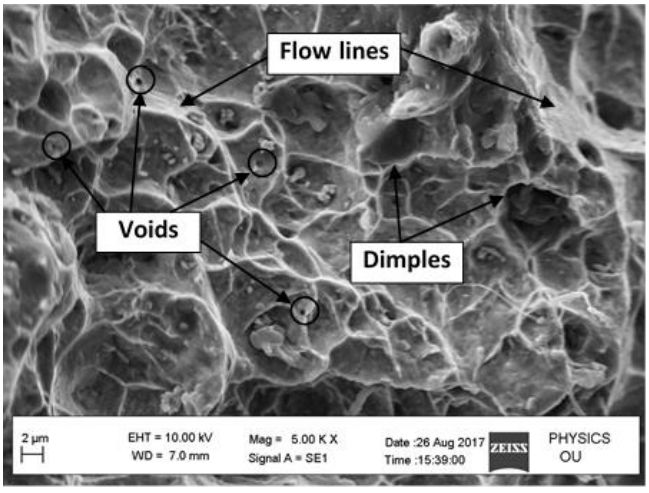

(e)

Figure 3.14 (a) Scanning Electron micrographs of ruptured specimens at 800℃ (a) 10^{-3} & (b) 10^{-4} s^{-1} and at 750℃ (c) 10^{-2}, (d) 10^{-3} & (e) 10^{-4} s^{-1} respectively

Simultaneously, optical micrographs have been obtained at 800℃ as presented in Figure 3.15 (a) - (b), it indicates α-Ti = 7.86 µm at 10^{-3} s^{-1} and α-Ti = 11.2 µm at 10^{-4} s^{-1}, whereas the grain sizes at 750℃ and different strain rates are displayed in Table 3.5 and related microstructures are illustrated in Figure 3.15 (c) - (e). Interestingly, at 10^{-3} s^{-1} and 750℃, the grain and void sizes were lesser in comparison with 10^{-4} s^{-1} as well as 10^{-2} s^{-1}. This could be because of the refinement in grains enabling the sliding of grains as it reduces effective stress. Also, cavitation is necessary to accommodate grain sliding at respective superplastic settings.

Table 3.5 Grain size at 750℃ and different strain rates

Strain rate (s^{-1})	Alpha (µm)
10^{-2}	6.50
10^{-3}	4.90
10^{-4}	9.90

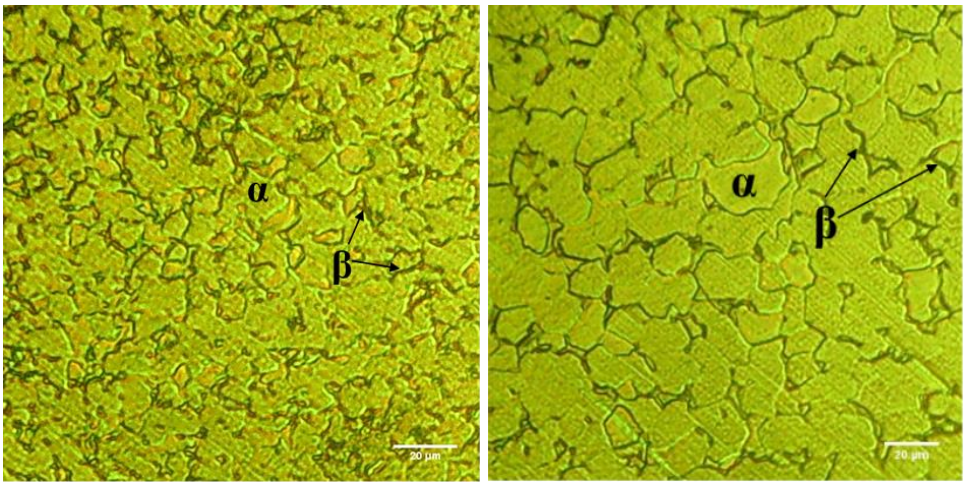

(a) (b)

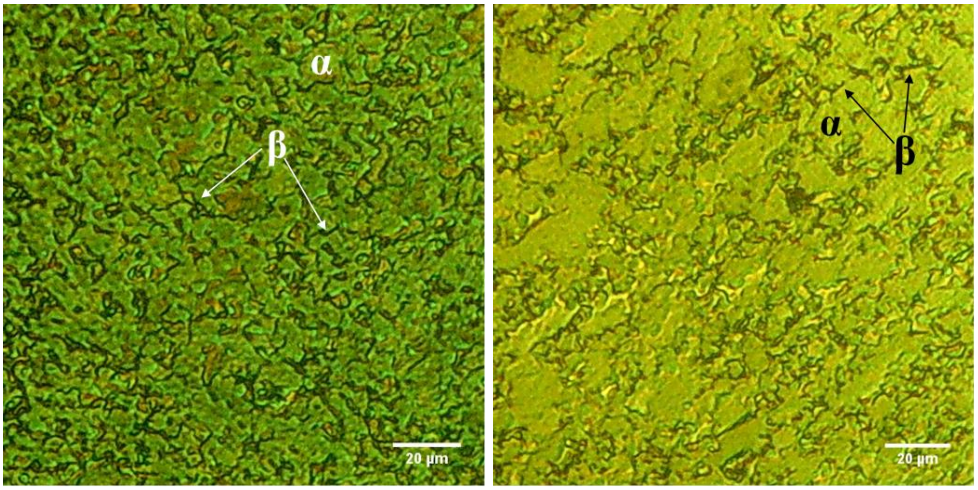

(c) (d)

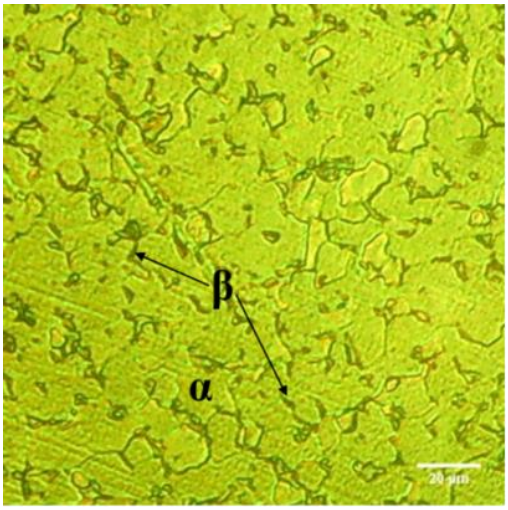

(e)

Figure 3.15 Optical micrographs of ruptured specimens at 800℃ (a) 10^{-3} s^{-1} & (b) 10^{-4} s^{-1} and at 750℃ (b) 10^{-2} s^{-1}, (c) 10^{-3} s^{-1} & (d) 10^{-4} s^{-1} respectively

Therefore, refinement of grain because of dynamic recrystallization might be the reason for occurrence of flow softening. Thus, at the lowest strain rate, superplastic behaviour improves grain size because of long exposures to high temperatures and it could be the reason for flow softening. Whereas, at high strain rates because of DRX the grain size as well as void size are lesser and it could be the reason for flow softening, similarly reported by Alabort et el. (2015).

3.3.2 Superplasticity Characterization

Metallography study has been performed on the ruptured samples at 750°C & 800°C at 10^{-4} s^{-1}, to analyze the superplastic deformation viz. El > 200%, distinction with the ruptured samples at Room temperature (RT). The optical images of ruptured samples at 10^{-4} s^{-1} and RT, 750°C and 800°C are shown in Figure 3.16. The existence of dual phase alpha (α-Ti) and beta (β-Ti) was observed with different size as well as distribution, similarly stated by Vanderhasten et al. (2007). Microstructure image of RT consists of equiaxed alpha phase grains with equal sharing of fine intergranular beta phase grains, similarly observed by Xiao, et al. (2012).

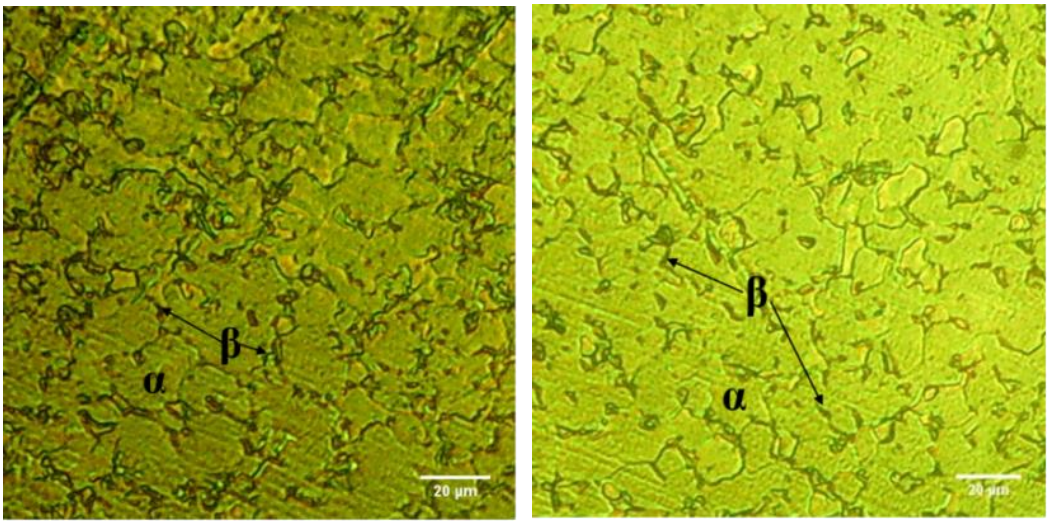

(a) (b)

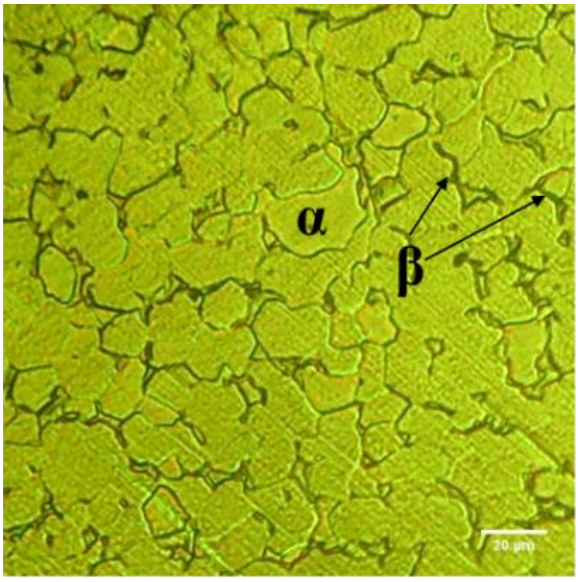

(c)

Figure 3.16 Optical images of ruptured specimens at 10^{-4} s^{-1} and different temperatures (a) RT, (b) 750°C and (c) 800°C

Volume fractions along with average grain sizes of beta phase are showed in Figure 3.17.

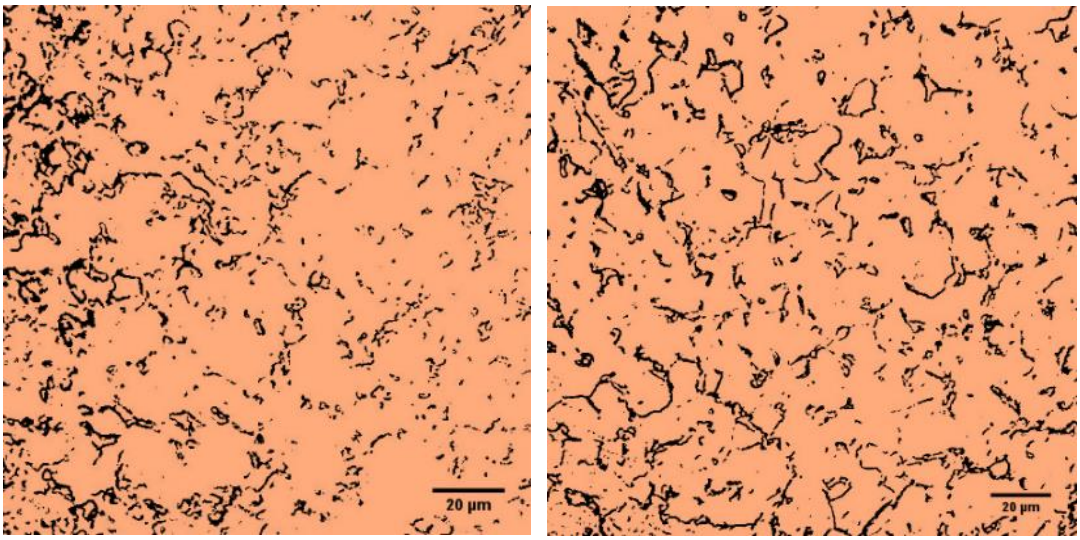

(a) (b)

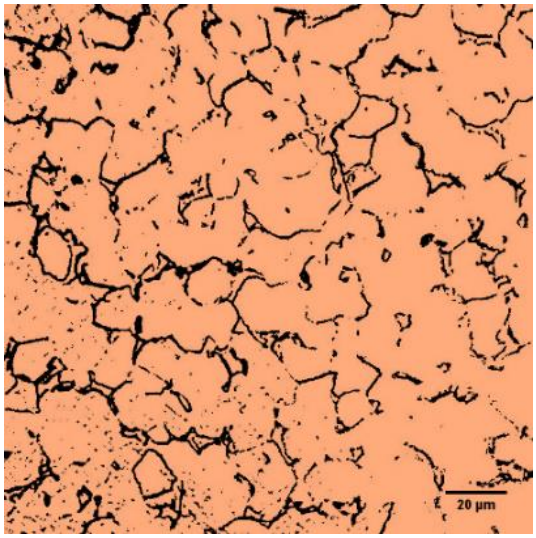

(c)

Figure 3.17 Volume fractions and Avg. grain size of beta phase for ruptured specimens at 10^{-4} s^{-1} and different temperatures at (a) RT, (b) 750℃ & (c) 800℃

The quantitative analysis of both the grain sizes are presented in Figure 3.18 and Figure 3.19. It shows an increasing tendency with the temperature. The average grain sizes of alpha and beta phase were calculated and obtained as 9.4 µm as well as 1.2 µm at RT, whereas at high temperatures i.e., at 750℃ and 800℃, they have been found to be as 9.9 & 1.4 µm and 11.2 & 1.5 µm.

The coarsening of beta phase is because of agglomeration due to high temperatures. As a result, the growth in grain size along with the rise in temperature could be recognized as the improvement in ductility as well as reduction in the strength that is apparent from Figure 3.7 (d). Similar phenomena about the existence of beta phase, its grain size sharing along with area fraction that has a major effect on the mechanical properties of material has been reported by Kim et al. (1999).

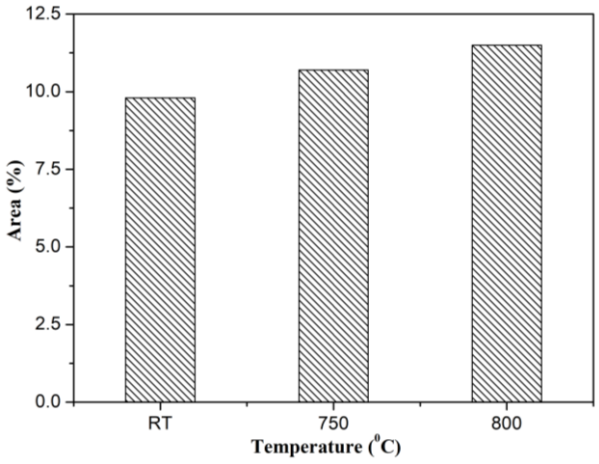

(a)

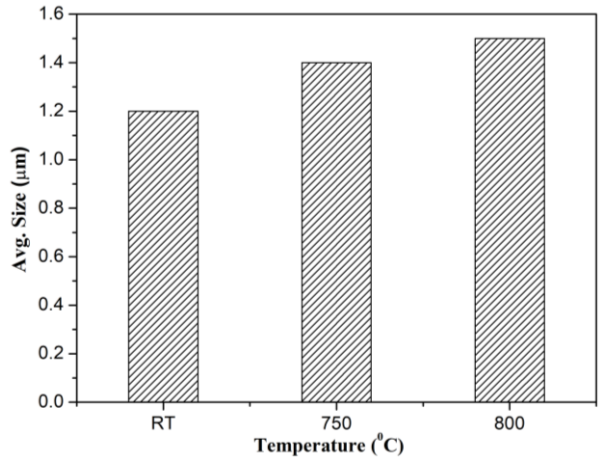

(b)

Figure 3.18 Quantitative study of beta phase for ruptured specimens (a) percentage area fraction & (b) Average size (μm) pertaining RT, 750℃ & 800℃ at 10^{-4} s^{-1}

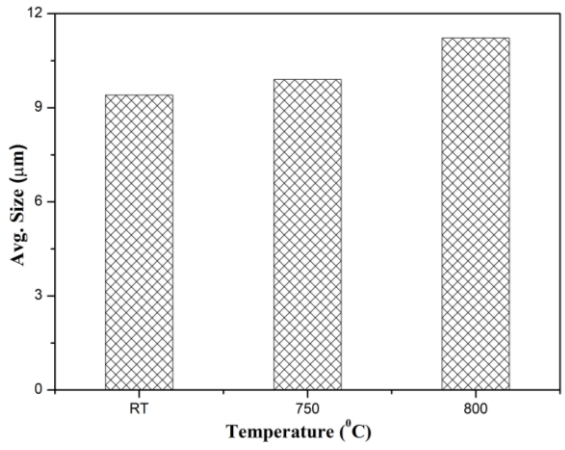

Figure 3.19 Quantitative study of alpha phase for ruptured specimens - Average size (μm) pertaining to RT, 750℃ & 800℃ at 10^{-4} s^{-1}

The growth in grain size at higher temperatures may be because of thermal activation of interface energy along with higher driving force helping in grain development. Also, heat-induced phase change for beta phase makes it challenging at temperatures lower than (T_β) beta transus temperature (980℃ - 1040℃) as described by Tamirisakandala et al. (2005), Roy and Suwas (2013), Roy et al. (2014). Thus, with increase of temperature, agglomeration of beta phase was observed as coarse grain size along with stress induced phase change. It offers additional activation energy for the phase change from alpha to beta that brings about in comparatively extra volume of the transformed beta phase and can be distinguished from Figure 3.18 (a), which clearly shows growth from 9.8% to 11.5%, similarly reported in the investigations performed by Tuoyang et al. (2014).

Therefore, improvement in the ductility with the rise of temperature could be because of the GBS and the change of alpha phase to beta phase at high temperatures helps as an additional stress accommodation mechanism, leading to a greater El%. Though, there has been a consistent reduction in the mechanical properties such as YS and UTS and it is evident from Figure 3.9.

To confirm the superplastic behaviour (El %), Scanning Electron Microscope (SEM) study has been performed on the ruptured samples. SEM micrographs of ruptured specimens at 10^{-4} s^{-1} and at different temperatures i.e., (a) RT, (b) 750℃ and (c) 800℃ are shown in Figure 3.20, representing ductile rupture with improving ductility. Increase in the ductility is accounted by a rise in the quantity of dimples along with flow lines. Also, from these Figures, it has been noticed that dimple size pertaining to high temperatures is greater, when compared to the dimple size

pertaining at RT. The existence of bigger size dimples along with flow lines and the voids specify presence of superplastic behaviour at related temperatures.

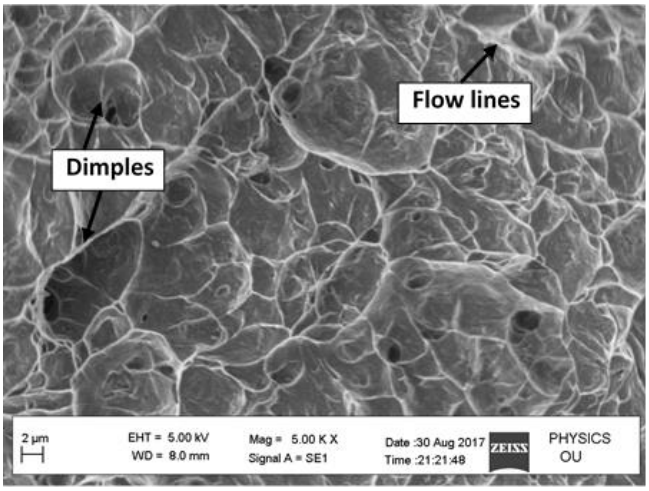

(a)

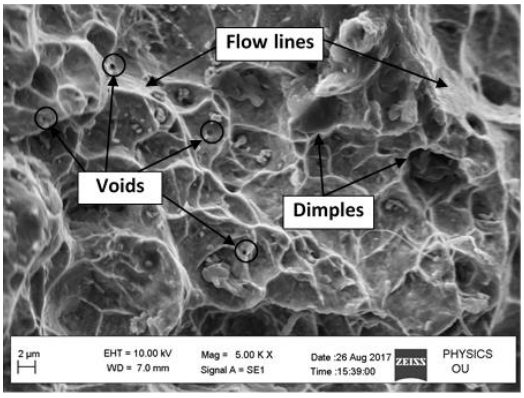

(b)

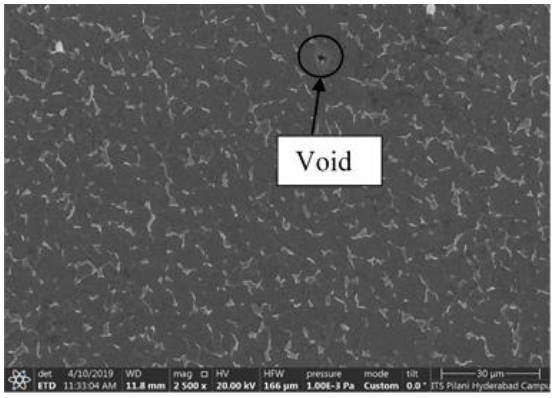

(c)

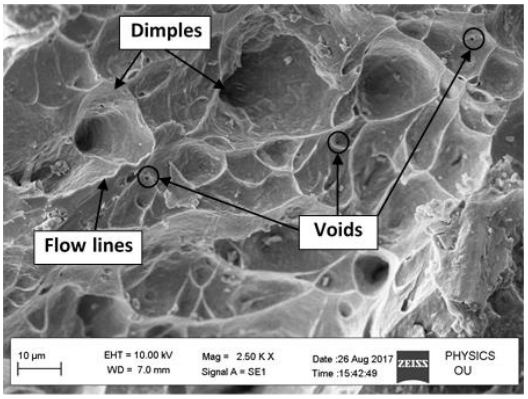

(d)

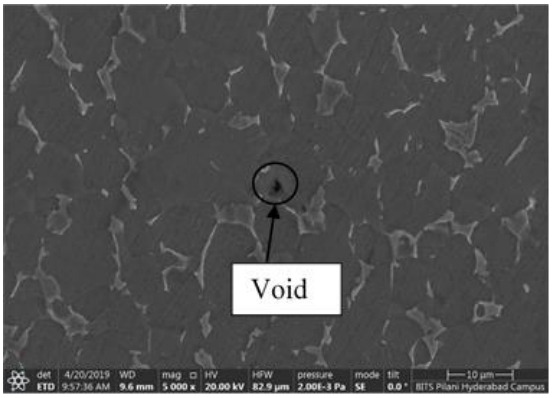

(e)

Figure 3.20 SEM images of ruptured specimens at 10^{-4} s^{-1} and different temperatures (a) RT, (b and c) 750°C & (d and e) 800°C

3.3.3 X-ray Diffraction

Figure 3.21 represents the XRD of Ti-6Al-4V alloy tensile deformed at various temperatures as well as at 10^{-4} s^{-1}. Images illustrate the peak occurrence remains nearly similar in all the three circumstances, though the diffraction pattern presents slight variation. All diffraction patterns display mainly HCP diffraction peaks for planes (002), (101) as well as (102).

On the other hand, as the temperature increases, the diffraction curve seems to vary. This specifies that some variations may be arising inside the lattice of the system over short-range diffusions, however, phase transformations were not obvious over diffraction curves. While the plane (004) vanishes at 750℃ as well as at 800℃, it may be because of rise in the temperature.

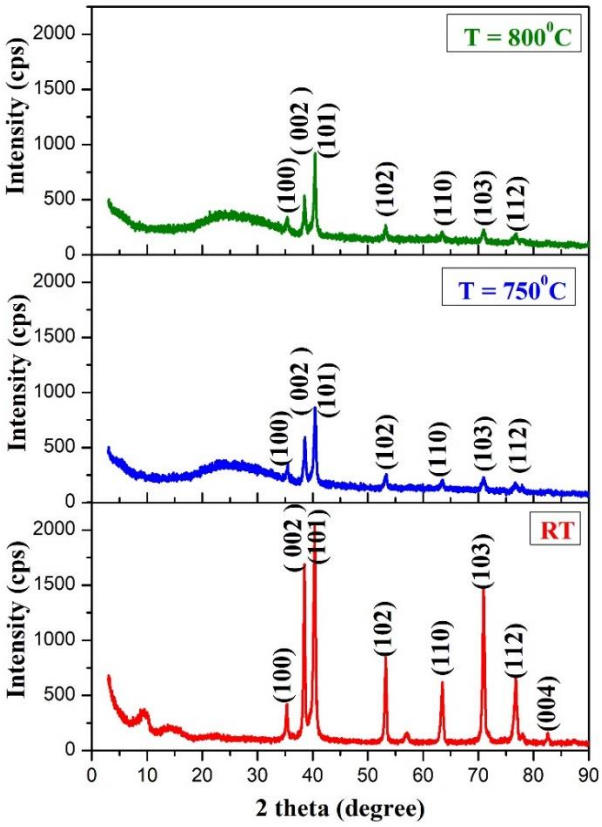

Figure 3.21 XRD of Ti-6Al-4V alloy deformed at 10^{-4} s^{-1} and different temperatures

3.4. Summary

This chapter discusses the experimental investigation and characterization of Ti-6Al-4V alloy at high temperatures and different strain rates. From stress vs. strain curves, it was observed that the superplasticity range of Ti-6Al-4V alloy occurs from 750℃ - 900℃ at 10^{-4} s^{-1}, as the complete elongation till rupture is greater than 200%, whereas YS and UTS reduces by 80% - 97% and the ductility improves by 41% - 224% and calculated anisotropic properties showed no variation. Furthermore, microstructure analysis revealed mean grain sizes of alpha and beta phase increases when compared to RT, whereas SEM analysis confirmed increase in ductility and XRD analysis revealed peak positions of the specimens remain almost the same.

Based on these tensile test studies, constitutive models and processing maps for Ti-6Al-4V alloy have been developed and presented in the next chapter.

CHAPTER 4 : CONSTITUTIVE MODEL AND PROCESSING MAPS FOR TI-6AL-4V ALLOY

For understanding the hot deformation behaviour of Ti-6Al-4V alloy, it is important to first understand its flow stress behaviour using the tensile test data at various strain rates as well as temperatures. The constitutive model helps to understand the flow stress behaviour with accurate prediction capabilities. Processing maps present a graphical picture of the stable and instable deformation regime. Development of a suitable constitutive model as well as processing maps has been presented in this chapter. Both of these require the true stress – true strain data at different temperatures as well as strain rates, which are illustrated in Figure 4.1.

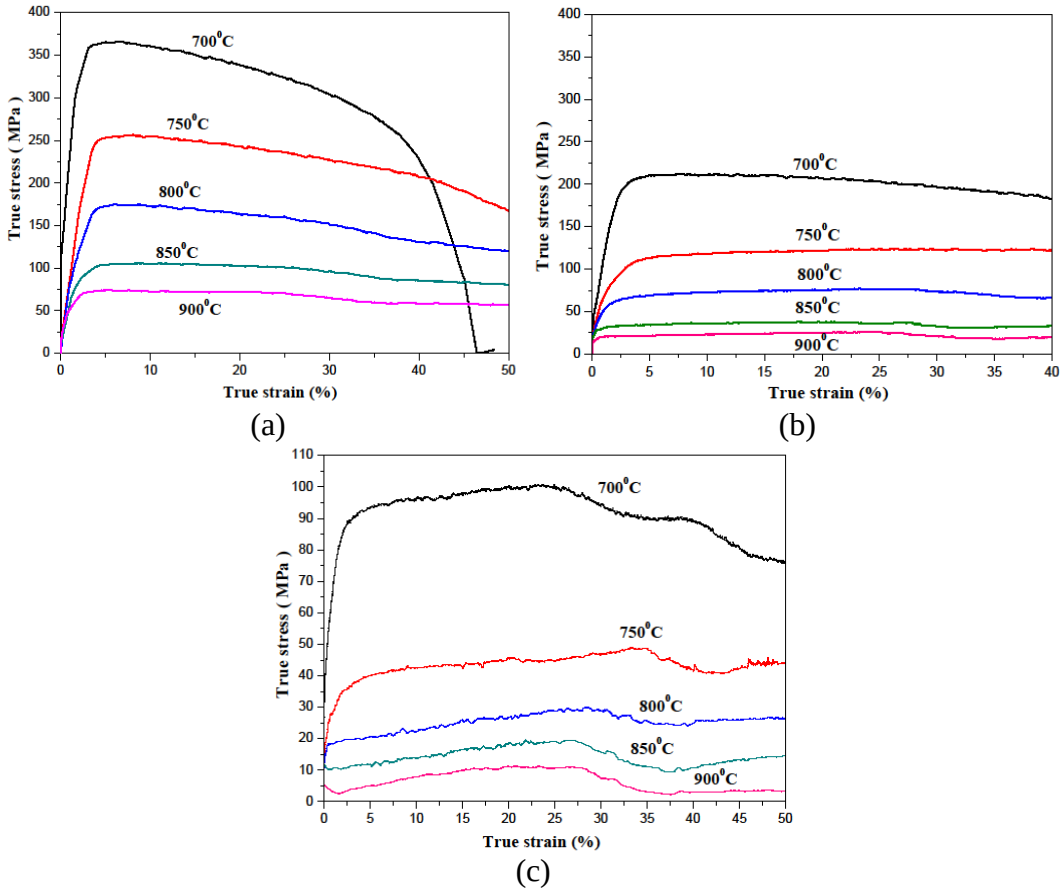

Figure 4.1 True stress - true strain curves along 0° orientation at high temperatures & various strain rates (a) 10^{-2} s^{-1}, (b) 10^{-3} s^{-1} & (c) 10^{-4} s^{-1}

4.1.Development of Constitutive Model

Initially, Johnson Cook (JC) as well as modified Zerilli Armstrong (m-ZA) models have been tried for representing the flow stress behaviour of Ti-6Al-4V alloy at high temperatures. The JC model used by Gupta et al. (2013) as well as Chen et al. (2015) expressed the flow stress behaviour mathematically as in Eq. 4.1,

$$\sigma = (\mathrm{A} + \mathrm{B}\varepsilon^{n})\,(1 + \mathrm{C}ln\dot{\varepsilon})\,(1 - T^{*m}) \quad (4.1)$$

where σ - von Mises flow stress, A - stress (yield) at ref. temperature as well as ref. strain rate, B – Coeff. of strain hardening, n - exponent (strain hardening), ε - plastic strain, C – Coeff. of strain rate hardening, $\dot{\varepsilon}^{*} = {\dot{\varepsilon}}/{\dot{\varepsilon}_0}$, where $\dot{\varepsilon}$ - strain rate, $\dot{\varepsilon}_0$ - reference strain rate, T^{*m} - homologous temperature and m - exponent (thermal softening).

Homologous temperature can be expressed as shown in Eq. 4.2,

$$T^{*} = \frac{T - T_{\mathrm{ref}}}{T_m - T_{\mathrm{ref}}} \quad (4.2)$$

where T - temperature (absolute), T_m - temperature (melting), T_{ref} - temperature (reference) such that $T \geq T_{\mathrm{ref}}$ always.

The following steps have been used to obtain values of the required parameters:

Step 1: Ref. strain rate and ref. temperature

In this step, second term along with third term in Eq. 4.1 becomes equal to unity such that,

$$\sigma = (\mathrm{A} + \mathrm{B}\varepsilon^{n}) \quad (4.3)$$

From this, B and n values are obtained.

Step 2: Fixed strain and ref. temperature

By using this step, Eq. 4.1 reduces to Eq. 4.4,

$$\sigma = (\mathrm{A} + \mathrm{B}\varepsilon^{n})\,(1 + \mathrm{C}ln\dot{\varepsilon}) \quad (4.4)$$

From this, C value is obtained.

Step 3: Fixed strain and ref. strain rate

With the help of this condition, Eq. 4.1 reduces to Eq. 4.5,

$$\sigma = (\mathrm{A} + \mathrm{B}\varepsilon^{n})\,(1 - T^{*m}) \quad (4.5)$$

From this condition, *m* value is obtained.

Similarly, modified-ZA model applied by Kotkunde et al. (2014) was used to predict flow stress behaviour and represented mathematically as in Eq. 4.6,

$$\sigma = (\mathrm{C}_1 + \mathrm{C}_2\varepsilon^{n})\, exp\{-(\mathrm{C}_3 + \mathrm{C}_4\varepsilon)T^{*} + (\mathrm{C}_5 + \mathrm{C}_6T^{*})\ln\dot{\varepsilon}^{*}\} \quad (4.6)$$

where C_1 to C_6 along with *n* represents material constants.

The following conditions have been used to obtain required constants:

Step 1: Ref. strain rate

By using this condition, Eq. 4.6 reduces to Eq. 4.7,

$$\sigma = (\mathrm{C}_1 + \mathrm{C}_2\varepsilon^{n})\, exp\,\{-(\mathrm{C}_3 + \mathrm{C}_4\varepsilon)T^{*}\} \quad (4.7)$$

From this condition C_1, C_2, C_3, C_4 and *n* values are obtained.

Step 2: Taking into consideration the coupled effects

In this condition, applying log on both the sides of Eq. 4.6, we finally get Eq. 4.8,

$$ln\,\sigma = ln\,(\mathrm{C}_1 + \mathrm{C}_2\varepsilon^{n}) - (\mathrm{C}_3 + \mathrm{C}_4\varepsilon)T^{*} + (\mathrm{C}_5 + \mathrm{C}_6T^{*})\ln\dot{\varepsilon}^{*} \quad (4.8)$$

From this condition, C_5 and C_6 values are obtained.

Finally, all the required values are obtained and optimized to reduce error, then statistical measures are used to quantify the performance of the constitutive model.

However, both these models were not able to properly represent the hot tensile behaviour of Ti-6Al-4V alloy at different strain rates. This is due to the reason that after attaining UTS flow stress values decrease and after reaching certain points the difference between the stress values and yield stress becomes negative, while this becomes incompatible in the JC and m-ZA equations. In other words, these two models were found ineffective in capturing the flow softening behaviour in Ti-6Al-4V alloy from 700℃ - 900℃. Therefore, the modified-Arr model has been considered for representing the hot flow stress behaviour of Ti-6Al-4V alloy.

In general, flow stress data is applied in the development of constitutive models to visualize the flow stress at high temperatures along with various strain rates, as used by Lin and Chen (2011) - Porntadawit et al. (2014). In this work, a modified-Arr model has been formulated, to study the hot flow stress of Ti-6Al-4V alloy.

The Arrhenius equation has been used by most of the researchers efficiently such as Gupta et al. (2013), Chen et al. (2015) to calculate the flow performance at high temperatures along with various strain rates. It takes into consideration, the flow softening occurred at a number of stress levels. For this, Zener - Holloman (*Z*) parameter considers temperature working range along with strain rate. Arithmetically, it is represented by an exponential Eq. (4.9) given by Sellars & McTegart (1966), Zener & Hollomon (1944),

$$Z = \dot{\varepsilon} * exp\left(\frac{Q}{RT}\right) \tag{4.9}$$

where, *Q* stands for activation energy (KJ/mol), *R* denotes constant (universal gas) (8.314 $Jmol^{-1}K^{-1}$), *T* represents temperature (Kelvin) and $\dot{\varepsilon}$ stands for strain rate (s^{-1}) also presented in Eq. (4.10),

$$\dot{\varepsilon} = AF(\sigma)\, exp\left(-\frac{Q}{RT}\right) \tag{4.10}$$

where,

$$F(\sigma) = \begin{cases} \sigma^n \; for \; \alpha\sigma \; less \; than \; 0.8 \\ exp(\beta\sigma) \; for \; \alpha\sigma \; greater \; than \; 1.2 \\ [sinh(\alpha\sigma)]^n \; for \; all \; \sigma \end{cases} \tag{4.11}$$

By presenting hyperbolic sine function in the Eq. (4.10), it has been modified,

$$\dot{\varepsilon} = A\,[sinh(\alpha\sigma)]^{\,n} exp\left(-\frac{Q}{RT}\right) \tag{4.12}$$

Now, relating Eq. (4.9) and (4.12), we get

$$\sigma = \frac{1}{\alpha}\, ln \left\{ \left(\frac{Z}{A}\right)^{1/n} + \left[\left(\frac{Z}{A}\right)^{2/n} + 1\right]^{1/2} \right\} \tag{4.13}$$

Eq. (4.13) does not include strain. Thus, for including strain, Xiao and Guo (2011) introduced supplementary terms as shown in Eq. (4.14) and it suitably analyzes the impact of temperature range, strain along with strain rate.

$$\sigma = \frac{\beta_0 \varepsilon^{\beta_1 exp(-\beta_2 \varepsilon)}}{\alpha}\, ln \left\{ \left(\frac{Z}{A}\right)^{1/n} + \left[\left(\frac{Z}{A}\right)^{2/n} + 1\right]^{1/2} \right\} \tag{4.14}$$

Eq. (4.14) is called the m-Arr model and material coefficients *A*, α & *n* have been calculated depending on the experimentally acquired tensile test data from high temperatures and various strain rates. Considering true strain spectrum from 0.05 - 0.4 with a gap of 0.05, a plot involving *ln* [*sin h* ($\alpha\sigma$)] vs. *ln* ($\dot{\varepsilon}$) gives n^{-1} as slope and *n* value is determined. In the same way, a plot of *ln* [*sin h* ($\alpha\sigma$)] vs. 1/*T* gives (*Q*/*nR*) as the slope. Finally, the average value of the slopes have been considered to estimate

activation energy (Q) that is found to be 164 KJmol^{-1}. The obtained material coefficients of m-Arr model are shown in Table 4.1.

Table 4.1 Material coefficients obtained for m-Arr model

Constants	α **(MP/a)**	n	A **(1/s)**
Value	0.003	2.750	2.16e5

β_0, β_1 as well as β_2 are determined from Eq. (4.15),

$$\beta = A * ln(Z) + B \tag{4.15}$$

With the help of a non-linear regression function (nlinfit) in the MATLAB software, β_0, β_1 along with β_2 material coefficients have been calculated and presented by Eqs 4.16 to 4.18,

$$\beta_0 = 0.02339\, ln\,(Z) - 0.2541 \tag{4.16}$$

$$\beta_1 = -0.0618\, ln\,(Z) + 1.3730 \tag{4.17}$$

$$\beta_2 = 0.0240\, ln\,(Z) + 0.9543 \tag{4.18}$$

After determining all the required coefficients, the Z value has been calculated depending on the tests conducted at high temperatures as well as different strain rates. Once Z value is obtained, flow stress behaviour can be estimated with the help of Eq. (4.14). Finally, the Zener - Holloman (Z) parameter is stated as

$$Z = \dot{\varepsilon} * \exp\left(\frac{164}{8.314 * T}\right)$$

Figure 4.2 (a) - (c) shows comparison of experimental vs. predicted flow stress at high temperatures as well as various strain rates (a) 10^{-2} s^{-1}, (b) 10^{-3} s^{-1} as well as (c) 10^{-4} s^{-1}. The prediction capacity of the m-Arr model was assessed based on statistical procedures viz., correlation constant (*R*), avg. absolute error along with its standard deviation and these were obtained as 0.993, 11.34% and 14.27%.

Furthermore, from these figures, it can be perceived that calculation of flow stress using the m-Arr model appears to be in close agreement when compared to the experimental flow stress, mainly at 10^{-2} s^{-1} and 10^{-3} s^{-1}. On the other hand, the variation occurring at 10^{-4} s^{-1} might be because of the existence of superplasticity varying from 750°C - 900°C.

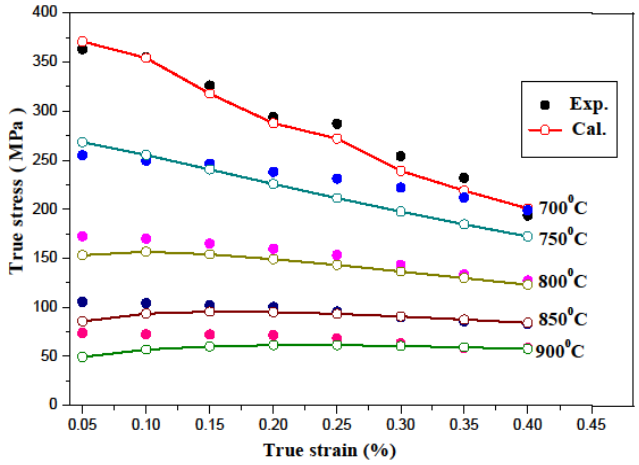

(a)

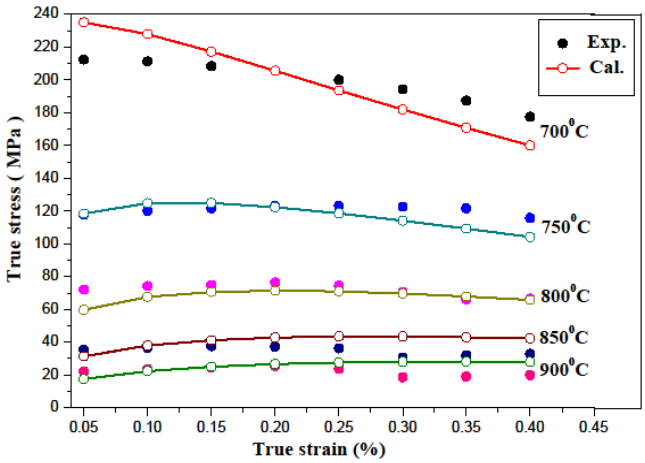

(b)

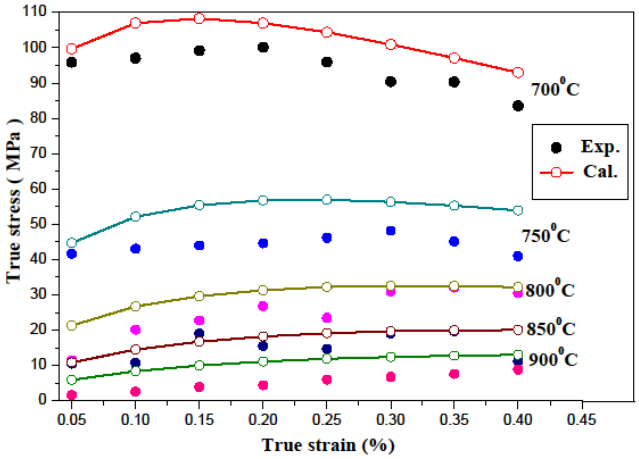

(c)

Figure 4.2 Comparison between experimental and predicted flow stress at high temperatures and various strain rates (a) 10^{-2} s^{-1}, (b) 10^{-3} s^{-1} & (c) 10^{-4} s^{-1}

Figure 4.3 presents the correlation constant (*R*) among experimental flow stress vs. predicted flow stress. Higher degree of proximity for *R* value as well as least error expresses the accuracy of the m-Arr model in calculating the flow stress.

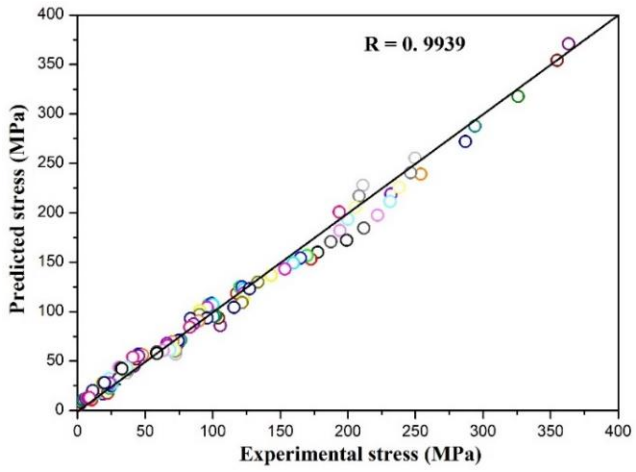

Figure 4.3 Comparison between experimental and predicted stress behaviour

Furthermore, to confirm and get the optimal settings of superplasticity, processing maps have been developed using flow stress data and have been presented in the next section.

4.2. Development of Processing Maps

In the development of processing maps, *m* plays a main role in defining the superplastic deformation behaviour. Based on *m* values, efficiency and instability maps are developed and then superimposed to develop processing maps.

4.2.1 Determination of Strain Rate Sensitivity

The obtained true stress - true strain data was applied to calculate *m* and it is an essential parameter in describing superplastic deformation. The superplastic deformation is amenable to strain rate and it is specified at respective stress (σ) and strain rate ($\dot{\varepsilon}$), as given by Dieter (2013), Wang et al. (2018) - Tang et al. (2015) and shown in Eq. (4.19),

$$\sigma = K\dot{\varepsilon}^{m} \tag{4.19}$$

where, *K* stands for material coefficient and *m* represents strain-rate sensitivity.
By applying log function on both the sides of Eq. (4.19), we get

$$m = \left(\frac{\partial\, ln\, \sigma}{\partial\, ln\, \dot{\varepsilon}}\right)_{\varepsilon,T} \tag{4.20}$$

Finally, *m* value has been calculated by Eq. 4.20. Figure 4.4 represents log - log curves of true stress vs. strain rate at various strains i.e., (a) 0.1, (b) 0.2, (c) 0.3 as well as (d) 0.4, to determine *m* values at different points by utilizing a polynomial fit, similarly considered by Wang et al. (2016), Sun et al. (2018).

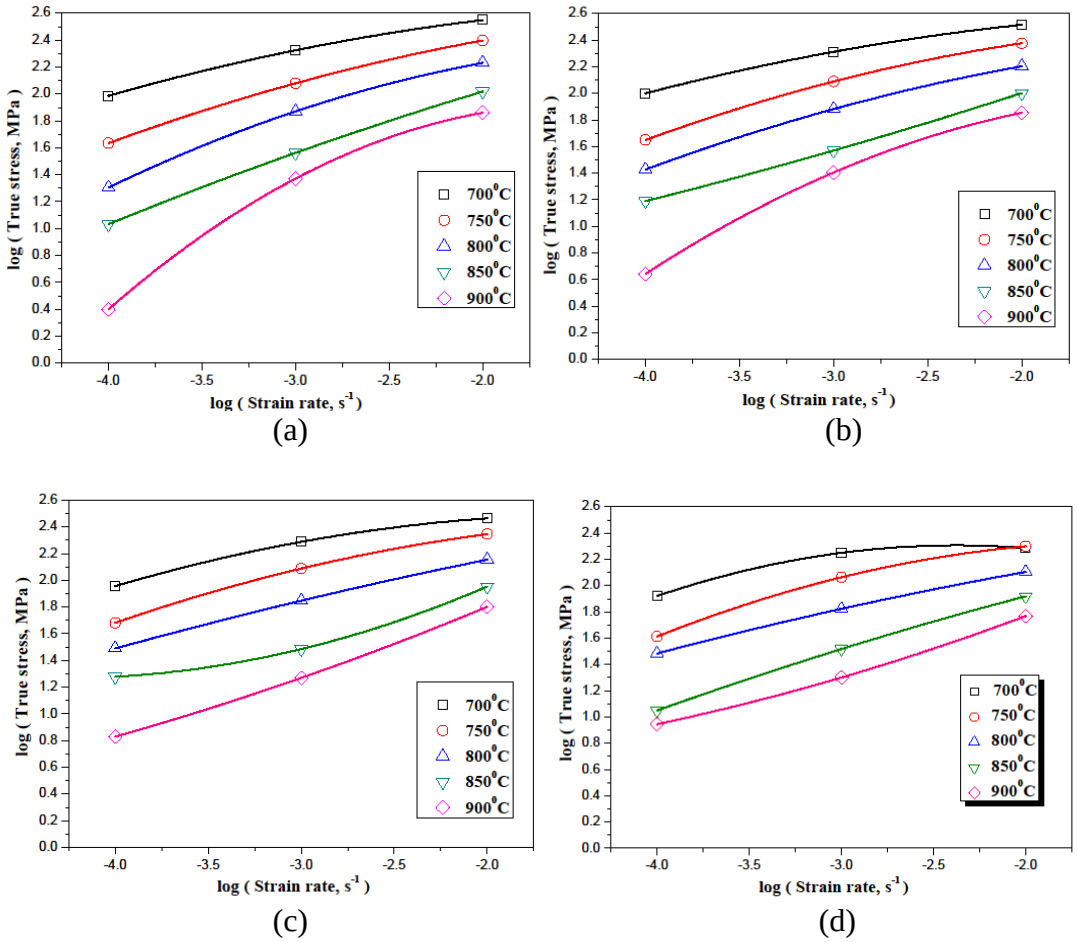

Figure 4.4 Log - log curves of true stress - strain rate at various strains (a) 0.1, (b) 0.2, (c) 0.3 & (d) 0.4

Figure 4.5 represents contour maps indicating *m* at various strain values i.e., (a) 0.1, (b) 0.2, (c) 0.3 along with (d) 0.4. From the presented Figures, it is perceived that maximum *m* value is achieved at the 0.1 strain as presented in Figure 4.5 (a) and the minimum *m* value is achieved at the 0.4 strain as presented in Figure 4.5 (d), i.e., *m* reduces with the rise in strain. Also, *m* rises from 0.1 - 0.3 strain consistently, viz. from temperature 700℃ - 900℃ and from 10^{-2} s^{-1} - 10^{-4} s^{-1} strain rate as shown in Figure 4.5 (a) - (c). Though at 0.4 strain, *m* value differs in a diverse way with respect to the working temperature as well as strain rate.

Generally, *m* in a range of (0.3 to 0.8) shows that the metal is experiencing superplastic behaviour, as reported by Giuliano (2011) and Tuoyang et al. (2014). It is perceived from Figure 4.5 that the *m* values obtained at higher strain rates along with lower temperatures is less than the above stated spectrum, confirming the absence of superplastic behaviour, i.e., at lower *m* values, the metal cannot stop thinning. Moreover, at lower strain rates along with higher temperatures, the *m* value fluctuates inside the mentioned spectrum, and therefore indicates superplasticity of Ti-6Al-4V alloy.

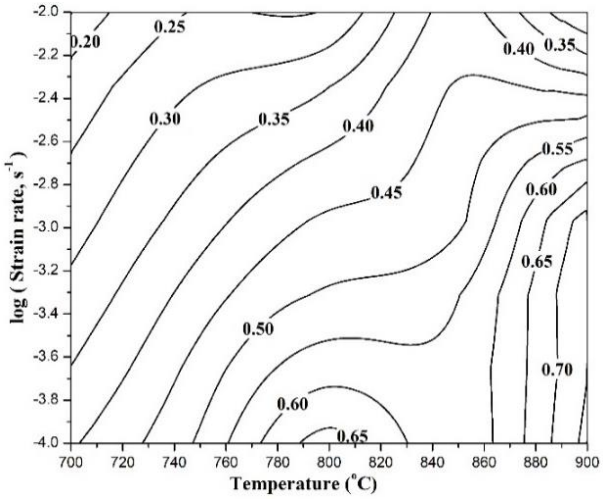

(a)

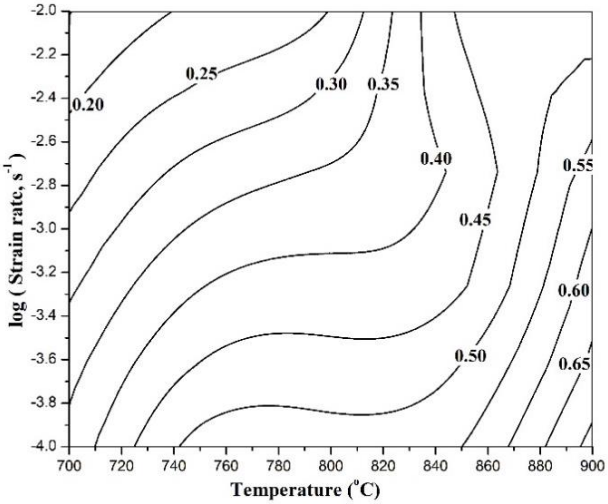

(b)

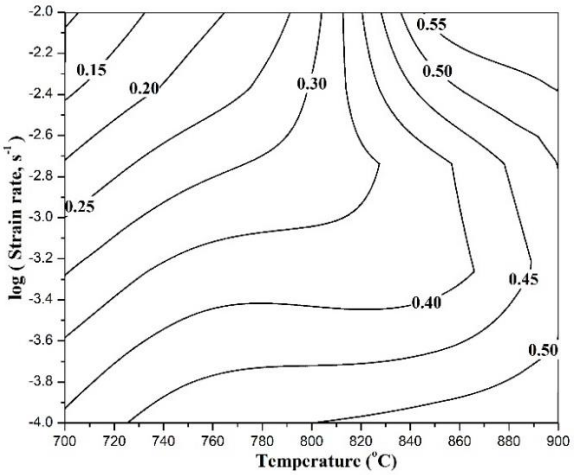

(c)

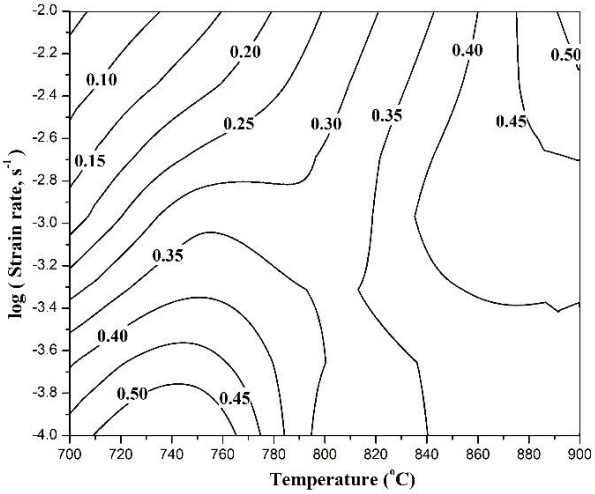

(d)

Figure 4.5 Contour maps representing *m* at various values of strains (a) 0.1, (b) 0.2, (c) 0.3 & (d) 0.4

4.2.2 Efficiency Maps

Processing maps are constructed depending on the dynamic material model (DMM), as presented by Prasad and Seshacharyulu (1998). In DMM, a dimensionless quantity known as the power dissipation (η) is utilized that suitably describes dissipation of energy via growth of the microstructure at diverse temperatures. However, functioning in the superplastic range can be stated with respect to temperature range and strain rate and it is termed as an efficiency map.

The variation in power dissipation comprises of numerous regions and all these regions may be correlated with different mechanisms of the microstructures viz., DRX, DRV and superplastic deformation behaviour. The Eq. for Efficiency (η) as given by Prasad et al. (2015) is derived as follows:

$$P = \sigma\,\dot{\varepsilon} = \theta\,\frac{d\,S}{dt} \geq 0 \tag{4.21}$$

$$P = \int_0^{\dot{\varepsilon}} \sigma\, d\dot{\varepsilon} + \int_0^{\sigma} \dot{\varepsilon}\, d\sigma = \mathrm{G} + \mathrm{J} \tag{4.22}$$

$$\Delta J \approx \int_{\sigma}^{\sigma+\Delta\sigma} \dot{\varepsilon}\, d\sigma \tag{4.23}$$

$$\Delta G \approx \int_{\varepsilon_0}^{\varepsilon_0+\Delta\varepsilon_0} \sigma\, d\dot{\varepsilon} \tag{4.24}$$

$$\Delta P \approx \mathrm{K}(\dot{\varepsilon} + \Delta\dot{\varepsilon})^{m+1} \tag{4.25}$$

$$\Delta J/_{\Delta G} = m \tag{4.26}$$

$$\Delta J/_{\Delta P} = m/_{(m+1)} \tag{4.27}$$

$$\frac{\Delta J/_{\Delta P}}{\left(\Delta J/_{\Delta P}\right)_{linear}} = \frac{m/_{(m+1)}}{1/_2} \tag{4.28}$$

$$\eta = \frac{2m}{m+1} \tag{4.29}$$

where, σ denotes flow stress (MPa), $\dot{\varepsilon}$ - strain rate and 'm' - strain rate sensitivity. Figure 4.6 represents efficiency maps generated at various strain values (a) 0.1, (b) 0.2, (c) 0.3 as well as (d) 0.4.

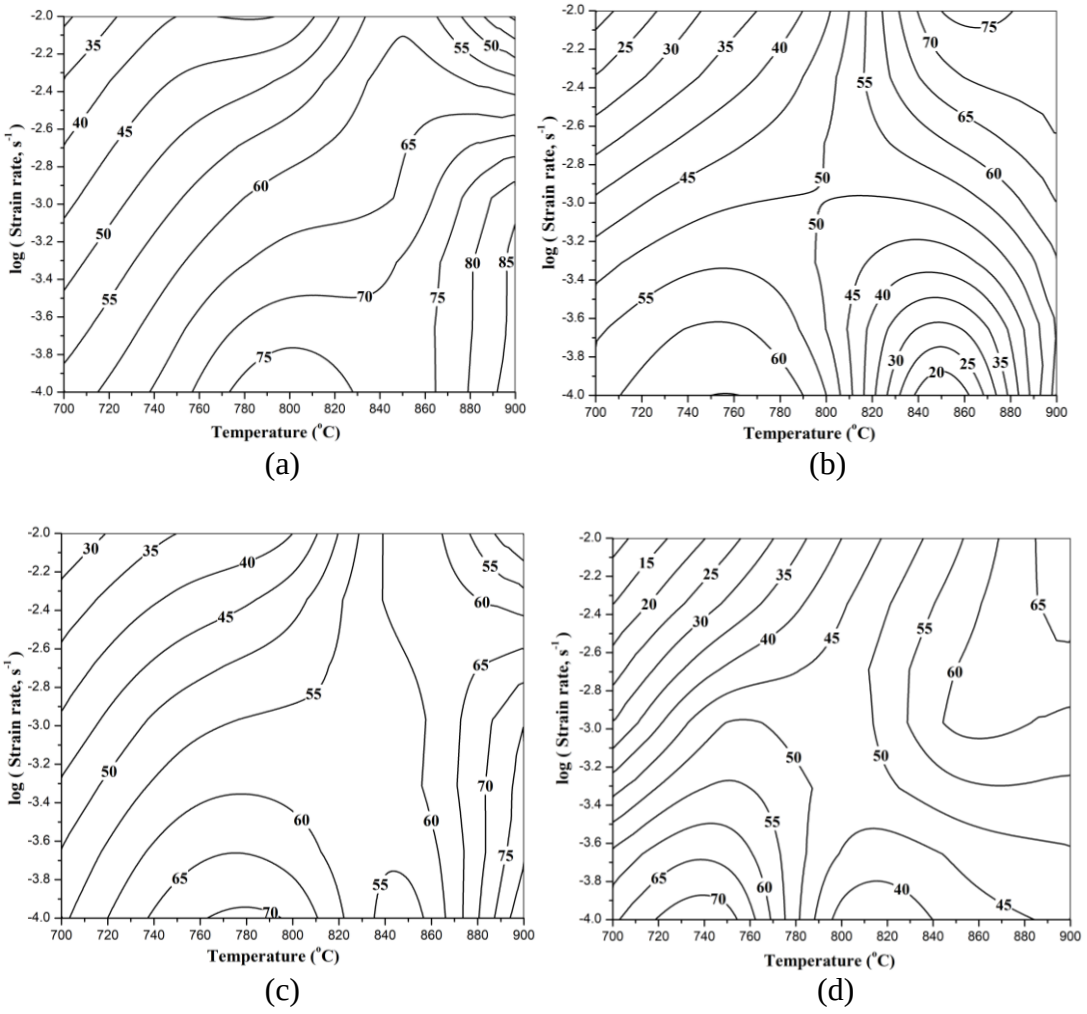

Figure 4.6 Efficiency maps generated at various strain values (a) 0.1, (b) 0.2, (c) 0.3 & (d) 0.4 respectively (Contour numbers in maps denote the efficiency.)

4.2.3 Instability Maps

An instability area/region is recognized based on maximum principle of irreversible thermodynamics to identify the flaws that take place during the hot working process namely flow localization, (DSA) dynamic strain ageing, etc. It is defined in terms of a dimensionless process parameter by Seshacharyulu et al. (2000) in Eq. (4.30) as:

$$\xi\ (\dot{\varepsilon}) = \frac{\partial\ ln\left(\frac{m}{m+1}\right)}{\partial\ ln\ \dot{\varepsilon}} + <\ 0 \qquad (4.30)$$

Statistically, instability takes place, when $\xi(\dot{\varepsilon})$ < zero, viz. a negative value and stability is recognized, when $\xi(\dot{\varepsilon})$ > zero viz. a positive value, as defined by Seshacharyulu et al. (2002).

In an instable region, negative value corresponds to flow instability, viz. greater the negative value, more is the possibility of occurring flow instability, whereas lower the negative value, less is the possibility of arising flow instability. However, a positive value corresponds to flow stability, viz. greater the positive value, higher is the possibility of occurring a stable deformation, similarly observed by Wang et al. (2016).

Finally, the development of processing map takes place by superimposing an instability map $\xi\ (\dot{\varepsilon})$ on an efficiency map (η).

Figure 4.7 represents instability maps generated at various strain values (a) 0.1, (b) 0.2, (c) 0.3 as well as (d) 0.4.

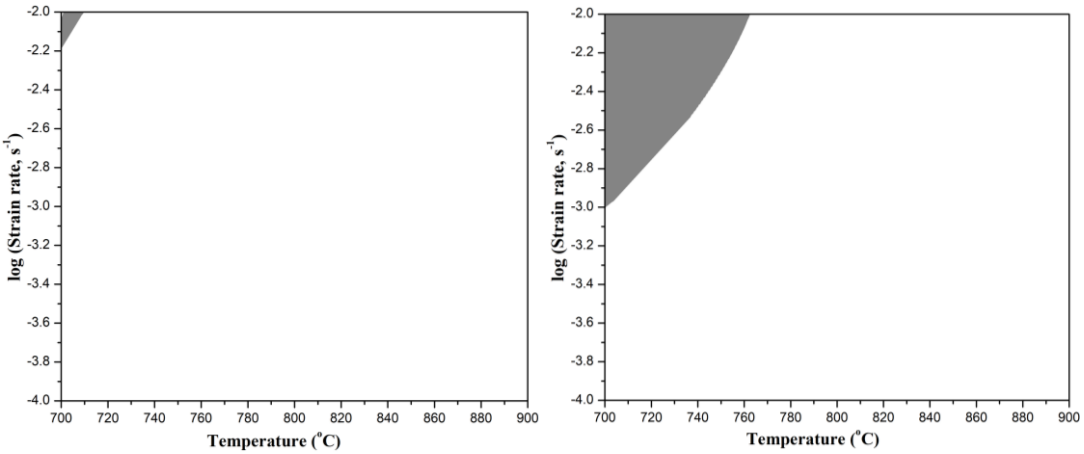

(a) (b)

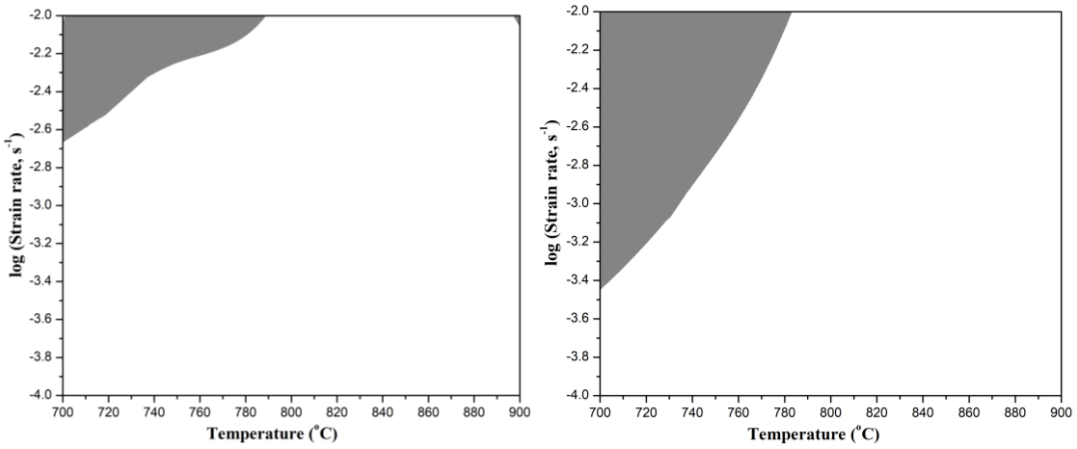

Figure 4.7 Instability maps generated at various strain values (a) 0.1, (b) 0.2, (c) 0.3 & (d) 0.4 (shaded region in maps denote the instability)

4.2.4 Processing Maps

The obtained *m* values have been applied to construct the respective efficiency (η) maps and instability $\xi(\dot{\varepsilon})$ maps. Depending on this, processing maps have been generated at various levels of strains, i.e., 0.1, 0.2, 0.3 as well as at 0.4 as presented in Figure 4.8 (a) - (d).

In all the presented Figures, the contour lines with numbers signify the percentage (%) of efficiency and the shaded region signifies the flow instability.

From these presented figures, it can be perceived that as the level of strain rises, the percentage of efficiency reduces and flow instability (shaded area) also rises steadily. A maximum percentage of efficiency of 85% is achieved at 0.1 strain value, it denotes that greater the percentage of efficiency, superior is the workability, similarly reported by Lukaszek-Solek and Krawczyk (2015). The flow instability area should be eluded, when working at high temperatures along with diverse strain rates.

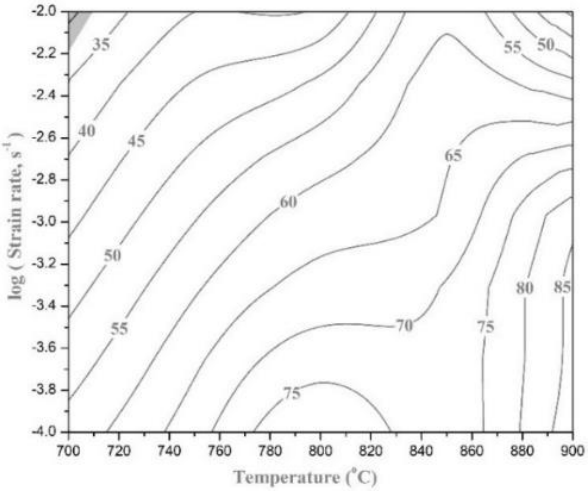
log (Strain rate, s^{-1})
Temperature (^{o}C)
35
40
45
50
55
60
65
70
75
80
85

(a)

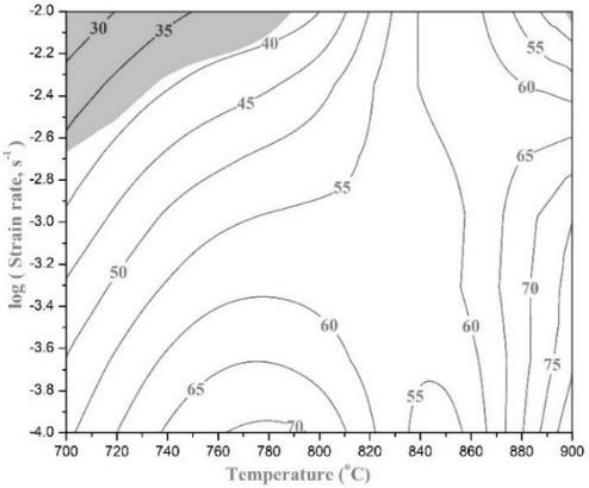
log (Strain rate, s^{-1})
Temperature (^{o}C)
30
35
40
45
50
55
60
65
70
75

(b)

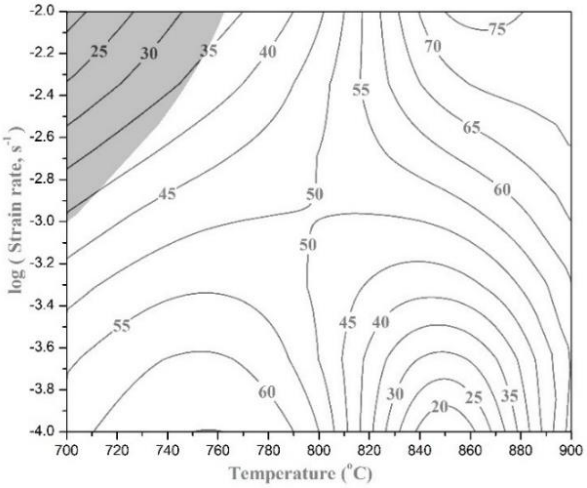
log (Strain rate, s^{-1})
Temperature (^{o}C)
20
25
30
35
40
45
50
55
60
65
70
75

(c)

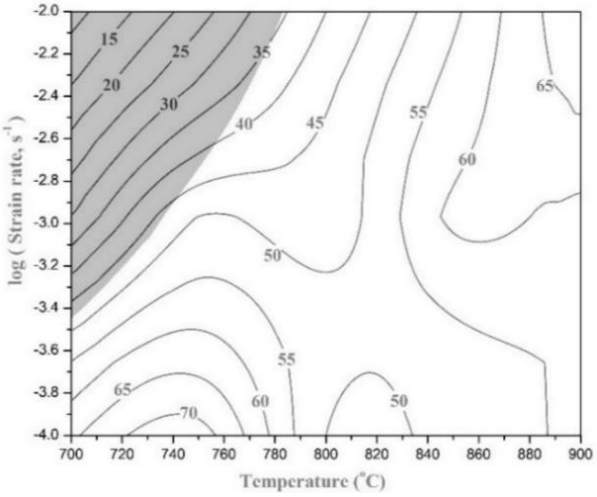

(d)

Figure 4.8 Processing maps generated at various strain values (a) 0.1, (b) 0.2, (c) 0.3 & (d) 0.4 (The contour numbers in maps signify the efficiency and shaded area in maps signify the instability)

Depending on the developed processing maps, the instability regions have been recognized at 700℃ and 10^{-2} s^{-1} at 0.1 strain as presented in Figure 4.8 (a). Flow instability used for strain values of 0.2 & 0.3 takes place at 700℃ & 750℃ at 10^{-2} s^{-1} as presented in Figure 4.8 (b) & (c). Flow instability for 0.4 strain takes place at 700℃ and 750℃ at 10^{-2} s^{-1} and at 700℃ at 10^{-3} s^{-1} as presented in Figure 4.8 (d).

Superplastic deformation area has been recognized from the presented processing maps, where the percentage of efficiency is higher as well as without having any flow instability varying from 770℃ - 900℃ and at 10^{-2} s^{-1} - 10^{-4} s^{-1} strain rate, i.e., this is the safest area to be used for hot deformation as presented in Figure 4.8 (a) - (d). It also shows that even with the rise of strain values, there does not exist any instability within the stated superplastic region. The obtained instabilities have been correlated with respective fractography and microstructure.

4.3. Correlation of Instability Region with Fractography and Microstructure

The fractography study conducted on ruptured tensile specimens for 700°C & 10^{-2} s^{-1} are shown in Figure 4.9. It indicates mainly a ductile failure shown by flow lines along with dimples on ruptured surface of the specimen.

Figure 4.9 (a) represents formation of a neck on specimen of size about 500µm approximately on the edges. From 300*X* magnification, the dimples seem to be stretched in a way perpendicular to the applied stress as apparent from Figure 4.9 (b).

Similar inferences have been confirmed from different magnifications i.e., at 800*X* from Figure 4.9 (c) & 1500*X* from Figure 4.9 (d). The specimen shows rupture due to localized necking, thus, indicating instability.

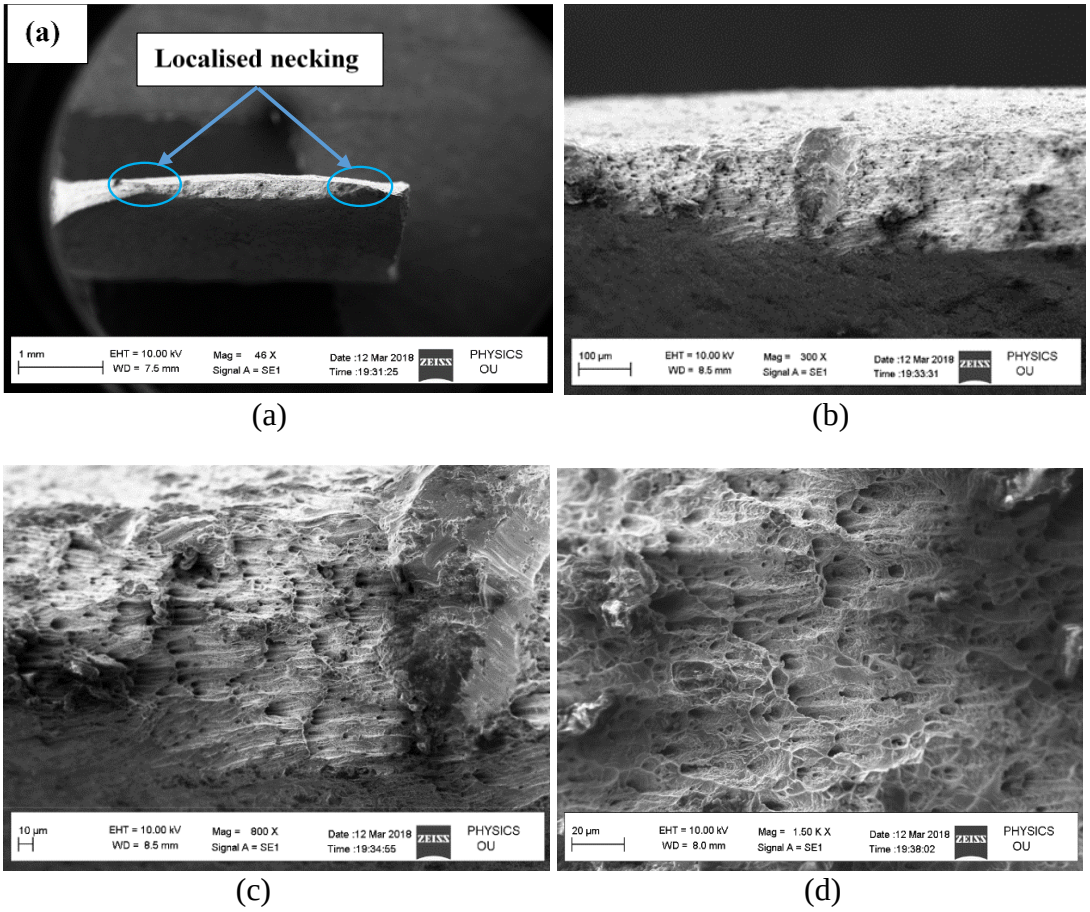

(a) (b)

(c) (d)

Figure 4.9 SEM images of ruptured specimens at 700°C and 10^{-2} s^{-1} strain rate at (a) 46*X*, (b) 300*X*, (c) 800*X* & (d) 1.5*kX* magnifications respectively

While, in other cases, viz., at 750℃ - 10^{-2} s^{-1} and at 700℃ - 10^{-3} s^{-1}, it shows ductile failure as identified by flow lines along with dimples as displayed in Figure 4.10 and Figure 4.11. From Figure 4.10 (a) & Figure 4.11 (a), thinning can be noticed on the cross section of specimens from where cracks develop leading to rupture and this could be a sign for the existence of these instabilities for the considered parameters.

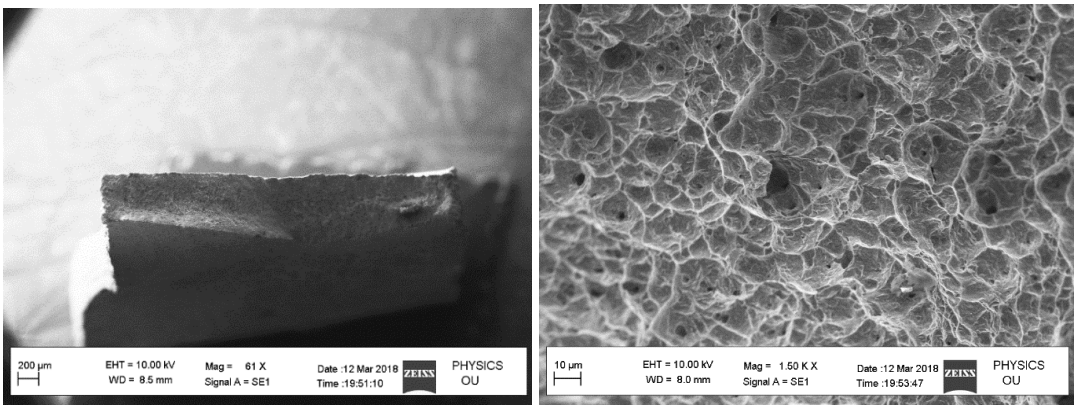

(a) (b)

Figure 4.10 SEM images of ruptured specimens at 750℃ and 10^{-2} s^{-1} at (a) 61*X* and (b) 1.5*kX* magnifications

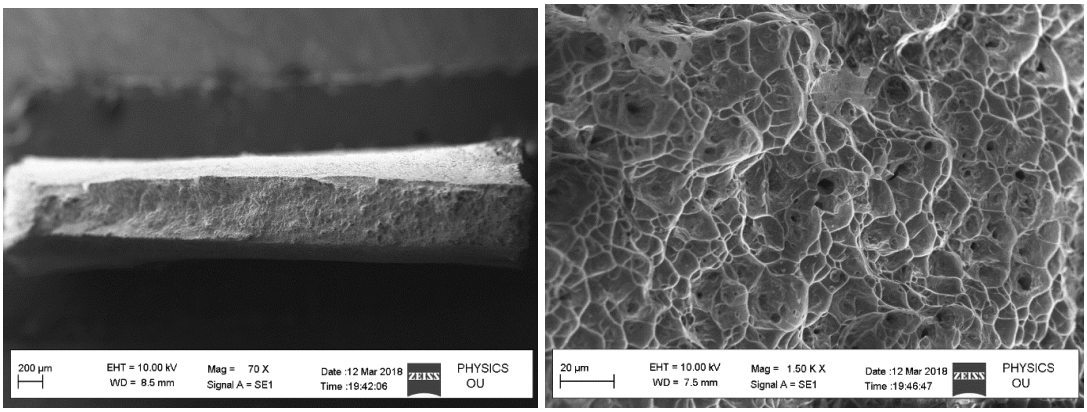

(a) (b)

Figure 4.11 SEM images of ruptured specimens at 700℃ and 10^{-3} s^{-1} at (a) 70*X* and (b) 1.5*kX* magnifications

Figure 4.12 represents optical micrographs of ruptured specimens (a) 700°C_10^{-2} s^{-1}, (b) 700°C_10^{-3} s^{-1} along with (c) 750°C_10^{-2} s^{-1} at 100*X*. Microstructure study has been conducted on specimens near ruptured region at obtained instabilities. However, in this area, none of the specimens indicate micro fractures. On the other hand, because of flow instability, namely localized necking or thinning, specimen ruptured, indicating the presence of instabilities.

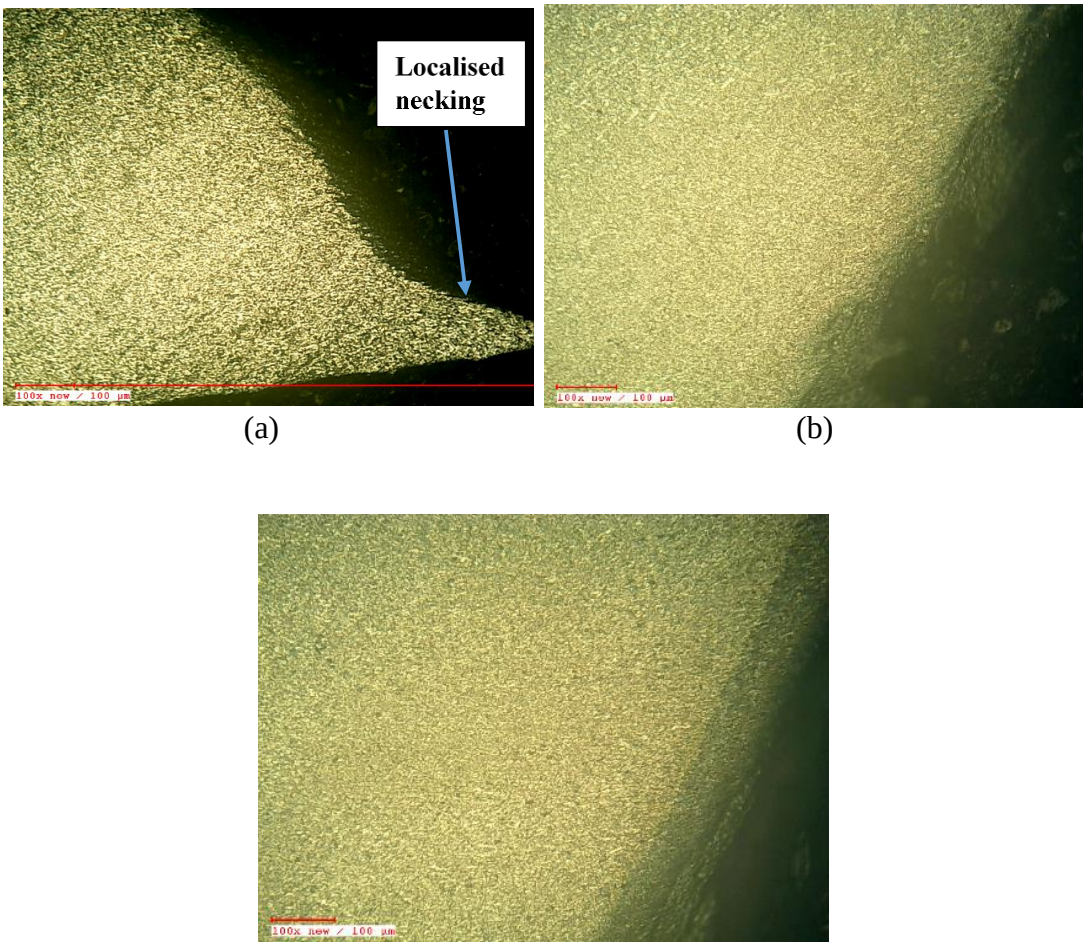

(a) (b)

(c)

Figure 4.12 Optical micrographs of ruptured specimens at (a) 700°C_10^{-2} s^{-1}, (b) 700°C_10^{-3} s^{-1} & (c) 750°C_10^{-2} s^{-1} at 100*X* magnification

4.4. Comparison of Instability Criteria

Instability criteria for Ti-6Al-4V alloy has been compared between Prasad and Murthy. Eq. 4.30 gives Prasad's criterion for instability, whereas Murthy's criterion is given by Eq. 4.31 (Cai, et al. 2016). Both these criteria have been used individually to develop instability maps at 0.1 and 0.4 strains respectively as shown in Figure 4.13. Numbers with negative signs and shaded region represent unstable region.

$$\xi\left(\dot{\varepsilon}\right) = \frac{\partial \ln\left(\frac{m}{m+1}\right)}{\partial \ln \dot{\varepsilon}} + m < 0 \qquad (4.30)$$

$$\xi\left(\dot{\varepsilon}\right) = \frac{2m}{\eta} - 1 < 0 \qquad (4.31)$$

It has been observed from Figure 4.13 (a & b) that Prasad's criterion shows the instable region, whereas from Figure 4.13 (c & d), Murthy's criterion does not predict any instable region. Therefore, to ensure the safety in hot tensile working in this study, Prasad's criterion has been considered to accurately predict the instable regions at high temperatures along with different strain rates, similarly reported by Sun et al. (2015).

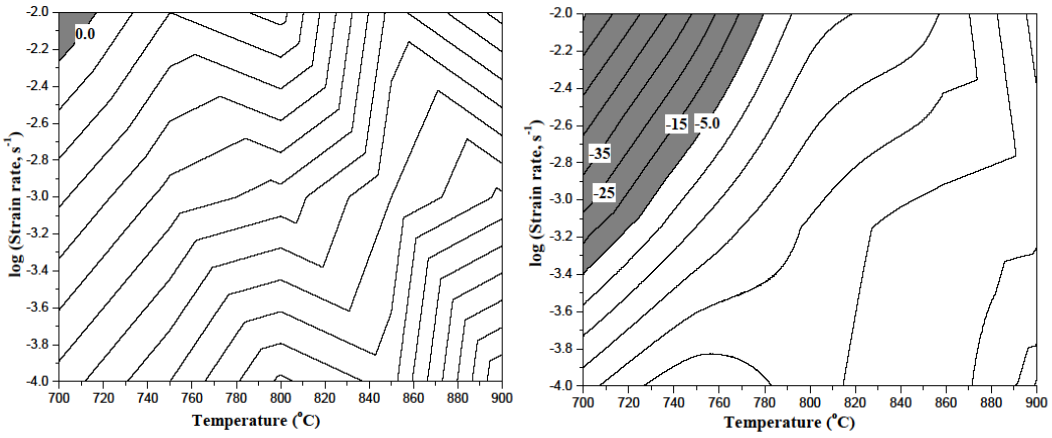

(a) (b)

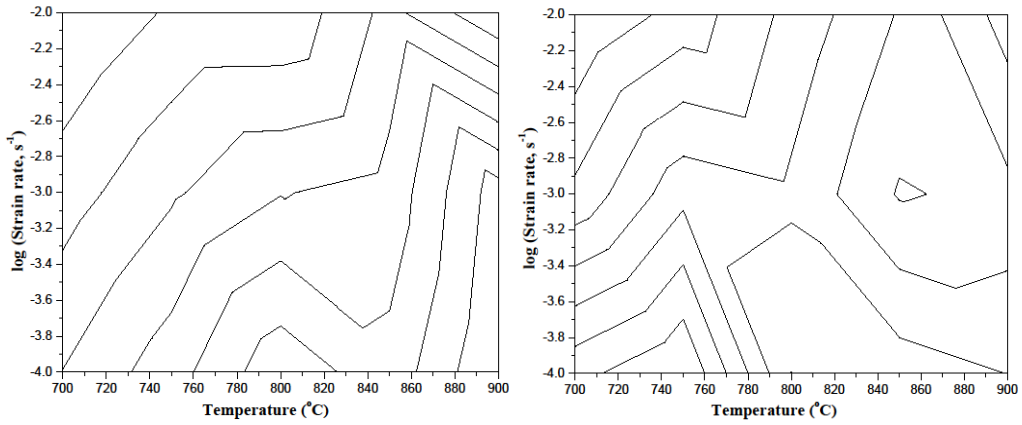

(c) (d)

Figure 4.13 Instability criteria (a & b) Prasad's and (c & d) Murthy's at 0.1 and 0.4 strains respectively

4.5. Comparison of Processing Maps

In the present study, uniaxial tensile tests have been conducted within a temperature range varying from 700°C - 900°C and at a strain rate range 10^{-2} s^{-1} - 10^{-4} s^{-1} and it forms as the basis for predicting superplastic behaviour. From Figure 4.8, at different strain values, superplastic deformation spectrum has been identified within a temperature range varying from 770°C - 900°C and at strain rate 10^{-2} s^{-1} - 10^{-4} s^{-1} with efficiency altering within the range of 40% - 85%. Higher the percentage of efficiency, better is the workability. However, flow instability takes place at 700°C - 10^{-2} s^{-1} and 10^{-3} s^{-1} and at 750°C - 10^{-2} s^{-1}. The existence of flow instability might be due to the localized necking or thinning. These instable regions should be avoided for better workability.

In a work reported in hot working guide textbook: a compilation of processing maps, from ASM international publisher by Prasad et al. (2015), compression tests have been performed on equiaxed Ti-6Al-4V alloy, within temperature range varying from 750°C - 1100°C along with strain rates $3x10^{-4}$ s^{-1} - 10^{2} s^{-1} and then processing map has been generated by means of flow stress data obtained at 0.5 strain as shown

in Figure 4.14. According to this work, they have classified the processing map into two areas viz. one in the dual phase (α+β) spectrum and the other in beta (β-Ti) spectrum.

Superplastic deformation spectrum is identified from 750°C - 1000°C viz, in (α+β) domain and at $3x10^{-4}$ s^{-1} to 10^{-2} s^{-1} with efficiency varying in the range of 40% - 52%. Flow instability occurs from strain rate greater than 1.0 s^{-1} and from 900°C - 1100°C temperature range and from strain rate greater than 10^{-2} s^{-1} within temperature 750°C - 900°C. Flow localization transpires within the flow instability area. In the β-Ti spectrum, 42% of efficiency has been observed.

The rate of flow softening is greater in tensile tests than in compression tests. Also, strain rate sensitivity varies in both the tests in hot working conditions, as reported by Miller et al. (1999). The specific contribution of this work in relation to the processing maps was to develop them based on tensile testing at different temperatures as well as strain rates, including the superplasticity regime. Whereas, Prasad et al. developed the processing maps for Ti-6Al-4V alloy at different temperatures as well as strain rates based on compression tests up to 50% strain which can be used only for applications involving compressive stresses.

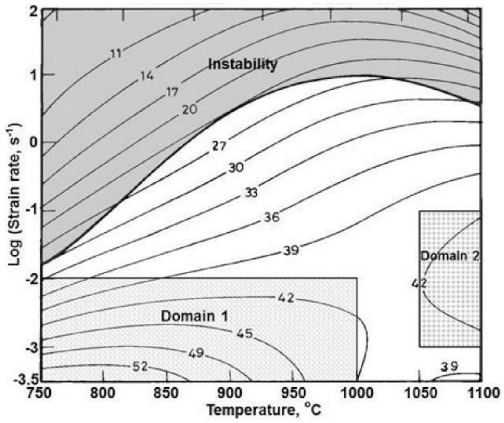

Figure 4.14 Processing map of Ti-6Al-4V alloy developed at 0.5 strain (Numbers denote efficiency & instability as shaded region) (Prasad, Rao and Sasidhara 2015)

4.6. Summary

This chapter discusses the development of constitutive model as well as processing maps. The modified-Arrhenius model has been considered to predict the hot tensile behaviour of Ti-6Al-4V alloy quite accurately. The calculated *m* values lie within the specified range of *m* for superplasticity of Ti-6Al-4V alloy. Based on these *m* values, instability and efficiency maps have been generated and superimposed to develop the processing maps. From processing maps, superplastic deformation has been recognized as stable regime, where the percentage of efficiency was high, whereas instable regimes have been correlated with fractography and microstructures and compared with different criteria.

Next chapter deals with experimental study of spring back behaviour in the V-bending process for Ti-6Al-4V alloy at high temperatures.

CHAPTER 5 : EXPERIMENTAL INVESTIGATION OF SPRING BACK IN V-BENDING PROCESS FOR TI-6AL-4V ALLOY

Though Ti-6Al-4V alloy is known for its superior qualities such as high melting point, high strength-to-weight ratio, low thermal conductivity and high corrosion resistance, but it suffers from the problem of high spring back behaviour, which can go even up to 30º at room temperature (Adamus and Lacki 2011). Spring back creates serious problems while manufacturing components as well as during assembly. Therefore, the present study has been focused to produce near-zero spring back effect by using a simple V-bending process at high temperatures. For this purpose, the experimental studies on spring back in V-bending process for Ti-6Al-4V alloy has been presented in Chapter 5 and its optimization to achieve near-zero spring back has been presented in Chapter 6 using finite element simulations. This will enhance application scope of Ti-6Al-4V alloy sheets to manufacture structural frames with superior strength and low weights.

In this chapter, the spring back behaviour in V-bending process at high temperatures has been studied using Taguchi methodology for designing the process parameters and ANOVA for identifying the significant key process parameters.

5.1. Experimental Set Up

V-bending tests have been carried out using computer controlled compression testing machine (CTM) of 2000 kN as presented in Figure 5.1 (a). The CTM is equipped with an externally attached three-zone split furnace having temperature capacity up to 1000°C and the inner part is surrounded with ceramic bricks to avoid heat loss as presented in Figure 5.1 (b). A temperature indicator and furnace controller have been used to indicate the temperature and to give input settings.

(a) (b)

Figure 5.1 (a) Compression testing machine and (b) Heating split furnace

V-bending punch as well as die used in the experiments have been manufactured with Nimonic alloy 80A for dimensional stability at high temperatures. Geometry of the punch as well as die used in V-bending experiments comprises of 60º bending angle along with 3 mm punch radius and 3 mm die radius. Dimensions of the punch and die in 2D model and combined in 3D CAD model are presented in Figure 5.2.

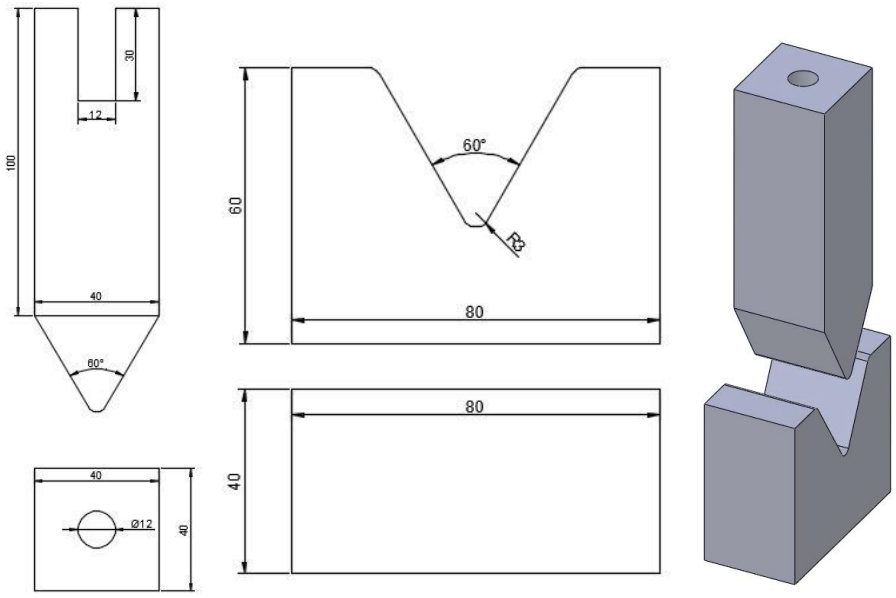

(a) (b) (c)

Figure 5.2 Schematic view of (a) 2D punch dimensions, (b) 2D die dimensions and (c) combined punch and die in a 3D CAD model

For using the punch and die, it required a complete set of arrangement such that a plate of stainless steel (SS) 316 was attached to a SS cylindrical bar of 100 mm diameter with the help of a tap screw. A slot was prepared on the cylindrical bar to press fit the punch and then this complete arrangement was attached to the top platen of the CTM with the help of C-clamps. Similarly, the die was placed on a SS cylindrical bar of 100 mm diameter with press fitted to a SS 316 plate and then kept on the bottom platen of the CTM. It was ensured that this complete arrangements of the punch and die properly encloses within the split furnace. In this way, both the punch and die have been loaded on the CTM and used for performing V-bending experiments as presented in Figure 5.3.

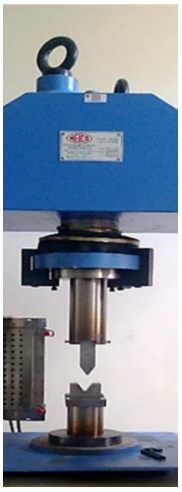

Figure 5.3 Loading of punch and die on CTM

The clearance between both the punch as well as the die have been kept as 1 mm. Ti-6Al-4V alloy sheet with 0.8 mm thickness was used and sheared along the rolling direction with the help of a shearing machine to sizes of 80 mm x 20 mm. Delta glaze coating has been applied on specimens to prevent oxidation at high temperatures and then kept on the die in such a way that rolling direction was perpendicular to the horizontal portion of the die.

V-bending specimens have been initially heated to the required temperature at a degree of 5°C/min and held for three minutes to ensure uniform heating and then V-bending experiments (loading/ holding/ unloading) have been performed followed by furnace cooling as presented in Figure 5.4.

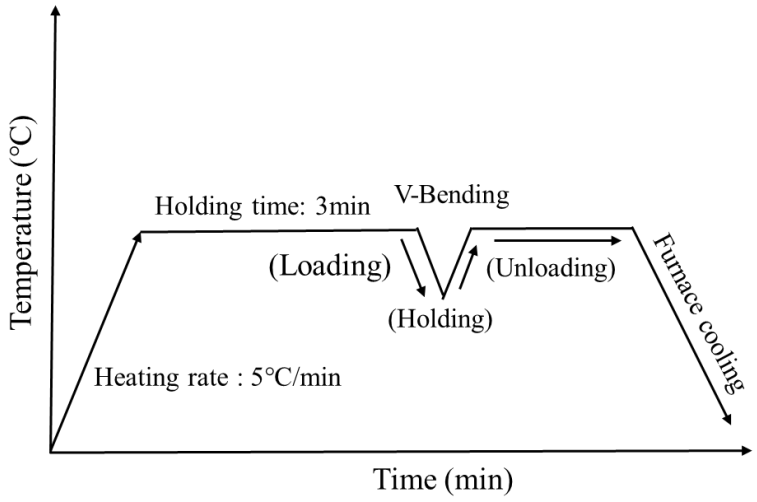

(a)

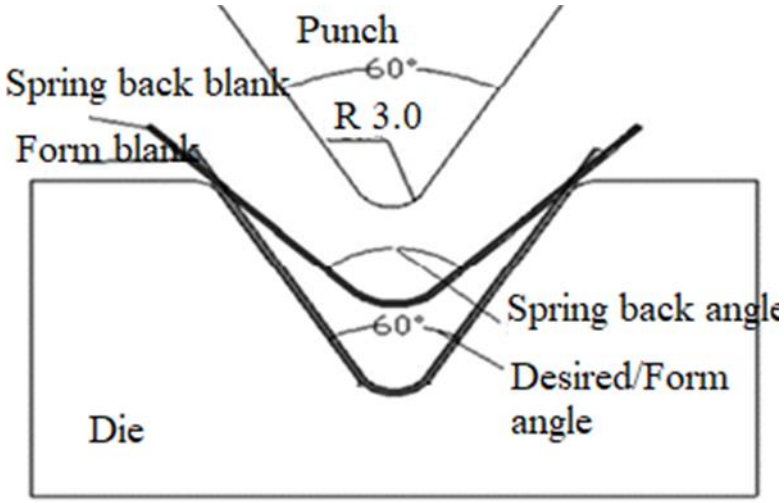

(b)

Figure 5.4 V-bending of Ti-6Al-4V alloy (a) process and (b) geometry

Each V-bending experiment has been conducted three times to attain accurate results. After completing the experiments, the angles of V-bend specimens have been measured using a coordinate measuring machine as shown in Figure 5.5 (a). The V-

bend specimen has been kept on a V block, and then points on each plane of the specimen has been selected one by one as shown in Figure 5.5 (b), followed by evaluation of the bend angle. After obtaining the bend angle, it has been subtracted from the initial bending angle to get the spring back value.

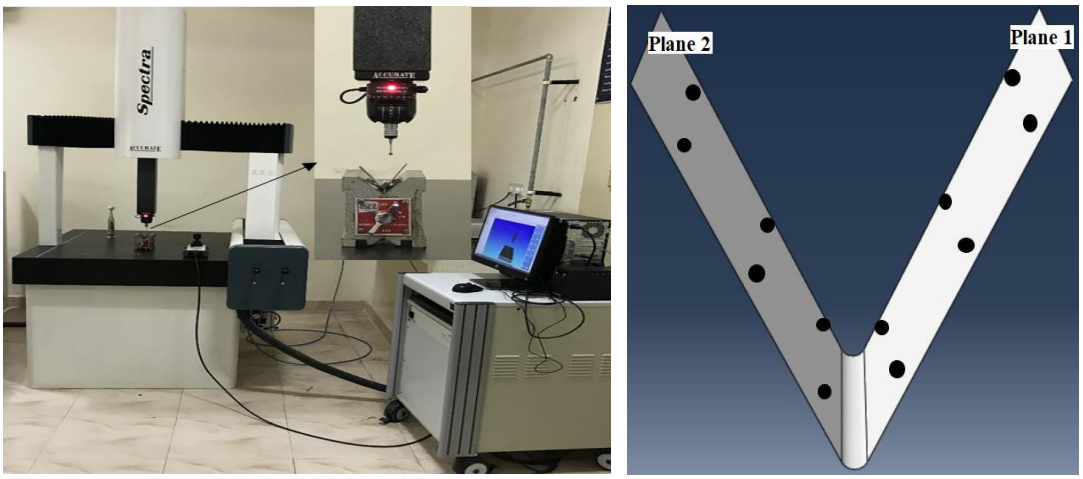

(a) (b)

Figure 5.5 (a) Coordinate measuring machine with V-bend specimen and (b) schematic of V-bend specimen showing measured points

5.2. Design of Experiments – Taguchi L_9 Orthogonal Array

In this study, for the experimental validation of simulation results, Taguchi L_9 orthogonal array has been used as a design of experiments for the V-bending process. Herein, the process parameters have been high temperature, punch speed as well as holding time and the objective has been to minimize the spring back behaviour of Ti-6Al-4V alloy. Taguchi method deals with the study of various process parameters without conducting a large amount of experiments and identifies suitable process parameters to acquire the best possible results of the process. Taguchi L_9 experimental design was used by Thipprakmas and Phanitwong (2011) for studying

the spring back behaviour in the V-bending simulations for A1100 alloy, considering the process parameters as varying thickness, punch radius as well as bending angle.

For robust design of experiments, signal to noise (S/N) ratio plays a main role, as it reduces the noise effect of the uncontrolled variables and helps in achieving optimum results. The objective of this work has been to minimize the spring back behaviour, for which the S/N ratio with smaller is better was selected and also, the significant percentage contribution of process parameters have been determined from ANOVA. The complete procedure of Taguchi method as adopted in this work is shown in Figure 5.6.

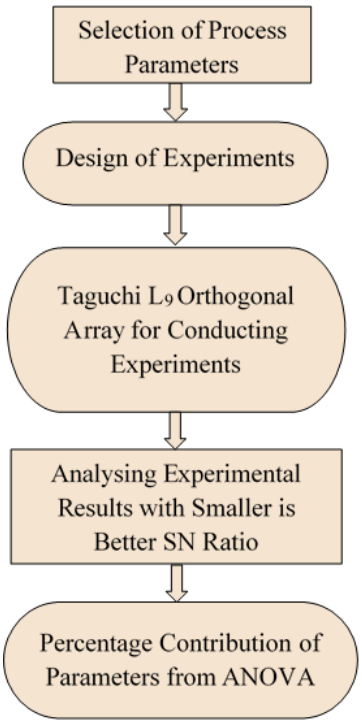

Figure 5.6 A flow chart of Taguchi method

In this study, high temperature, punch speed as well as holding time have been considered as process parameters for the V-bending experiment. The three level design of these process parameters as presented in Table 5.1 is due to the following reasons:

- Giuliano (2011) has recommended that temperature in the range of 700℃ - 900℃ gives minimum spring back.
- Lower punch speeds (0.01, 0.05 & 0.1 mm/sec) have been selected, in order to avoid impact loading effect.
- Holding time (0, 1 & 10 minutes) have been selected such that higher the temperature minimum is the holding time required, similarly used by Zong et al. (2015).

Table 5.1 Three level design of process parameters

Temperature (℃)	**Punch speed (mm/sec)**	**Holding Time (min)**
700	0.01	0
800	0.05	1
900	0.1	10

For conducting V-bending experiments, Taguchi L_9 orthogonal array has been implemented using Minitab software version 16, which is presented in Table 5.2.

Table 5.2 Design of parameters according to Taguchi L_9 orthogonal array

L_9 Orthogonal array	**Temperature (℃)**	**Punch speed (mm/sec)**	**Holding Time (min)**
1	700	0.01	0
2	700	0.05	1
3	700	0.1	10
4	800	0.01	1
5	800	0.05	10
6	800	0.1	0
7	900	0.01	10
8	900	0.05	0
9	900	0.1	1

In Taguchi analysis, the S/N ratio, smaller is better has been considered to minimize the spring back as presented in Eq. (5.1). The mean for total parameters ($\overline{S/N}$) is presented in Eq. (5.2) and the mean for distinct parameters (SS_i) is presented in Eq. (5.3), whereas sum of squares relating to deviations of the total mean (SS) is presented in Eq. (5.4). The percentage of contribution of individual parameters have been estimated, as it gives a degree of prominence of distinct parameters is presented in Eq. (5.5), as used by Thipprakmas and Phanitwong (2011).

$$SN_s = -10\log\left(\frac{1}{n}\sum_{i=1}^{n} y_i^2\right) \tag{5.1}$$

$$\overline{S/N} = \frac{1}{9}\sum_{k=1}^{9}(S/N)_k \tag{5.2}$$

$$SS_i = \sum_{j=1}^{3}\left((S/N)_{ij} - \overline{S/N}\right)^2 \tag{5.3}$$

$$SS = \sum_{i=1}^{9}\left((S/N)_{ij} - \overline{S/N}\right)^2 \tag{5.4}$$

$$\%\ \text{Contribution}_i = \left(\frac{SS_i}{SS}\ x\ 100\right) \tag{5.5}$$

5.3. Experimental Results of Spring back in V-Bending Process

The V-bending experiments have been carried out as per L_9 orthogonal array and the obtained V-bend specimens have been presented in Figure 5.7.

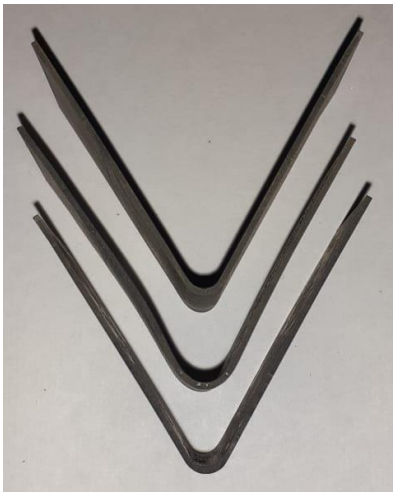

700_0.01_0

700_0.05_1

700_0.1_10

800_0.01_1

800_0.05_10

800_0.1_0

900_0.01_10

900_0.05_0

900_0.1_1

Figure 5.7 V bent samples as per Taguchi L_9 orthogonal array

The outcome of L_9 orthogonal array with an average of three spring back values and S/N ratio of individual setting are presented in Table 5.3. It can be observed that higher the signal to noise ratio (positive), minimum was the spring back (negative) and at the same time, it matches with the best possible setting as per L_9 orthogonal array S/N ratio. While, lower the S/N ratio (negative), maximum was the spring back (positive - away from zero) and it refers to a different set of parameters.

Table 5.3 Experimental spring back values for Taguchi L_9 orthogonal array

Temp (°C)	**Punch speed (mm/s)**	**Holding time (min)**	**Exp. spring back value (degree)**				**S/N ratio**
			SB_1	**SB_2**	**SB_3**	**Avg.**	
700	0.01	0	3.098	3.375	3.226	3.233	-10.197
700	0.05	1	3.283	3.437	3.415	3.378	-10.575
700	0.1	10	3.476	3.469	3.307	3.417	-10.676
800	0.01	1	1.905	1.873	1.835	1.871	-5.442
800	0.05	10	2.203	2.354	2.164	2.240	-7.012
800	0.1	0	1.114	1.124	1.028	1.088	-0.744
900	0.01	10	0.459	0.654	0.557	0.556	5.000
900	0.05	0	-0.113	-0.119	-0.115	-0.116	18.733
900	0.1	1	0.549	0.574	0.483	0.535	5.405

Figure 5.8 illustrates the boxplot of each setting (L_9) with different combination of process parameters showing spring back expressing, SB_1: Upper whisker designates the top vertical line existing on the box demonstrating the value of maximum spring back:- 3.476. *Q3* describes the top straight line (horizontal) of the box representing ≤ 75% of spring back values: 3.190. *Q2* describes the middle straight line (horizontal) of box signifying ≤ 50% of spring back values: 1.905 i.e., median and *Q1* designates the bottom straight line (horizontal) of box demonstrating

≤ 25% of spring back values: 0.504. Lower whisker describes the bottom vertical line of the box demonstrating minimum spring back: -0.113.

Correspondingly, for SB_2: Upper whisker value: 3.469. *Q3* value: 3.406, *Q2* value: 1.873 (median) & *Q1* value: 0.614. Lower whisker value: -0.119. Simultaneously, SB_3: Upper whisker value: 3.415. *Q3* value: 3.266, *Q2* value: 1.835 (median) and *Q1* value: 0.520. Lower whisker value: -0.115 respectively.

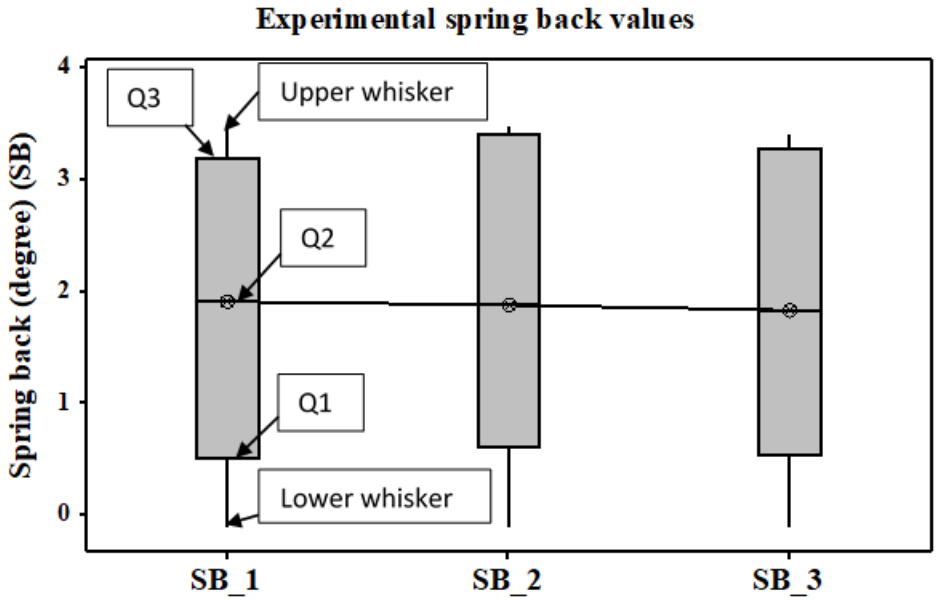

Figure 5.8 Box plot displaying spring back values (SB_1, SB_2 & SB_3)

At the same time, the main effect plots for S/N ratios with smaller is better is presented in Figure 5.9. It gives the possible set of parameters according to the L_9 orthogonal array namely temperature point 700°C, holding time 10 minutes along with punch speed value as 0.01 mm/s respectively.

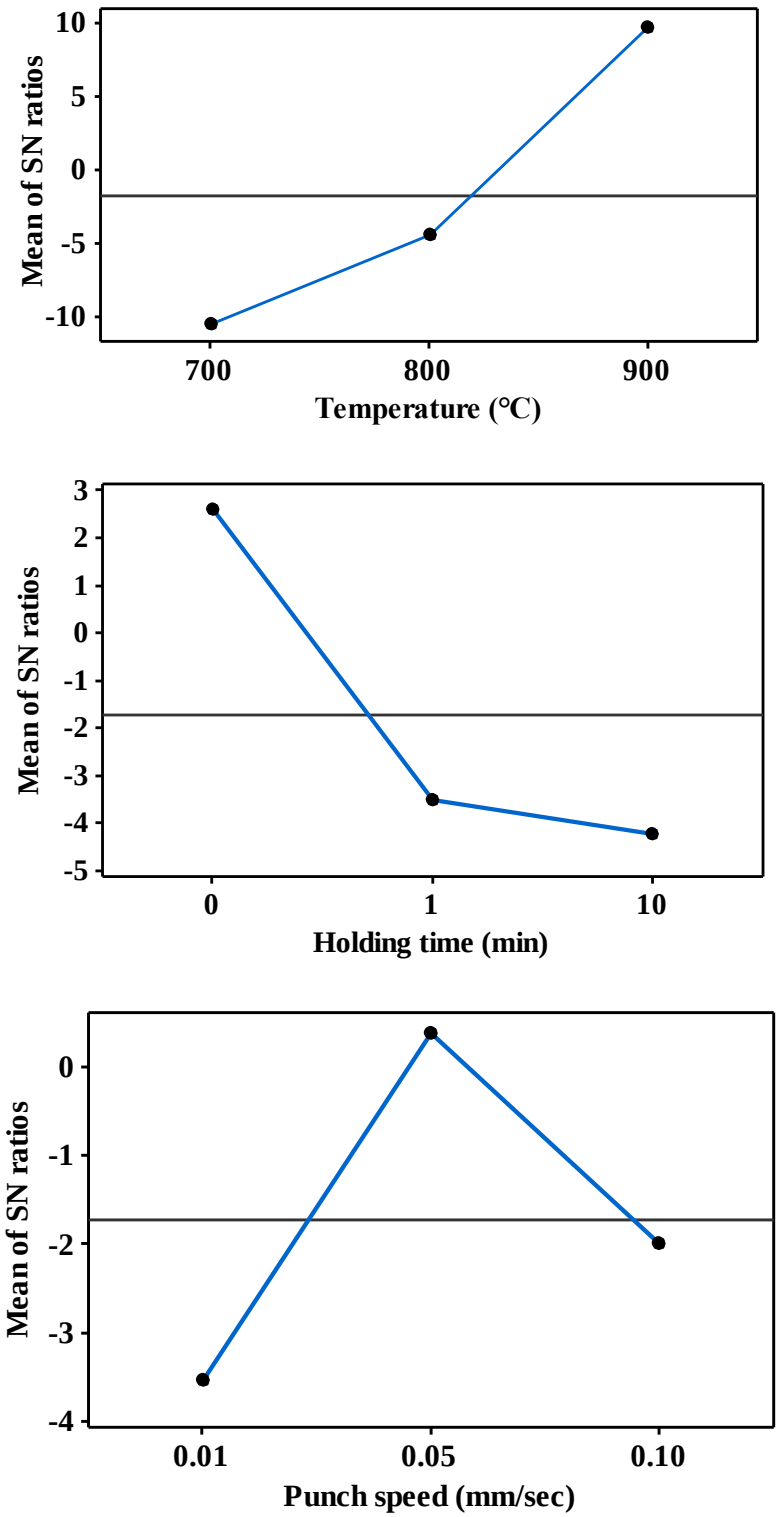

Figure 5.9 Main effect plots of process parameters for smaller is better SN ratios

5.4. Analysis of Variance and Percentage Contribution

ANOVA has been performed by means of Eqs (5.2) to (5.5) and presented in Table 5.4. Hence, Table 5.4 shows that SS_i for individual process parameters was highest in temperature then in holding time and punch speed and from (SS_i), percentage of contribution for individual process parameters have been calculated.

Table 5.4 ANOVA outcome for experimentation spring back

Process parameters	**Temperature (°C)**			**Punch speed (mm/s)**			**Holding time (min)**		
	700	**800**	**900**	**0.01**	**0.05**	**0.1**	**0**	**1**	**10**
$(S/N)_{ij}$	-10.48	-4.39	9.71	-3.54	0.38	-2.00	2.59	-3.53	-4.22
Sum of Squares (SS_i)	214.67			23.17			28.23		
(%) Contribution	80.68			8.70			10.61		

Therefore, depending on the percentage of distinct parameter contribution, it was observed that temperature has a main role in attaining minimum spring back subsequently followed by holding time and then punch speed. These results are analogous to the results achieved by Ramadass et al. (2019) from ANOVA study on Grade 2 titanium alloy. The significance of individual process parameter's contribution can be observed from the interaction plots, which are presented in Figure 5.10 (a) and (b). It can be perceived here that as temperature rises spring back reduces without much interaction with other process parameters. This shows the significance of temperature as an individual parameter in minimizing spring back. Whereas, from Figure 5.10 (c) & (d), it can be observed that parameters namely punch

speed as well as holding time interact at different levels with the temperature in minimizing the spring back.

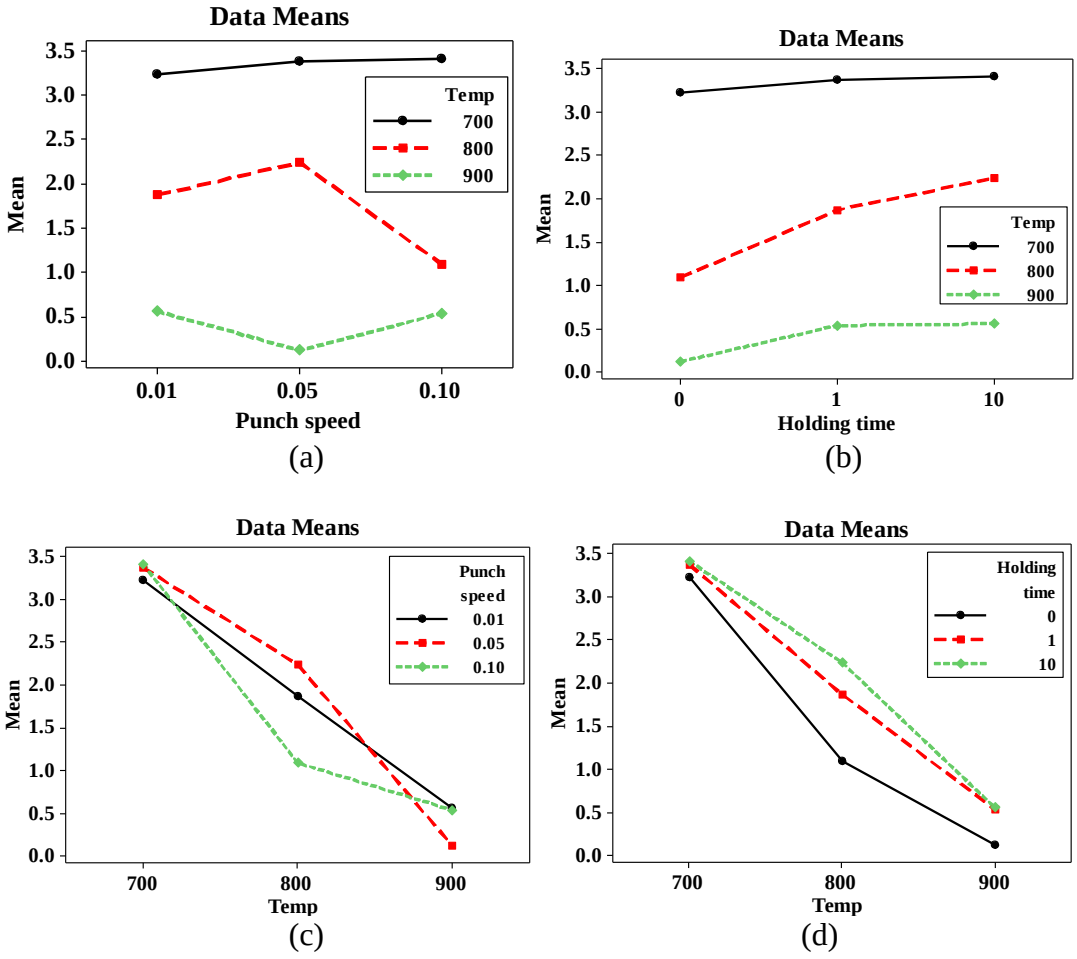

Figure 5.10 Interaction plots for spring back in (a) temp vs. punch speed, (b) temp vs. holding time, (c) punch speed vs. temp and (d) holding time vs. temp

Furthermore, from stress vs. strain plots as shown in Figure 3.7, it can be perceived that there has been a reduction in the yield stress as temperature increases from 700°C - 900°C. Hence, this also reduces spring back behaviour.

5.5. Comparison of Spring back between Room and High Temperatures

It can be observed from the experimental results as shown in Figure 5.11 (a) that spring back of Ti-6Al-4V alloy at room temperature was determined as 13º, it might be due to high yield strength and low Young's modulus, as also reported by Adamus and Lacki (2011). From Figure 5.11 (b) & (c), it can be inferred that spring back decreases from 3º to 0.5º respectively for V-bending experiments conducted at 700℃ and 900℃ in comparison with the room temperature experiment, this might be due to the effect of temperature in reducing the yield strength as well as the elastic modulus.

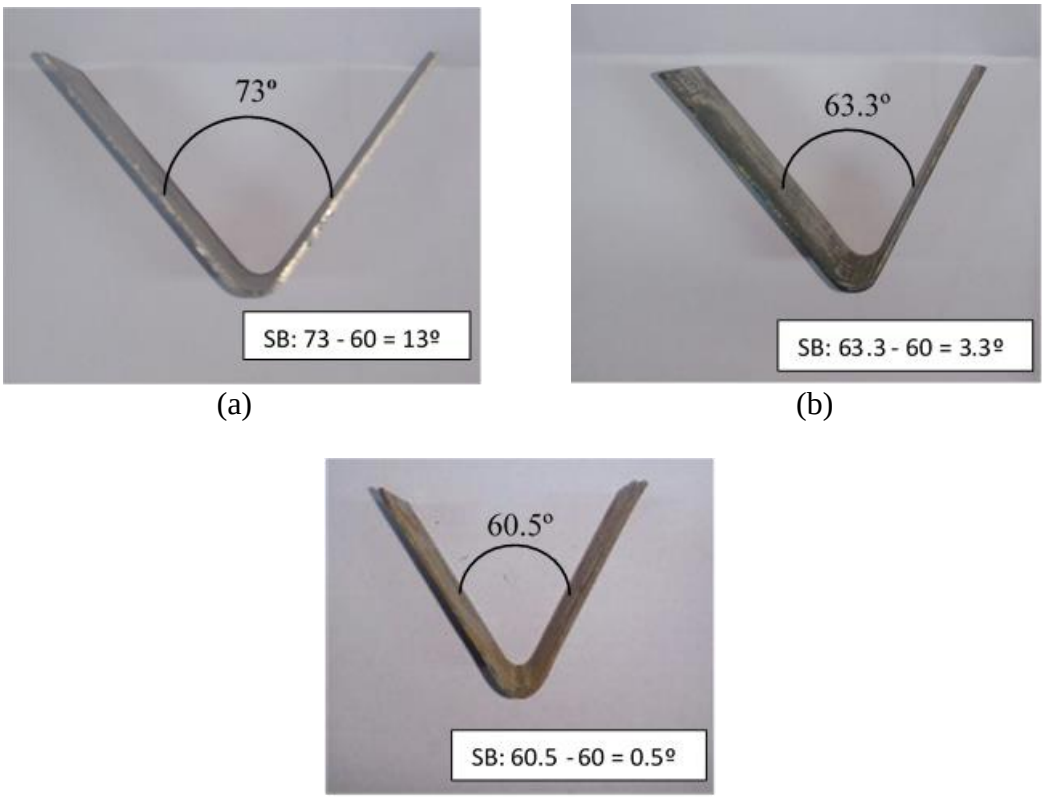

Figure 5.11 Experiementally measured spring back values at (a) RT, (b) 700℃ and (c) 900℃

5.6. Spring back Factors

Spring back has been evaluated by using different factors i.e., spring back ratio & spring back effect as given in Eqs 5.6 and 5.8 (Martinez and Medellín-Castillo 2019) and spring back factor (Kalpakjian and Schmid 2009) as given in Eq. (5.7) ,

$$\text{Spring back ratio } (K) = \frac{\alpha_{\text{final}}}{\alpha_{i\text{nitial}}} \tag{5.6}$$

$$\text{Spring back factor } (K_s) = \frac{\left(2R_i/_t\right) + 1}{\left(2R_f/_t\right) + 1} \tag{5.7}$$

where R_i & R_f means the initial as well as the final bend radii.

$K_s = 1$ (no spring back)

$K_s = 0$ (total elastic recovery)---

$$\text{Spring back effect} = \frac{\alpha_{\text{final}} - \alpha_{\text{initial}}}{\alpha_{i\text{nitial}}} \tag{5.8}$$

where α_{initial} - die bending angle and α_{final} - bending angle (after SB) respectively.

By using Eq. 5.6, spring back ratio (K) has been found to be greater than unity in most of the L_9 orthogonal settings. By using Eq. 5.7, the spring back factor (K_s) has been calculated and obtained to be varying from 0.80 to 0.87, whereas by using Eq. 5.8, spring back effect has been calculated and found to be in the range of 0.008 to 0.050 i.e., these two parameters (spring back factor and spring back effect) indicate minimum spring back.

5.7. Summary

This chapter discusses experimental study of spring back behaviour in V-bending process based on Taguchi L_9 orthogonal array. For these experiments, S/N ratio smaller is better was considered and it revealed that higher the signal to noise ratio lowest was the spring back, whereas lower the signal to noise ratio, highest was the spring back. ANOVA conveys that depending on the percentage of contribution, temperature has a main role in attaining minimum spring back, subsequently followed by holding time and then punch speed. Furthermore, spring back was evaluated using different factors indicating minimum spring back.

Next chapter deals with FE modelling of V-bending process and optimization of spring back values using RSM and GA.

CHAPTER 6 : FINITE ELEMENT ANALYSIS AND OPTIMIZATION OF SPRING BACK BEHAVIOUR IN V-BENDING OF TI-6AL-4V ALLOY

This chapter focusses on FE modelling and analysis of spring back behaviour in V-bending of Ti-6Al-4V alloy at high temperatures. The results of this FE study have been verified and found to be analogous with the experimental results for L_9 orthogonal array, which were presented in the previous chapter. Further, this FE model has been used for a full factorial design of experiments and the consequent results have been used for determining the optimum process parameters for minimizing spring back values using RSM and GA.

6.1. FE Modelling of Spring back Behaviour in V-Bending Process

In this study, the commercial FEA software ABAQUS version 6.14 has been used for performing V-bending simulations. The system configuration applied for simulating V-bending process is as follows: Manufacturer: Dell, Processor: Intel (*R*) Xenon (*R*), CPU: E3-1270 V2, at the rate 3.50 GHz, RAM: 16.0 GB and Operating System - Windows 7. The steps implemented in FE analysis are presented in Figure 6.1.

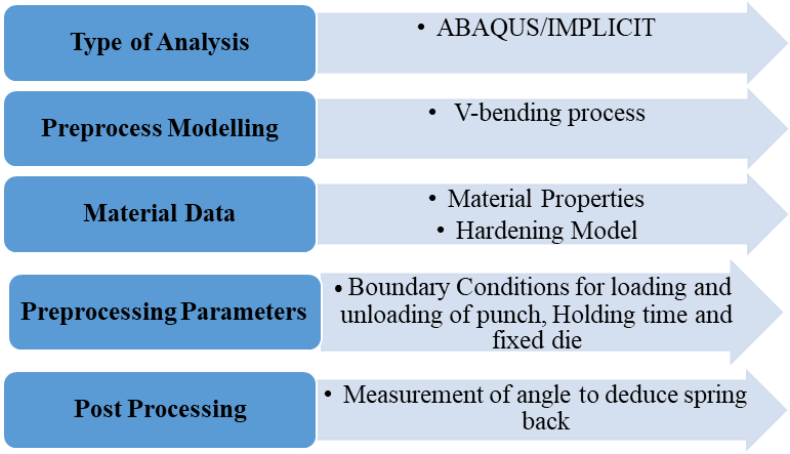

Figure 6.1 Steps implemented in FEA

The complete simulation has been carried out in 2D as shown in Figure 6.2, because of less thickness of the specimen when matched to its width, similarly performed by Chan et al. (2004) and there might be minimal strain along the width of the specimen. Only the Ti-6Al-4V alloy blank (specimen) has been considered as deformable and the V-bending punch as well as die have been considered as rigid. Type of element used for the punch and die was R2D2 - a 2 node 2D linear rigid link.

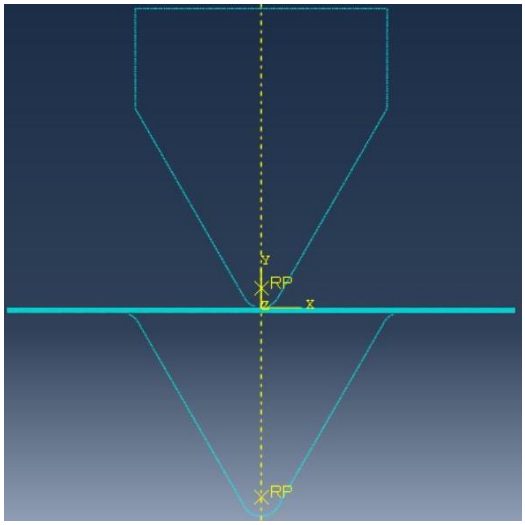

Figure 6.2 2D FE model of V-bending process

At high temperatures, one of the main reason spring back reduces is due to lower magnitude of Bauschinger effect, as reported by Banabic (2010). Therefore, the isotropic hardening approach has been considered to better predict the spring back behaviour.

The material properties of Ti-6Al-4V alloy at high temperatures such as Modulus of Elasticity and Poisson's ratio have been defined from the materials properties handbook of titanium alloys (Boyer, Welsch and Collings 1994), to define elastic data, whereas true stress vs. true strain data have been used to define plastic data and the density of Ti-6Al-4V alloy has been considered as 4.5 g/cc. V-bending

simulations have been performed using different process parameters – temperature, punch speed and holding time. The percentage error less than 10% has been obtained between simulation and experiments for spring back values.

After assigning all the material properties, assembly of the parts have been completed and the working model has been prepared with 60º bending angle along with 3 mm punch and die radii. The loading step, holding step and unloading step as presented in Figure 6.3 (a) - (d) have been modeled in ABAQUS/IMPLICIT (as it considers material, geometry and boundary non linearities).

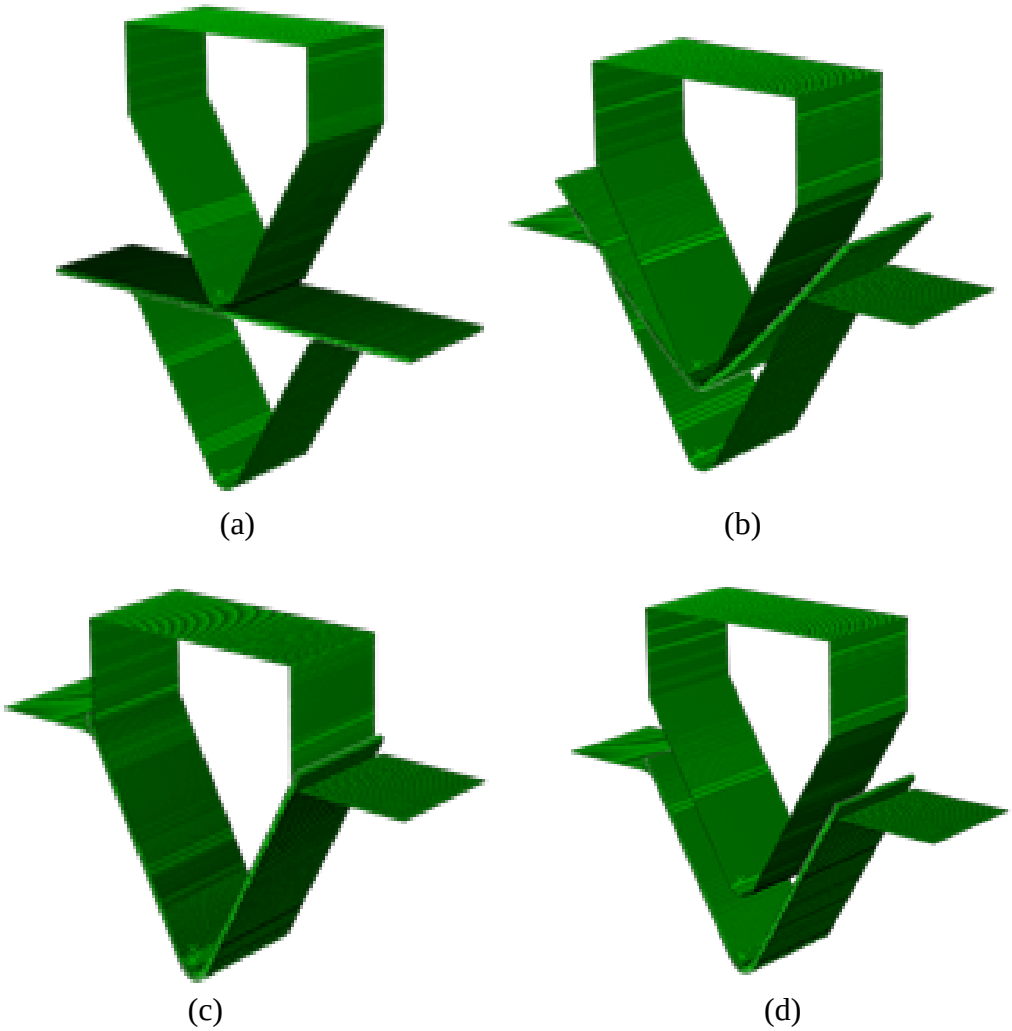

Figure 6.3 FE modelling of V-bending process (a) initial step, (b) loading step, (c) holding step and (d) unloading step

In the interaction section, coefficient of friction (μ) has been fed as 0.1 (Boyer, Welsch and Collings 1994). In boundary conditions: V-bending die has been made fixed, whereas loading of the punch has been restricted to move in *y*-axis direction only with speeds 0.01, 0.05, 0.1 mm/s and unloading at a fixed speed of 10 mm/s.

In the step section: holding time as 0, 1 and 10 minutes have been used to stabilize the process. For meshing of the blank, CPE4R - four node bilinear plane strain quadrilateral, reduced integration, hourglass control shell element has been applied, similarly considered by Chan et al. (2004).

Mesh sensitivity analysis have been carried out with different element sizes. Depending on this, no. of layers, no. of elements, no. of nodes and total CPU time taken have been calculated and presented in Table 6.1.

Table 6.1 Mesh sensitivity analysis

S.No.	**Element size (mm x mm)**	**No. of layers**	**No. of elements**	**No. of nodes**	**Total CPU time (sec)**
1	0.025 x 0.025	32	102400	105633	17263
2	0.05 x 0.05	16	25600	27217	3640
3	0.075 x 0.075	11	11726	12804	1378
4	0.1 x 0.1	08	7272	8012	655

Based on this complete analysis, the element with 0.05 mm x 0.05 mm has been considered, since it has an error of < 1% as compared to the element size of 0.025 mm x 0.025 mm. Moreover, it was 4.74 times faster in simulating the V-bending process. Boundary conditions and adopted blank meshing are presented in Figure 6.4.

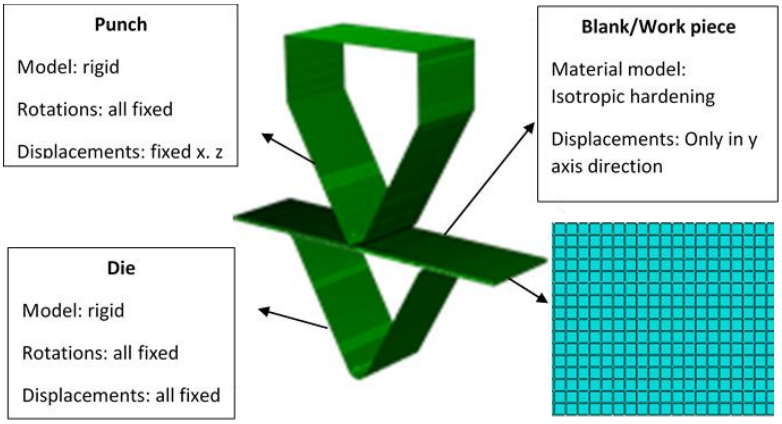

Figure 6.4 Boundary conditions and blank meshing

The entire simulation has been assumed to be done in isothermal condition and heat dissipation has been neglected. Finally, V-bending simulation has been executed and the spring back measurement has been performed by choosing the coordinates of selected nodes on the blank viz. at loading step and unloading step, using the formula of slope given in Eq. 6.1,

$$\theta = \tan^{-1}\left(\frac{y_2 - y_1}{x_2 - x_1}\right) \tag{6.1}$$

where 1 as well as 2 indicate the coordinates of selected nodes along *x* and *y*.

Furthermore, after completing pre-processing of spring back behaviour in V-bending process, post processing has been studied, which is discussed in the next section.

6.2. FE Analysis of Spring back Behaviour in V-Bending Process

The spring back behaviour using Ti-6Al-4V alloy was studied by applying FE simulations and its validation with experimental results, to know the effect of parameters namely, high working temperatures, varying punch speed as well as holding time. The last unloading step showed that with rise of temperature and with an amalgamation of other two distinct parameters, spring back decreases to a major extent viz. from 3º_700℃ - 0.5º_900℃ as presented in Figure 6.5.

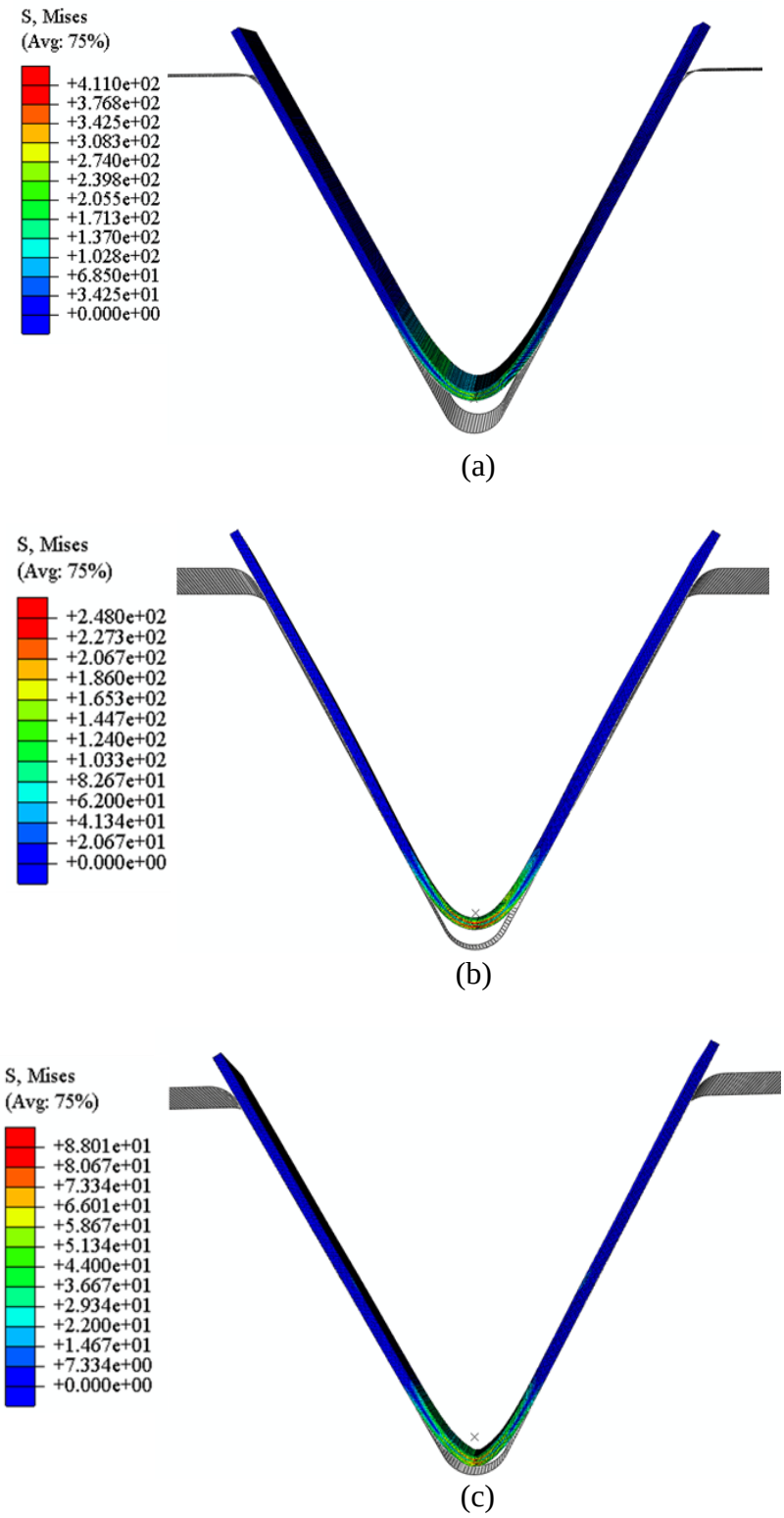

Figure 6.5 FE simulation outcome of unloading step (a) 700-0.05-1, (b) 800-0.1-0 & (c) 900-0.01-10

6.3.Comparison of Experimental and Simulation Results

The outcomes acquired from FE simulations and conducted experiments as per L_9 orthogonal array by means of high temperature, varying punch speed as well as holding time was compared based on the percentage of error as presented in Table 6.2. It can be perceived that the percentage of error is less than 10% in all the cases having a mean of 7.35% and standard deviation of 1.24%. Simultaneously, Pearson correlation has been determined between simulations and experimentations and has been found as 0.997, which shows that FE simulation outcomes are much similar with the experimental outcomes.

Table 6.2 Comparison between simulation & experimentation outcomes

Temp. (°C)	Punch speed (mm/s)	Holding time (min)	Simulation SB (degree)	Experimental SB (degree)	Error (%)
700	0.01	0	2.921	3.233	9.650
700	0.05	1	3.082	3.378	8.771
700	0.1	10	3.194	3.417	6.535
800	0.01	1	1.978	1.871	5.718
800	0.05	10	2.065	2.240	7.826
800	0.1	0	1.025	1.088	5.848
900	0.01	10	0.514	0.556	7.664
900	0.05	0	-0.108	-0.116	6.628
900	0.1	1	0.495	0.535	7.534

6.4. Full Factorial Simulation Results

The full factorial FE simulations was carried out by means of an amalgamation of three parameters viz., high working temperatures, varying punch speed as well as holding time, in order to get a full series of spring back variations as presented in Table 6.3.

Table 6.3 Full factorial FE simulation outcome of spring back

Temperature (°C)	**Punch speed (mm/s)**	**Holding time (min)**	**SB (degree)**
700	0.01	0	2.921
700	0.01	1	3.000
700	0.01	10	2.978
700	0.05	0	2.600
700	0.05	1	3.082
700	0.05	10	3.050
700	0.1	0	2.069
700	0.1	1	3.176
700	0.1	10	3.194
800	0.01	0	1.909
800	0.01	1	1.978
800	0.01	10	2.010
800	0.05	0	1.602
800	0.05	1	2.055
800	0.05	10	2.065
800	0.1	0	1.025
800	0.1	1	2.077
800	0.1	10	2.124
900	0.01	0	0.298
900	0.01	1	0.491
900	0.01	10	0.514
900	0.05	0	-0.108
900	0.05	1	0.549
900	0.05	10	0.556
900	0.1	0	-0.522
900	0.1	1	0.495
900	0.1	10	0.554

6.5. Optimization Methods Applied for Full Factorial Design

In order to get the optimal process parameters setting, full factorial simulations of spring back has been optimized using RSM and GA.

6.5.1 Response Surface Method

To comprehensively understand the influence of individual parameter, the response surface method (RSM) has been used for full factorial simulations (L_{27}) in the Minitab software version 16, similarly used by Gupta (2010). In general, RSM uses a polynomial Eq. (6.2),

$$Y = b_0 + b_1x_1 + b_2x_2 + b_3x_3 + b_{12}x_1x_2 + b_{13}x_1x_3 + b_{23}x_2x_3 + b_{11}x_1^2 + b_{22}x_2^2 + b_{33}x_3^2 \quad (6.2)$$

where Y - spring back (degree). x_1 - temperature (°C), x_2 - punch speed (mm/s) & x_3 - holding time (minutes). b_0 - constant term. b_1, b_2 & b_3 - coefficients of the linear terms. b_{12}, b_{13} & b_{23} - coefficients of the interaction terms and b_{11}, b_{22}, & b_{33} - coefficients of the square terms respectively.

Polynomial Eq. (6.3) after substituting all the coefficients obtained from RSM,

$$Y = -5.11 + 0.02\,x_1 + 1.08\,x_2 + 0.55\,x_3 - 0.005\,x_1x_2 + 0.00004\,x_1x_3 + 0.672\,x_2x_3 - 0.00002\,x_1^2 - 11.086\,x_2^2 - 0.056\,x_3^2 \quad (6.3)$$

Contour plots have been generated for some of the selected settings as shown in Figure 6.6 (a) - (d) i.e., (a) 700_0.1_0 where SB is 2.069, (b) 800_0.05_0 where SB is 1.602, (c) 900_0.05_0 where SB is -0.108 and (d) 900_0.1_10 where SB is 0.554.

The contour plots display the range of spring back values for each setting from minimum to maximum. The obtained spring back values can be checked and visualized from contour regions. Contour plots vary based on the interaction between process parameters and their effect can be observed pertaining to individual setting with respective spring back value.

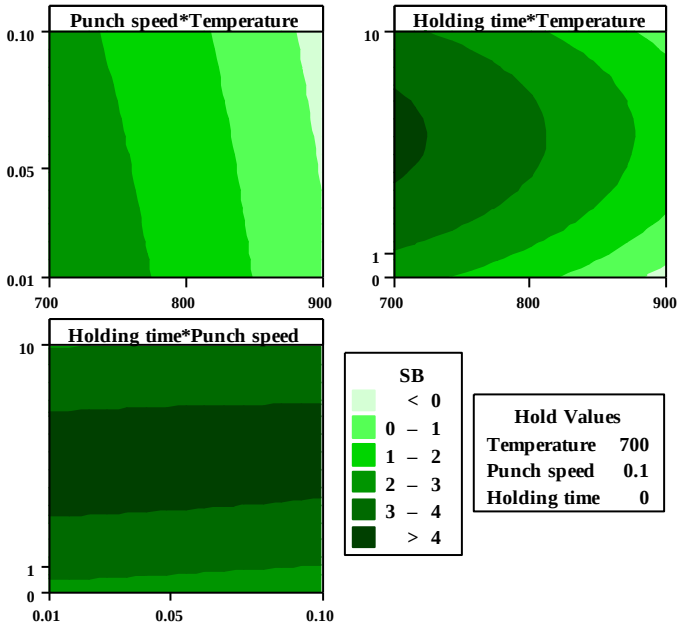

(a)

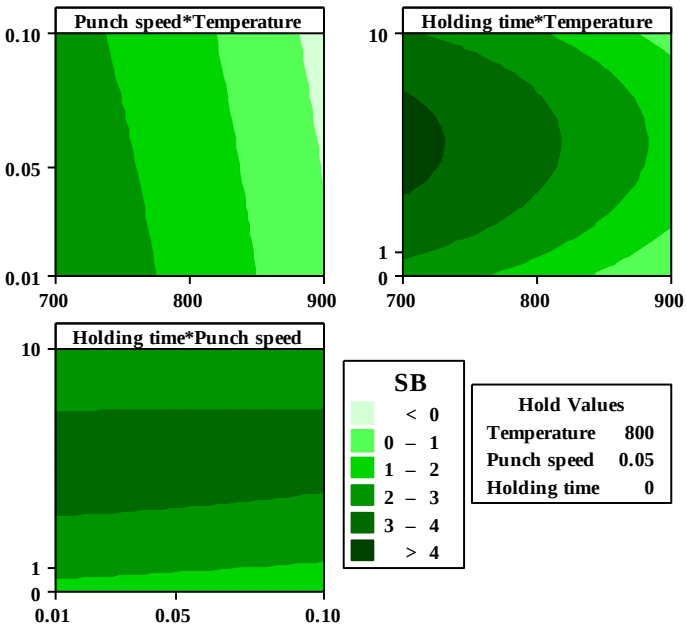

(b)

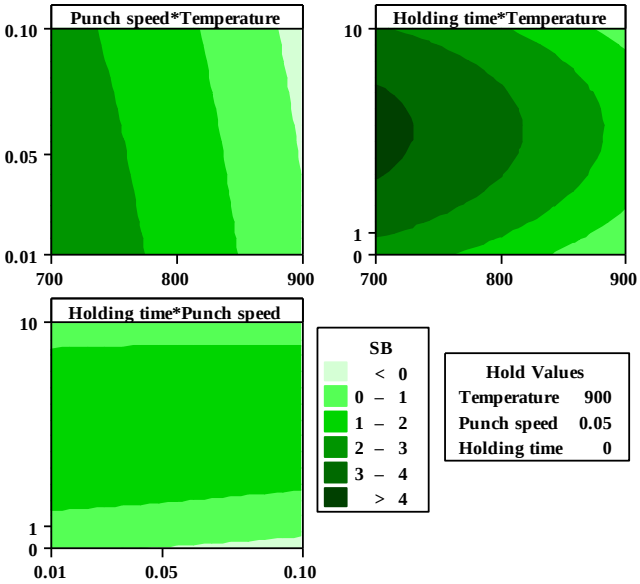

(c)

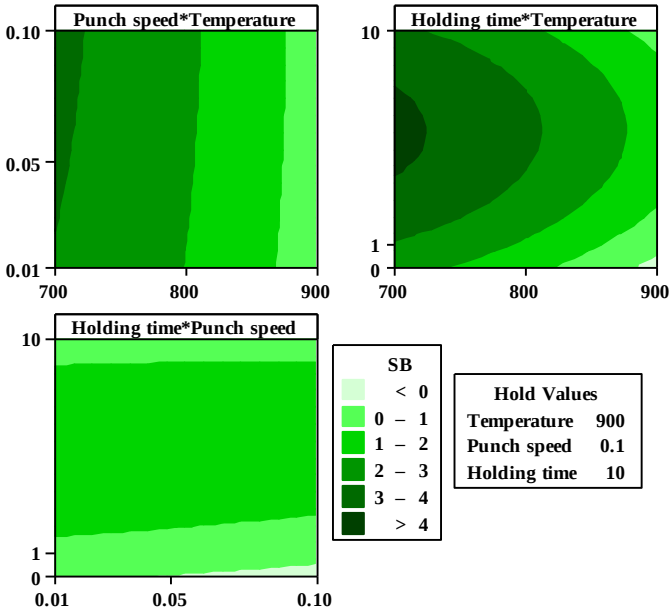

(d)

Figure 6.6 Contour plots at different settings (a) 700_0.1_0, (b) 800_0.05_0, (c) 900_0.05_0 and (d) 900_0.1_10

6.5.2 Genetic Algorithm

The polynomial Eq. (6.3) has been applied as a fitness function, then the optimization of parameters was performed step by step using genetic algorithm (GA)

in Matlab optimization toolbox version R2017a. Prior to optimization by GA, a set of preferences have been given for individual fitness value. Amongst them, individuals with greater fitness has been sensibly selected following the principle of persistence of the fittest. After subsequent progress from generation to generation, it comes together as the fittest individual.

The settings applied in GA are as follows: population size = 50, generations = 100, fitness scaling function:- proportional, selection:- tournament, reproduction:- elite count = 0.05*population size, crossover fraction = 0.8 and mutation function:- adaptive feasible.

The spring back outcome from full factorial simulations as presented in Table 6.3 has been applied in RSM and the necessary constants have been attained for each and in a group of parameters with respective T as well as P values are presented in Table 6.4. The acquired regression constants express very high R^2 as well as suitable adjusted R^2 with satisfactory goodness of fit. The analysis presented in Table 6.4 has been executed with coded units.

In Table 6.4, SE Coeff. denotes standard error of constant, T signifies statistical test indicating the variance in means. Each T value has an associated P value presenting statistical importance of variance. R^2 denotes the constant of determination viz. higher the R^2, superior is the association between spring back as well as parameters. Whereas, R^2(adj) represent adjusts statistic based on the no. of present variables.

At the same time, ANOVA has been performed as presented in Table 6.5 and it provides the p-value mostly below 5% in the respective sources, showing high impact of all three parameters in getting minimum possible spring back.

In Table 6.5, DF means degrees of freedom and it describes a precarious value at which an assumption may be accepted or may be rejected, whereas Seq. SS represents a sequential (progressive) sum of squares, showing deviation of specific quantity from the mean. Adj SS shows modification in the sum of squares. While, Adj MS means Adjusted mean of squares and it signifies variation in the model. Simultaneously, *F* statistic expresses whether mean variances are statistically important among two groups or not and *P* designates probability and if value of $P < 5\%$, it means substantial contribution of process parameters in decreasing the spring back. Lastly, the regression coefficients have been calculated by means of the data based on un-coded units as presented in Table 6.6.

Table 6.4 Calculated regression constants for FE simulated spring back based on the coded units

Terms	**Coefficients**	**SE Coefficients**	***T* values**	***P* values**
Constant	3.207	0.230	13.914	0.000
Temperature (T)	-1.286	0.046	-27.400	0.000
Punch speed (PS)	-0.065	0.046	-1.398	0.180
Holding time (HT)	0.297	0.045	6.605	0.000
T*T	-0.266	0.077	-3.418	0.003
PS*PS	-0.022	0.079	-0.284	0.780
HT*HT	-1.414	0.238	-5.935	0.000
T*PS	-0.026	0.054	-0.479	0.638
T*HT	0.020	0.050	0.418	0.681
PS*HT	0.151	0.049	3.032	0.008
$S = 0.190$	$R^2 = 98.16\%$	$R^2(\text{adj}) = 97.18\%$		

Table 6.5 ANOVA for FE simulated spring back

Source	DF	Seq SS	Adj SS	Adj MS	F	P
Regression	9	32.985	32.985	3.665	100.64	0.000
Linear	3	30.925	29.008	9.669	265.52	0.000
T	1	30.013	27.340	27.340	750.76	0.000
PS	1	0.206	0.071	0.071	1.96	0.180
HT	1	0.705	1.588	1.588	43.62	0.000
Square	3	1.711	1.711	0.570	15.66	0.000
T*T	1	0.425	0.425	0.425	11.68	0.003
PS*PS	1	0.002	0.002	0.002	0.08	0.780
HT*HT	1	1.282	1.282	1.282	35.23	0.000
Interaction	3	0.349	0.349	0.116	3.20	0.050
T*PS	1	0.008	0.008	0.008	0.23	0.638
T*HT	1	0.006	0.006	0.006	0.17	0.681
PS*HT	1	0.334	0.334	0.334	9.19	0.008
Residual Error	17	0.619	0.619	0.036	-----	-----
Total	26	33.604	----------			

Table 6.6 Calculated regression constants for spring back using uncoded units

Terms	Coefficients
Constant	-5.112
T	0.029
PS	1.082
HT	0.554
T*T	-2.662E-06
PS*PS	-11.086
HT*HT	-0.056
T*PS	-0.005
T*HT	4.179E-05
PS*HT	0.672

By means of the data from Table 6.6, the acquired constants have been applied for completing polynomial Eq. 6.2 to obtain Eq. 6.3 which has been used as a fitness function in the GA. As a final point, by means of GA, RSM has been optimized. Finally, obtained optimum parameters are as follows: temperature:- 900℃, punch speed:- 0.05 mm/s as well as holding time:- 0.05 minutes. Based on this setting, a confirmation test has been conducted.

6.6. Confirmation Test

The optimal process parameters acquired from GA for minimizing spring back has been used to carry out FE simulation and its experimental validation. These simulation and experimental results have been presented in Table 6.7. From here, it can be concluded that the optimization approach of combining RSM with GA has been very effective to obtain the minimum spring back value, quite close enough to zero spring back. The minimum spring back value at the optimum parameters setting through FE simulation is obtained as only 0.067 degree, further which was found to be in close agreement with the experimental result of 0.073 degree, having only 8.2% error.

Table 6.7 Simulation and experimental spring back value for the optimum process parameters

	FEA	**Experiment**	**Error (%)**
Spring back (degree)	0.067	0.073	8.2

6.1. Summary

This chapter has covered FE modelling and optimization of spring back behaviour in V-bending process for Ti-6Al-4V alloy. FE analysis brought out that with the rise of temperature in an amalgamation with other parameters, spring back decreases to a major extent. The FE simulation results of Taguchi L_9 orthogonal array are found to be in close agreement with the experimental results with percentage error being less than 10%. Further, using a full factorial design on FE simulations, optimization of spring back value is obtained with the help of RSM and GA. The obtained optimum settings of process parameters have been used for the experimental confirmation test, which resulted in almost zero spring back value.

CHAPTER 7 : CONCLUSIONS

This thesis presents the studies on the deformation behaviour, the processing maps and the spring back behaviour of Ti-6Al-4V alloy at high temperatures. Some of the salient conclusions of the work are as follows:

7.1. Salient Conclusions

- The key outcomes based on the mechanical and microstructural characterization of Ti-6Al-4V alloy at high temperature are as follows:
  - The calculated flow softening index shows that the highest value obtained is along 0º orientation followed by 90º and 45º orientations.
  - Based on the tensile tests conducted at various high temperatures as well as low strain rates, Ti-6Al-4V alloy exhibited superplastic behaviour at 10^{-4} s^{-1} and 750℃ onwards, as the percentage elongation increases more than 200%.
  - Microstructural characterization revealed the coarsening of grains as well as increase in the area and volume fraction of beta phase with increase in temperature.
  - The ductility improvement at high temperatures could be attributed to the grain boundary sliding as well as the phase change from alpha to beta at high temperatures and it helps as a supplementary stress accommodation mechanism, leading to a significant increase in El % and decrease in YS and UTS.

- SEM study of the tested samples at high temperatures indicate enhanced quantity of dimples as well as flow lines confirming ductility. XRD analysis distinctly shows that the elementary peaks place remains similar. However, the diffraction pattern show changes with increase in the temperature.

- Based on the tensile tests data, the constitutive model as well as processing maps were developed and the respective outcomes are presented as follows:
  - Johnson Cook model as well as Zerilli Armstrong model were unable to predict flow stress behaviour correctly due to the highly dominant flow softening effect. However, the flow stress prediction results based on the Modified Arrhenius (m-Arr) model quiet accurately matched with the experimental results, having *R* as 0.993, average absolute error as 11.34% and its standard deviation as 14.27%.
  - The prediction ability of m-Arr model has been in decent agreement with experimental flow stress performance, mainly at 10^{-2} s^{-1} and 10^{-3} s^{-1}. The variation at 10^{-4} s^{-1} strain rate might be due to the existence of superplasticity phenomenon from 750℃ to 900℃.
  - The values of *m* obtained at higher strain rates along with lower temperatures is less than (0.3 - 0.8) spectrum, confirming the absence of superplastic behaviour. However, at lower strain rates and high temperatures, the value of *m* lies within the specified range, confirming the presence of superplastic behaviour of Ti-6Al-4V alloy.
  - Processing maps distinctly illustrate the occurrence of superplasticity, as efficiency is high from 770℃ - 900℃ and at 10^{-2} s^{-1} - 10^{-4} s^{-1} strain rate

as well as a maximum efficiency of 85% is attained at 0.1 strain. Efficiency decreases as well as instability region increases with an increase in strain. Also, it is observed that instability occurs at 10^{-2} s^{-1} from 700℃ - 750℃ and at 10^{-3} s^{-1} for 700℃. SEM and microstructure analysis on these settings confirmed the existence of flow instabilities.

- Prasad's instability criteria predicts instable regions more accurately than Murthy's instability criteria, to ensure the safety in hot tensile working.
- A comparison of processing maps developed on the basis of tensile tests confirms superplasticity more accurately than compression tests.

- The outcomes of experimental and simulation studies on spring back behaviour of Ti-6Al-4V alloy at high temperature using V-bending process are as follows:
  - Analysis of Variance reveals that the percentage involvement of specific parameter expresses that temperature is the main dominating parameter subsequently followed by varying holding time as well as punch speed for reducing spring back. Moreover, as the temperature rises, the yield strength reduces leading to a substantial decrease in the spring back behaviour.
  - Highlights of FE simulation results for full factorial design revealed that the spring back behaviour from 3º at 700℃ reduces to 0.2º at 900℃.
  - FE results have been found analogous to the experimental results with percentage of error having a mean of 7.35% and standard deviation of 1.24%.

- RSM used in the full factorial design of spring back provides an excellent goodness of fit with R^2 = 98.16% as well as R^2(adj) = 97.18%. Also, ANOVA results indicate, temperature and holding time probability (*P*) values as 0%, representing the high impact of parameters in attaining minimum spring back.
- In the optimization of RSM using GA, optimum V-bending parameters to get minimum spring back were temperature:- 900°C, punch speed:- 0.05 mm/s as well as holding time:- 0.05 min. An experimental validation has been conducted using these parameters setting, achieving almost zero spring back value, and within close agreement with the simulation result.

7.2. Limitations of the Study

The limitations of this study are presented as follows:

- This study involved the development of a constitutive model based on m-Arr equation for predicting the flow stress values, however this could not be implemented in Abaqus for FE modelling of the V-bending process at high temperatures. This required development of UMAT codes which will be considered as a future work.
- The CTM for performing V-bending process at high temperatures was capable of achieving up to 1000°C temperature, but only 10^{-1} to 10^{-2} s^{-1} strain rates; whereas superplasticity required 10^{-4} s^{-1} strain rate and 700°C - 900°C temperature.

7.3. Specific Contribution to the Research

Through this work on the deformation behaviour, development of processing maps and spring back behaviour of Ti-6Al-4V alloy at high temperatures, the specific contribution made towards the state-of-the-art of research is the methodology to obtain almost zero spring back in the bending of Ti-6Al-4V alloy sheets. As Ti-6Al-4V alloy is known for its wide use in aerospace and defense applications, this methodology can be used to manufacture structural frames from Ti-6Al-4V alloy sheets using high temperature bending process and thus achieving frames with superior strength and low weights.

7.4.Future Scope

This research work can be enhanced further by implementing the following points:

- By developing UMAT code for m-Arr model, the FE analysis can be fine-tuned for studying the spring back behaviour.
- Structural frames from Ti-6Al-4V alloy sheets can be manufactured using high temperature bending process.
- The formability of Ti-6Al-4V alloy at high temperatures may be assessed for the deep drawing process as well as spring back behaviour can also be studied using split ring test.

REFERENCES

Ablat, Muhammad Ali, and Ala Qattawi. 2017. "Numerical simulation of sheet metal forming: a review." *Int J Adv Manuf Technol* 89: 1235-1250.

Adamus, Janina, and Piotr Lacki. 2011. "Forming of the titanium elements by bending." *Computational Materials Science* 50 (4): 1305-1309.

Alabort, E, D Putman, and R C Reed. 2015. "Super plasticity in Ti-6Al-4V: characterisation, modelling and applications." *Acta Materialia* 95: 428-442.

Alvarez, M.J., L. Ilzarbe, E. Viles, and M. Tanco. 2009. "The Use of Genetic Algorithms in Response Surface Methodology." *Quality Technology & Quantitative Management* 6 (3): 295-307.

Ao, Dongwei, Xingrong Chu, Yang Yang, Shuxia Lin, and Jun Gao. 2018. "Effect of electropulsing on springback during V-bending of Ti-6Al-4V titanium alloy sheet." *The International Journal of Advanced Manufacturing Technology* 96 (9-12): 3197-3207.

Badr, Ossama Mamdouh, Bernard Rolfe, Peter Hodgson, and Matthias Weiss. 2015. "Forming of high strength titanium sheet at room temperature." *Materials and Design* (66): 618-626.

Banabic, Dorel. 2010. *Sheet Metal Forming Processes.* Springer.

Bao, Jianxing, Jie Xu, Jianan Bai, Shoudan Lv, Debin Shan, and Bin Guo. 2020. "Mechanical behavior and shear banding of electropulsing-assisted micro-scale shear-compression in Ti-6Al-4V alloy." *Materials Science and Engineering: A* 771.

Bao, Weizong, Longke Bao, Dan Liu, Deyi Qu, Zhuangzhuang Kong, Mingjun Peng, and Yonghua Duan. 2020. "Constitutive Equations, Processing Maps, and

Microstructures of Pb-Mg-Al-B-0.4Y Alloy under Hot Compression." *Journal of Materials Engineering and Performance* 29: 607-619.

Bodunrin, Michael Oluwatosin. 2020. "Flow stress prediction using hyperbolic-sine Arrhenius constants optimised by simple generalised reduced gradient refinement." *Journal of Materials Research and Technology* 9 (2): 2376-2386.

Boyer, Rodney, Gerhard Welsch, and E.W. Collings. 1994. *Materials Properties Handbook: Titanium Alloys.* Materials Park, Ohio: ASM international.

Cai, Jun, Xiaolu Zhang, Kuashe Wang, Qingjuan Wang, and Wen Wang. 2016. "Development and validation of processing maps for Ti-6Al-4V alloy using various flow instability criteria." *Journal of Materials Engineering and Performance* 25: 4750-4756.

Chan, W.M., H.I. Chew, H.P. Lee, and B.T. Cheok. 2004. "Finite element analysis of spring-back of V-bending sheet metal forming processes." *Journal of Materials Processing Technology* 148 (1): 15-24.

Chandra, Namas. 2002. "Constitutive behaviour of superplastic materials." *International Journal of Non-Linear Mechanics* 37: 461-484.

Chen, Chang-Cheng. 2014. "Experimental Study on Punch Radius and Grain Size Effects in V-Bending Process." *Materials and Manufacturing Processes* 29: 461-465.

Chen, Liang, Guoqun Zhao, Junquan Yu, and Wendong Zhang. 2015. "Constitutive analysis of homogenized 7005 aluminum alloy at evaluated temperature for extrusion process." *Materials and Design* 66 : 129–136.

Chen,, Liang, Guoqun Zhao, and Junquan Yu. 2015. "Hot deformation behavior and constitutive modeling of homogenized 6026 aluminum alloy." *Materials and Design* 74: 25-35.

Cui, Xiaohui, Zhiwu Zhang, Zhihao Du, Hailiang Yu, Dongyang Qiu, Yongqi Cheng, and Xiaoting Xiao. 2020. "Inverse bending and springback-control using magnetic pulse forming." *Journal of Materials Processing Tech.* 275: 116374.

Debta, M.K., B.D. Bishoyi, R.K. Sabat, W. Muhammad, and S.K. Sahoo. 2020. "Microstructure and texture evolution during annealing of Ti–6Al–4V alloy." *Materials Science and Technology* 36: 417-424.

Dieter, George E. 2013. *Mechanical Metullargy.* McGraw Hill Education.

Froes, F.H. 2015. *Titanium physical metallurgy, processing and applications.* Materials park, Ohio: ASM International.

Gao, Pengfei, Mingwang Fu, Mei Zhan, Zhenni Lei, and Yanxi Li. 2020. "Deformation behavior and microstructure evolution of titanium alloys with lamellar microstructure in hot working process: A review." *Journal of Materials Science & Technology* 39: 56-73.

Ghasemi, E., A. Zarei-Hanzaki, E. Farabi, K. Tesar, A. Jager, and M. Rezaee. 2017. "Flow softening and dynamic recrystallization behavior of BT9 titanium alloy: A study using process map development." *Journal of Alloys and Compounds* 695: 1706-1718.

Giuliano, Gillo. 2011. *Superplastic forming of advanced metallic materials methods and applications.* (Wood head Publishing Limited).

Gupta, Amit Kumar, Nitin Hansoge Krishnamurthy, Yashjeet Singh, Mangaprasad Kaushik, and Swadesh Kumar Singh. 2013. "Development of constitutive models for dynamic strain aging regime in austenitic stainless steel 304." *Materials and Design* 45: 616-627.

Gupta, Amit Kumar. 2010. "Predictive modelling of turning operations using response surface methodology, artificial neural networks and support vector regression." *International Journal of Production Research* 48 (3): 763-778.

Gupta, Amit Kumar, Anirudh V Krishnan, and Swadesh Kumar Singh. 2013. "Constitutive models to predict flow stress in Austenitic Stainless Steel 316 at elevated temperatures." *Materials and Design* 43: 410-418.

Han, Pyokyoung, and Jongsoo Lee. 2009 . "A response surface based sequential approximate optimization using constraint-shifting analogy." *Journal of Mechanical Science and Technology* 23 : 2903-2912.

Huang, Yang, Jingjing Ji, and Kok-Meng Lee. 2018. "An improved material constitutive model considering temperature-dependent dynamic recrystallization for numerical analysis of Ti-6Al-4V alloy machining." *International Journal of Advanced Manufacturing Technology* 97 (9-12): 3655-3670.

Inagaki, Ikuhiro, Tsutomu Takechi, Shirai Yoshihisa, and Nozomu Ariyasu. 2014. *Application and Features of Titanium for the Aerospace Industry.* Osaka city, Japan: Nippon steel & sumitomo metal technical report.

Jalumedi , Babu, and Abhijit Dutta. 2015. "Low temperature superplasticity through grain refinement in Ti-6Al-4V by a novel route of quench-roll-recrystallise." *Journal of Materials Research and Technology* 4 (3): 348-352.

Jata, K.V, A.K. Hopkins, and R.J. Rioja. 1996. "The Anisotropy and Texture of Al-Li Alloys." *Materials Science Forum* 647-652.

Jha, Jyoti S., Suraj P. Toppo, Rajkumar Singh, Asim Tewari, and Sushil K. Mishra. 2019. "Flow stress constitutive relationship between lamellar and equiaxed microstructure during hot deformation of Ti-6Al-4V." *Journal of Materials Processing Technology* 270: 216-227.

Kalpakjian, Serope, and Steven R. Schmid. 2009. *Manufacturing Processes for Engineering Materials.* Pearson Education.

Karaagac, Ibrahim. 2016. "The Experimental Investigation of Springback in V-Bending Using the Flexforming Process." *Arab J Sci Eng* 42 (5): 1853-1864.

Khan, Akhtar S., and Shaojuan Yu. 2012. "Deformation induced anisotropic responses of Ti–6Al–4V alloy. Part I: Experiments." *International Journal of Plasticity* 38: 1–13.

Kim, J. S., J. H. Kim, Y. T. Lee, C G Park, and C. S. Lee. 1999. "Microstructural analysis on boundary sliding and its accommodation mode during superplastic deformation of Ti-6Al-4V alloy." *Material Science and Engineering A* 263: 272–280.

Kotkunde, Nitin, Aditya D Deole, Amit Kumar Gupta , and Swadesh Kumar Singh. 2014. "Comparative study of constitutive modelling for Ti-6Al-4V alloy at low strain rates and elevated temperatures." *Materials and Design* 55: 999-1005.

Kotkunde, Nitin, Amit Kumar Gupta, and Swadesh Kumar Singh. 2015. "Formability study of Ti-6Al-4V alloy under warm conditions." *Advances in Materials and Processing Technologies* 1: 210-222.

Kotkunde, Nitin, Nitin Hansoge Krishnamurthy, Pavan Puranik, Amit Kumar Gupta, and Swadesh Kumar Singh. 2014. "Microstructure study and constitutive modelling of Ti–6Al–4V alloy at elevated temperatures." *Materials and Design* 54: 96-103.

Leu, Daw-Kwei, and Zhi-Wei Zhuang. 2016. "Springback prediction of the vee bending process for high-strength steel sheets." *Journal of Mechanical Science and Technology* 30 (3): 1077-1084.

Leyens, C, and M Peters. 2003. *Titanium and Titanium alloys fundamentals and applications.* (WILEY-VCH Verlag GmbH & Co).

Li, Feifan, Jianjun Wu, Yang Li, Zengkun Zhang, and Yong'an Wang. 2016. "A new calculating method to perform springback predictions for varied curvature sheet bending based on the B-spline function." *International Journal of Mechanical Sciences* 113: 71-80.

Li, M.Q., and W.F. Zhang. 2009. "Effect of hydrogen on processing maps in isothermal compression of Ti–6Al–4V titanium alloy." *Materials Science and Engineering A* 502: 32-37.

Li, Xiaoqiang, Guiqiang Guo, Junjie Xiao, Nan Song, and Dongsheng Li. 2014. "Constitutive modeling and the effects of strain-rate and temperature on the formability of Ti–6Al–4V alloy sheet." *Materials and Design* 325-334.

Liang, Riqiang, and Akhtar S. Khan. 1999. "A critical review of experimental results and constitutive models for BCC and FCC metals over a wide range of strain rates and temperatures." *International Journal of Plasticity* 963-980.

Lin, Y. C, and Xiao-Min Chen. 2011. "A critical review of experimental results and constitutive descriptions for metals and alloys in hot working." *Materials and Design* 32: 1733-1759.

Liu, Jun, Ming Jen Tan, Aue-U-Lan Yingyot, Meiling Guo, Sylvie Castagne, and Beng Wah Chua. 2013. "Superplastic-like forming of Ti-6Al-4V alloy." *The International Journal of Advance Manufacturing Technology* 69: 1097-1104.

Liu, Po, Taichao Zhang, Bin Guo, Li Yang, Debin Shan, and Yingying Zong. 2019. "Deformation path and springback behavior in double-curved bending at high temperature." *Journal of Mechanical Science and Technology* 33 (9): 4361-4370.

Liu, Qiang, Songxiao Hui, Ke Tong, Yang Yu, Wenjun Ye, and Sheng-yin Song. 2019. "Investigation of high temperature behavior and processing map of Ti-6Al-4V-0.11Ru titanium alloy." *Journal of Alloys and Compounds* 787: 527-536.

Liu, Qiang, Wenjuan Liu, Feng Ruan, and Hongyang Qiu. 2007. "Parameters' automated optimization in sheet metal forming process ." *Journal of Materials Processing Technology* 187-188: 159-163.

Liu, Wenjuan, Qiang Liu, Feng Ruan, Zhiyong Liang, and Hongyang Qiu. 2007. "Springback prediction for sheet metal forming based on GA-ANN technology." *Journal of Materials Processing Technology* 187-188: 227-231.

Lukaszek-Solek, Aneta, and Janusz Krawczyk. 2015. "The analysis of the hot deformation behaviour of the Ti–3Al–8V–6Cr–4Zr–4Mo alloy, using processing maps, a map of microstructure and of hardness." *Materials and Design* 65: 165–173.

Luo, Jiao, Miaoquan Li, Weixin Yu, and Hong Li. 2009. "Effect of the strain on processing maps of titanium alloys in isothermal compression." *Materials Science and Engineering A* 504: 90-98.

Lypchanskyi, Oleksandr, Tomasz Sleboda, Marek Wojtaszek, Krzysztof Muszka, Aneta Łukaszek-Sołek, Rafał Stanik, and Maik Gude. 2020. "The analysis of flow behavior of Ti-6Al-2Sn-4Zr-6Mo alloy based on the processing maps." *International Journal of Material Forming.*

Martinez, Omar Pérez, and Hugo I. Medellín-Castillo. 2019. "Analysis and assessment of the spring back effect of steel sheet metal under bending operations." *International Mechanical Engineering Congress and Exposition (IMECE).* Salt lake city, USA: ASME.

Miller, R.M., T.R. Bieler, and S.L. Semiatian. 1999. "Flow softening during hot working of Ti-6Al-4V with a lamellar colony microstructure." *Scripta Materialia* 1387-1393.

Montgomery, Douglas C. 2017. *Design and Analysis of Experiments.* New york: John Wiley and sons.

Odenberger, E.-L., M. Oldenburg, P. Thilderkvist, T. Stoehr, J. Lechler, and M. Merklein. 2011. "Tool development based on modelling and simulation of hot sheet metal forming of Ti–6Al–4V titanium alloy." *Journal of Materials Processing Technology* 211 (8): 1324-1335.

Ozturk, Fahrettin, Remzi Ecmel Ece, Naki Polat, and Arif Koksal. 2010. "Effect of Warm Temperature on Springback Compensation of Titanium Sheet." *Materials and Manufacturing Processes* 25: 1021-1024.

Panthi, S.K., N. Ramakrishnan, K.K. Pathak, and J.S. Chouhan. 2007. "An analysis of springback in sheet metal bending using finite element method (FEM)." *Journal of Materials Processing Technology* 186: 120-124.

Papeleux, Luc, and Jean-Philippe Ponthot. 2002. "Finite element simulation of springback in sheet metal forming." *Journal of Materials Processing Technology* 125-126: 785-791.

Park, Nho-Kwang, Jong-Taek Yeom, and Young-Sang Na. 2002. "Characterization of deformation stability in hot forging of conventional Ti–6Al–4V using processing maps." *Journal of Materials Processing Technology* 130-131: 540-545.

Patankar, S N, J P Escobedo, D P Field, G Salishchev, R M Galeyev, O R Valiakhmetov, and F H Froes. 2002. "Superior superplastic behaviour in fine-grained Ti-6Al-4V sheet." *Journal of Alloys and Compounds* 345: 221-227.

Picu, R. C, and A Majorell. 2002. "Mechanical behaviour of Ti-6Al-4V at high and moderate temperatures - Part II: constitutive modelling." *Materials Science and Engineering A* 326: 306-316.

Porntadawit, J, V Uthaisangsuk, and P Choungthong. 2014. "Modelling of flow behaviour of Ti–6Al–4V alloy at elevated temperatures." *Materials Science and Engineering A* 599: 212-222.

Prasad, Y.V.R.K, and T Seshacharyulu. 1998. "Processing maps for hot working of titanium alloys." *Materials Science and Engineering A* 243: 82–88.

Prasad, Y.V.R.K, K.P Rao, and S Sasidhara. 2015. *Hot working guide: a compendium of processing maps.* ASM international.

Quan, Guo-zheng, Yao-yao Ma, Yu-qing Zhang, Pu Zhang, and Wei-yong Wang. 2020. "Separation of dynamic recrystallization parameter domains from a chaotic system for Ti–6Al–4V alloy and its application in parameter loading path design." *Materials Science and Engineering: A* 772: 138745.

Rahman, Mahfujur, I. Reid, P. Duggan, D.P. Dowling, G. Hughes, and M.S.J. Hashmi. 2007. "Structural and tribological properties of the plasma nitrided Ti-alloy biomaterials Influence of the treatment temperature." *Surface and coatings technology* 201: 4865-4872.

Ramadass, Rajesh, Saravanan Sambasivam, and Karthik Thangavelu. 2019. "Selection of optimal parameters in V-bending of Ti-Grade 2 sheet to minimize springback." *Journal of the Brazilian Society of Mechanical Sciences and Engineering* 1-11. doi:DOI:10.1007/s40430-018-1521-x.

Roy, Shibayan, and Satyam Suwas. 2013. "The influence of temperature and strain rate on the deformation response and microstructural evolution during hot compression of a titanium alloy Ti–6Al–4V–0.1B." *Journal of Alloys and Compounds* 548: 110-125.

Roy, Shibayan, R. Madhavan, and Satyam Suwas. 2014. "Crystallographic texture and microstructure evolution during hot compression of Ti–6Al–4V–0.1B alloy in the (α + β)-regime." *Philosophical Magazine* 94 (4): 358-380.

Salishchev, G A, R M Galeyev, O R Valiakhmetov, R V Safiullin, R Y Lutfullin, O N Senkov, F H Froes, and O A Kaibyshev. 2001. "Development of Ti-6Al-4V sheet with low temperature superplastic properties." *Journal of Materials Processing Technology* 116: 265-268.

Santos, Abel D., Ana Reis, J.F. Duarte, Pedro Teixeira, A. Barata Rocha, M.C. Oliveira, J.L. Alves, and Luis Menezes. 2004. "A benchmark for validation of numerical results in sheet metal forming." *Journal of Materials Processing Technology* 155-156: 1980-1985.

Saxena, K.K., V Pancholi, S.K. Jha, G.P. Chaudhari, D. Srivastava, and G.K. Dey. 2017. "A novel approach to understand the deformation behavior in two phase region using processing map." *Journal of Alloys and Compounds* 706: 511-519.

Sellars, CM, and WJ McTegart. 1966. "On the mechanism of hot deformation." *Acta Metallurgica* 14: 1136-1138.

Semiatin, S.L. 2006. *ASM Handbook, Volume 14B, Metalworking: sheet forming.* Materials Park, Ohio: ASM International.

Semiatin, S.L., and T.R. Bieler. 2001. "Effect of Texture and Slip Mode on the Anisotropy of Plastic Flow and Flow Softening during Hot Working of Ti-6Al-4V." *Metallurgical and Materials Transactions A* 1787-1799.

Sen, Indrani, Ravi Sankar Kottada, and U. Ramamurty. 2010. "High temperature deformation processing maps for boron modified Ti–6Al–4V alloys." *Materials Science and Engineering A* 527: 6157-6165.

Seshacharyulu, T, S C Medeiros, W G Frazier, and Y.V.R.K Prasad. 2002. "Microstructural mechanisms during hot working of commercial grade Ti–6Al–4V with lamellar starting structure." *Materials Science and Engineering A* 325: 112–125.

Seshacharyulu, T, S. C Medeiros, W. G Frazier, and Y.V.R.K Prasad. 2000. "Hot working of commercial Ti–6Al–4V with an equiaxed α–β microstructure:

materials modelling considerations." *Materials Science and Engineering A* 284: 184–194.

Shong, Z.C., Z.R. Ling, and J. Peklenik. 1983. "A Study of the Hot Sizing and High Temperature Mechanical Behaviour for Titanium Alloy Sheet." *CIRP Annals* 32 (1): 161-165.

Singh, Gaurav, J. Quinta da Fonseca, and M. Preuss. 2020. "Microstructure evolution and deformation texture during rolling of TIMETAL 407." *Materialia* 9: 100596.

Sorgente, Donato, Gianfranco Palumbo, Antonio Piccininni, Pasquale Guglielmi, and Luigi Tricarico. 2017. "Modelling the superplastic behaviour of the Ti6Al4V-ELI by means of a numerical/experimental approach." *Int J Adv Manuf Technol* (90): 1-10.

Sousa, L.C, C.F. Castro, and C.A.C. Antonio. 2006. "Optimal design of V and U bending processes using genetic algorithms." *Journal of Materials Processing Technology* 172: 35-41.

Su, Yu, Fantao Kong, FengHai You, Xiaopeng Wang, and Yuyong Chen. 2020. "The high-temperature deformation behavior of a novel near-α titanium alloy and hot-forging based on the processing map." *Vacuum* 173: 109135.

Sun, Y., W.D. Zeng, Y.Q. Zhao, X.M. Zhang, Y. Shu, and Y.G. Zhou. 2011. "Research on the hot deformation behavior of Ti40 alloy using processing map." *Materials Science and Engineering A* 528: 1205-1211.

Sun, Yu, Zhipeng Wan, Lianxi Hu, and Junshuai Ren. 2015. "Characterization of hot processing parameters of powder metallurgy TiAl-based alloy based on the

activation energy map and processing map." *Materials and Design* 86: 922-932.

Sun, Yu, Zhuohan Cao, Zhipeng Wan, Lianxi Hu, Wenhong Ye, Niankui Li, and Changlong Fan. 2018. "3D processing map and hot deformation behavior of 6A02 aluminum alloy." *Journal of Alloys and Compounds* (742): 356-368.

Tamirisakandala, S, R.B Bhat, D.B Miracle, S Boddapati, R Bordia, R Vanover, and V.K Vasudevan. 2005. "Effect of boron on the beta transus of Ti–6Al–4V alloy." *Scripta Materialia* 53: 217–222.

Tang, Jung-Sung, Yiin-Kuen Fuh, and Shyong Lee. 2015. "Superplastic forming process applied to aero-industrial strakelet: wrinkling, thickness, and microstructure analysis." *International Journal of Advanced Manufacturing Technology* 77: 1513-1523.

Teimouri, Reza, Hamid Baseri, Behzad Rahmani, and Mohammad Bakhshi-Jooybari. 2012. "Modeling and optimization of spring-back in bending process using multiple regression analysis and neural computation." *International journal of material forming* 178: 167-178.

Tekiner, Zafer. 2004. "An experimental study on the examination of springback of sheet metals with several thicknesses and properties in bending dies." *Journal of Materials Processing Technology* 145: 109-117.

Tekkaya, A. Erman. 2000. "State-of-the-art of simulation of sheet metal forming." *Journal of Materials Processing Technology* 103 (1): 14-22.

Thipprakmas, Sutasn, and Wiriyakorn Phanitwong. 2011. "Process parameter design of spring-back and spring-go in V-bending process using Taguchi technique." *Materials and Design* 32 (8-9): 4430-4436.

Tisza, M. 2004. "Numerical modelling and simulation in sheet metal forming." *Journal of Materials Processing Technology* 151: 58-62.

Tuninetti, V, and A. M Habraken. 2014. "Impact of anisotropy and viscosity to model the mechanical behaviour of Ti–6Al–4V alloy." *Materials Science and Engineering A* 605: 39–50.

Tuoyang, Zhang, Liu Yong, G Sanders Daniel, Liu Bin, Zhang Weidong, and Zhou Canxu. 2014. "Development of fine-grain size titanium 6Al-4V alloy sheet material for low temperature superplastic forming." *Materials Science and Engineering A* 608: 265-272.

Vanderhasten, M, L Rabet, and B Verlinden. 2007. "Deformation mechanisms of Ti-6Al-4V during tensile behaviour at low strain rate." *Journal of Materials Engineering and Performance* 16: 208-212.

Wagoner, Robert H., Hojun Lim, and Myoung-Gyu Lee. 2013. "Advanced Issues in springback." *International Journal of Plasticity* 3-20.

Wang, Guofeng, Xiao Li, Siyu Liu, and Yibin Gu. 2018. "Improved superplasticity and microstructural evolution of Ti2AlNb alloy sheet during electrically assisted superplastic gas bulging." *The International Journal of Advanced Manufacturing Technology* (99): 773-787.

Wang, Jin, Guoqun Zhao, and Mengjin Li. 2016. "Establishment of processing map and analysis of microstructure on multi-crystalline tungsten plastic deformation process at elevated temperature." *Materials and Design* 103: 268–277.

Wiebenga, J.H, A.H. van den Boogaard, and G. Klaseboer. 2012. "Sequential robust optimization of a V-bending process using numerical simulations." *Structural and Multidisciplinary Optimization* 46: 137-153.

Wu, Y.T., and C.H. Koo. 1998. "Effect of temperature on the anisotropic superplasticity of textured Ti-25Al-10Nb alloy." *Scripta Materialia* 267-271.

Xia, Yu-feng, Wei Jiang, Qian Cheng, Lai Jiang, and Li Jin. 2020. "Hot deformation behavior of Ti−6Al−4V−0.1Ru alloy during isothermal compression." *Trans. Nonferrous Met. Soc. China* 30: 134-146.

Xiao, J, D. S Li, X. Q Li, and T. S Deng. 2012. "Constitutive modelling and microstructure change of Ti-6Al-4V during the hot tensile deformation." *Journal of Alloys and Compounds* 541: 346-352.

Yan-Hong Xiao, and Cheng Guo. 2011. "Constitutive modelling for high temperature behaviour of 1Cr12Ni3Mo2VNbN martensitic steel." *Materials Science and Engineering A* 528: 5081-5087.

Zener, H C, and J Hollomon. 1944. "Effect of strain rate upon plastic flow of steel." *Journal of Applied Physics* 15: 22-32.

Zhang, Chao, Xiao qiang Li, Dong sheng Li, Chao hai Jin, and Jun jie Xiao. 2012. "Modelization and comparison of Norton-Hoff and Arrhenius constitutive laws to predict hot tensile behaviour of Ti-6Al-4V alloy." *Transactions of Nonferrous Metals Society of China* 22: 457-464.

Zhe, Wang, Wang Xinnan, and Zhu Zhishou. 2017. "Characterization of high-temperature deformation behavior and processing map of TB17 titanium alloy." *Journal of Alloys and Compounds* 692: 149-154.

Zhou, Xuan, Kelu Wang, Shiqiang Lu, Xin Li, Rui Feng, and Mingjun Zhong. 2020. "Flow behavior and 3D processing map for hot deformation of Ti-2.7Cu alloy." *Journal of Materials Research Technology*.

Zong, Yingying, Po Liu, Bin Guo, and Debin Shan. 2015. "Springback evaluation in hot V-bending of Ti-6Al-4V alloy sheets." *The International Journal of Advanced Manufacturing Technology* 76 (1-4): 577–585.

PUBLICATIONS

The research efforts put in this work has resulted in the following publications.

Publications in International Journals:

1) MA Wahed, AK Gupta, V Sharma, K Mahesh, SK Singh and N Kotkunde (2019) "Material Characterisation, Constitutive Modelling and Processing Map for Superplastic Deformation Region in Ti-6Al-4V Alloy" *International Journal of Advanced Manufacturing Technology*, 104, 3419–3438.
2) MA Wahed, AK Gupta, VSR Gadi, Supradeepan K, SK Singh and N Kotkunde (2020) "Parameter optimization in V-bending process at elevated temperatures to minimize spring back in Ti-6Al-4V alloy" *Advances in Materials and Processing Technologies*, 6(2), 430-444.

Publications in International Conferences:

1) MA Wahed, VSR Gadi, AK Gupta, Supradeepan K, SK Singh and NR Kotkunde (2019) "Finite element analysis of spring back in Ti-6Al-4V alloy" - published in *International Conference on Materials Processing and Characterisation (ICMPC)*, 18, Part 7, 2693-2699.
2) Mohd Abdul Wahed, Nitin Kotkunde, Amit Kumar Gupta and Swadesh Kumar Singh (2018) "Development of processing map for superplastic deformation of Ti-6Al-4V alloy" - published in *ASME - International Mechanical Engineering Congress and Exposition (IMECE)*. Paper No. IMECE 2018-88631, pp. V002T02A036; 7 pages.
3) MA Wahed, AK Gupta, SK Singh and N Kotkunde (2018) "Effect of anisotropy on mechanical properties of Ti-6Al-4V in superplastic region" published in *IOP conference series: Material Science and Engineering* 346, 012023.

BIOGRAPHIES

Biography of the Candidate

Mohd Abdul Wahed, graduated in Mechanical Engineering (B.E.) with division as first class from Osmania University, Hyderabad, India in the year 2009. Thereafter, he obtained his master's degree (M.E.) with specialization in CAD/CAM from Osmania University, Hyderabad, India in the year 2011. After completing post-graduation, he worked as an Assistant Professor and then joined as a Research Scholar (PhD) in the Department of Mechanical Engineering at Birla Institute of Technology and Science (BITS), Pilani, Hyderabad Campus, India in the year 2016. He is a Chartered Engineer and Member of Institution of Engineers (IE), India. Also, he is a Life Time Member of Indian Society for Technical Education (ISTE), India and Indian Science Congress Association (ISCA), India.

Biography of the Supervisor

Dr. Amit Kumar Gupta is working as a Professor in the Department of Mechanical Engineering, Birla Institute of Technology and Science (BITS), Pilani, Hyderabad Campus. He obtained his Doctoral degree from Nanyang Technological University (NTU), Singapore and Bachelor's degree from Indian Institute of Technology (IIT), Delhi in Mechanical engineering. For his PhD, he has received the prestigious Singapore Millennium Foundation award and for the excellence in teaching and research at BITS, he has been awarded the Prof. S. Venkateswaran Faculty Excellence Award, 2013. In November 2020, he has also been named in the list of top 2% scientists in the world by Stanford University. His research interest lies in the area of sheet metal forming, tensile testing and constitutive modeling, production scheduling, manufacturing simulation and modeling, predictive modeling

and optimization of manufacturing processes. He has successfully completed funded projects from BRNS, DST, UGC, DRDO, etc. and authored more than 200 publications in journals and conferences of international repute.

Biography of the Co-supervisor

Dr. Nitin Kotkunde, graduated in Mechanical Engineering (B.E.) from Dr. Babasaheb Ambedkar Marathwada University, Aurangabad, India. Thereafter, he received his master's degree (M.E.) and Ph.D. from Birla Institute of Technology and Science Pilani Hyderabad Campus, India. His research interest includes material testing and characterization of metal, hot deformation behaviour of metals, material model development, sheet metal forming analysis, finite element analysis, product design and development. He is currently working as an Assistant Professor in the Department of Mechanical Engineering at Birla Institute of Technology and Science Pilani Hyderabad Campus, India and has more than 04 years of teaching experience. So far, he has 30 publications in various International Journals and 26 publications in various International Conferences with a total citations of 544. Currently, he has two ongoing projects as Principal Investigator from DST ECR and BITS-Pilani (ACRG) worth of Rs. 41.43 lakhs. He has completed one sponsored project from BITS-Pilani (RIG).